UNIVERSITY OF CALIFORNIA,
IRVINE

Modeling Small Nanopore Arrays for Biomimetic Ionotronics

DISSERTATION

submitted in partial satisfaction of the requirements
for the degree of

DOCTOR OF PHILOSOPHY

in Physics

by

DaVante Cain

Dissertation Committee:
Professor Zuzanna Siwy, Chair
Professor Albert Siryaporn
Professor Craig Martens

2026

DEDICATION

To

Kimberly Hernandez

The love of my life.

TABLE OF CONTENTS

LIST OF FIGURES

ACKNOWLEDGMENTS

First and foremost, I would like to thank God for the gift of life and for the path that has been set before me. I am deeply grateful for the opportunities, challenges, and people who have shaped my journey and ultimately brought me to this point.

I would also like to express my deepest gratitude to Kimberly Hernandez, the mother of my children. Her love, support, patience, and presence throughout this journey have meant more to me than words can adequately express. Without her, I would truly be lost.

My sincerest gratitude goes to my research advisor and committee chair, Professor Zuzanna Siwy. Her character, leadership, dedication, and example have had a profound influence on me, both as a scientist and as a person. Under her mentorship, I have learned not only how to conduct meaningful scientific research, but also the importance of professionalism, perseverance, integrity, and hard work. I am truly grateful and honored to have been one of her graduate researchers and to have had the opportunity to learn from her throughout my doctoral studies.

I would also like to sincerely thank Professor Stacy Copp, Professor Albert Siryaporn, Professor Craig Martens, and Professor Mu-Chun Chen for their service on my advancement and doctoral committees and for their guidance and support throughout my graduate studies. Their time, expertise, thoughtful questions, and encouragement have contributed greatly to my development as a scientist.

I would like to extend a special thank you to Dr. David Weisbart, Professor of Mathematics at the University of California, Riverside, who played an important role in my academic development and in helping me reach graduate school. His mentorship, encouragement, and support during my time at UCR helped me recognize the possibility of pursuing graduate education and provided me with opportunities that contributed significantly to

the path that ultimately led me here. I remain deeply grateful for the role he played in my journey and for his belief in my potential.

To all of my lab mates throughout the years, thank you for your help, kindness, friendship, and support. I genuinely looked forward to coming to the lab each day, and all of you were a large part of what made that experience so enjoyable and memorable. The conversations, collaborations, challenges, and successes we shared will remain some of my fondest memories from graduate school.

I am also incredibly grateful to all of my collaborators throughout the years. Science is rarely accomplished alone, and the research presented in this dissertation would not have been possible without your expertise, ideas, hard work, and willingness to collaborate. I have been fortunate to work alongside so many talented scientists, and I sincerely appreciate everything you contributed to this work.

I would also like to acknowledge Oak Ridge National Laboratory for their partnership with the GEM fellowship opportunity that allowed me to conduct research there. The experience provided me with the opportunity to work in a new research environment, interact with scientists outside of my home institution, and broaden my perspective as a researcher. I am grateful for the opportunity and for the scientists and staff at Oak Ridge who contributed to that experience.

To my family and friends who have stood beside me throughout this journey, thank you. Your encouragement, patience, love, and belief in me carried me through many difficult moments. This journey was long and challenging, and I know that I would not have reached the finish line without the people who supported me along the way.

Chapter 4 of this dissertation is adapted from E. Cao, D. Cain, S. Silva, and Z. S. Siwy, “Ion Concentration Polarization Tunes Interpore Interactions and Transport Properties of

Nanopore Arrays," *Advanced Functional Materials*, 2024, 34, 2312646, used with permission from Wiley-VCH GmbH. The coauthors of this publication are Ethan Cao, Savannah Silva, and Zuzanna S. Siwy. Professor Zuzanna S. Siwy advised and supervised the research that forms the basis of this chapter.

Chapter 5 of this dissertation is adapted from D. Cain, E. Cao, I. Vlassiouk, T. E. Schäffer, and Z. S. Siwy, "Ion Concentration Polarization Causes a Nearly Pore-Length-Independent Conductance of Nanopores," *Faraday Discussions*, 2025, 257, 344–359, DOI: 10.1039/D4FD00148F, with permission from the Royal Society of Chemistry. The coauthors of this publication are Ethan Cao, Ivan Vlassiouk, Tilman E. Schäffer, and Zuzanna S. Siwy. Professor Zuzanna S. Siwy advised and supervised the research that forms the basis of this chapter.

Financial support for the research presented in this dissertation was provided by the National Science Foundation, Division of Chemistry, Mathematical and Physical Sciences, Award No. 2200524.

To everyone who played a role in this journey, whether mentioned here by name or not, I offer my sincerest gratitude. This accomplishment is not mine alone; it reflects the support, mentorship, friendship, collaboration, and sacrifices of many people who helped me along the way. Thank you.

VITA

DaVante Devon Lee Cain

2026	Ph.D. in Physics, University of California, Irvine
2025	M.S. in Physics, University of California, Irvine
2021	B.S. in Physics, University of California, Riverside
2021	B.S. in Applied Mathematics, University of California, Riverside

RESEARCH AND TEACHING INTERESTS

Nanofluidics

Finite Element Analysis

Development of Solid-State Memristive Electronics

Machine Learning

Fluid Mechanics

Classical Mechanics

Electrodynamics

Quantum Mechanics

Statistical Mechanics

RESEARCH EXPERIENCE

Professor Zuzanna Siwy, University of California Irvine
Graduate Research Assistant, January 2021 to January 2026

• Simulation of local concentrations in various nanopore array systems using COMSOL Multiphysics (finite element analysis software).

• Experimental fabrication and measurement of solid-state nanopore array devices using SEM, SEM-FIB, TEM, and EBL as a fundamental platform for studying biomimetic ionic circuits.

Scientist Charles Collier, Oak Ridge National Laboratory, Oak Ridge
Research Intern, Summer 2023

• Nanofabrication at the Center for Nanophase Materials Sciences

• Lipid Extrusion, thin film deposition, lithography, etching, microscale 3D printing

• Handling of lipid membranes with embedded ion channels

• Computer Aided Design and 3D Printer fabrication of microfluidic devices

• Characterization of neuromorphic circuitry

Professor Stacy Copp, University of California Irvine
Lab Rotation, Summer 2021

• Developed Machine Learning algorithms to classify DNA-stabilized silver clusters by magic number count

Professor David Weisbart, University of California Riverside, CA
Undergraduate Researcher, 2020-2021

• Derivation of discrete-time random walks convergence to Brownian Motion in Real numbers

Professor James Burnette III, University of California Riverside, CA
Undergraduate Researcher, 2019-2020

• Investigation of the circadian rhythm in Fairchild mandarin genome

• PCR, primer fabrication, gene identification, Bioinformatics

TEACHING AND ADVISING EXPERIENCE

Associate Instructor of Record, University of California Irvine, Department of Physics and Astronomy.

Lower Division Calculus-based Light and Waves Summer 2026,

Lower Division Calculus-based Classical Mechanics – Fall Quarter 2023 Lower Division
Lower Division Calculus-based Electrodynamics – Summer 2022, Summer 2023, Summer 2024

Part Time Community College Instructor, Irvine Valley College, Department of Physics and Astronomy.

Lower Division Calculus-based Classical Mechanics – Spring Semester 2026

Lower Division Calculus-based Thermodynamics complete courses with lab and lectures – Summer Semester 2026, Spring Semester 2026

Part Time Community College Instructor, Cypress College, Department of Physics and Astronomy.

Lower Division Calculus-based Electrodynamics complete courses with lab and lectures – Spring Semester 2026

Part Time Community College Instructor, Grossmont College, Department of Physics and Astronomy.

Lower Division Calculus-based Electrodynamics complete courses with lab and lectures – Spring Semester 2026

Introduction to Physics – Summer Semester 2026, Spring Semester 2026

Part Time Community College Instructor, Norco College, Department of Physics and Astronomy.

Introduction to Physics – Summer Semester 2026

Teaching Assistant, University of California Irvine, Department of Physics and Astronomy. Upper Division Classical Mechanics, Professor Steven Barwick, Fall 2022

Lower Division Calculus-based E&M Laboratory, Professor Simona Murgia, Spring 2022
Conservation Lower Division Waves Laboratory, Professor Michael Cooper, Fall 2017
Conservation Lower Division Calculus-based Classical Mechanics, Professor Arnold Guerra, Fall 2021

Undergraduate Advising, University of California Irvine, Department of Physics and Astronomy Research Development Leadership – Summer 2022

Letters of Recommendation – Fall 2023 and Winter 2024

Teaching Assistant, University of California Riverside, STEM Academy Single Variable Calculus – Summer 2019

PUBLICATIONS

Cao, E., Cain, D., Silva, S., & Siwy, Z. S. (2024). Ion concentration polarization tunes interpore interactions and transport properties of nanopore arrays. *Advanced Functional Materials, 34*(11), 2312646. https://doi.org/10.1002/adfm.202312646

Cain, D., Cao, E., Vlassiouk, I., Schäffer, T. E., & Siwy, Z. S. (2025). Ion concentration polarization causes a nearly pore-length-independent conductance of nanopores. *Faraday Discussions, 257*, 344–359. https://doi.org/10.1039/D4FD00148F

Barajas-Aguilar, A. H., Schiel, M., Cao, E., Cain, D., Berrens, M. L., Aydin, F., Pham, T. A., Sanchez-Yamagishi, J., & Siwy, Z. S. (2026). Electrostatic gating of ionic conductance through heterogeneous van der Waals nanopores. *ACS Nano, 20*(25), 18207–18218. https://doi.org/10.1021/acsnano.6c03174

Cho, A. D., Wawrzkiewicz-Jałowiecka, A., Dewi, C. E. P., Tang, S., Cain, D., Cao, E., Martens, C., Schäffer, T. E., Cervera, J., Ramirez, P., Mafe, S., & Siwy, Z. S. (2025). Nanopores with ionic memory in oscillating ion current signals. *Journal of the American Chemical Society, 147*(51), 47559–47572. https://doi.org/10.1021/jacs.5c16779

FELLOWSHIPS AND AWARDS

GAANN Fellowship, University of California Irvine, 2024-2025
Rose-Hill Foundation Fellowship, University of California Irvine, 2024-2025
Regents Fellowship, University of California Irvine, 2021-2022
Diversity Equity and Inclusion Fellowship, University of California Irvine, 2022-2023

GEM Fellowship, The National GEM Consortium, 2023-2024
California Alliance for Minority Participation Scholarship 2020-2021
Riverside City College Foundations Scholarship Mathematics 2019
Riverside City College Foundations Scholarship Physics 2019

PRESENTATIONS

"Ionic Concentration Polarization causes nearly pore length independent conductance in nanopores" Poster presentation delivered at the Anaheim Convention Center, American Physical Society – March Meeting (APS) 2025, Anaheim, California, March 2025
"The effects of gold polarization near the opening of a nanopore array" Poster presentation delivered at the Boston Burlington Hotel, COMSOL Conference 2024, Boston, Massachusetts, October 2024

"Near pore length conduction independence in nanopore arrays," Poster presentation delivered at the Hyatt Regency Houston Downtown, 2024 National Society of Black Physicists Conference (NSBP), Houston, Texas, November 2024

"Near pore length conduction independence in nanopore arrays," Poster presentation delivered at the Double Tree by Hilton, NSF AGEP 25, Arlington, Virginia, October 2024

"Ion Concentration Polarization Tunes Interactions Between Nanopores and Transport Properties of Nanopore Arrays," Poster presentation delivered at the Knoxville Convention Center, 2023 National Society of Black Physicists Conference, Knoxville, Tennessee, October 2023

"Development of NxN Droplet Interface Bilayer Systems for Neuromorphic Computing Devices," Oral Presentation delivered at Oak Ridge National Laboratory, 2023 ORNL GEM Conference, Oak Ridge, Tennessee, August 2023

"Tuning Interactions in Nanopore Arrays with Charges on the Pore Walls," Poster presentation delivered at the 2023 Annual Biophysical Society Meeting, San Diego, CA, February 2023

"Probing Interactions Between Nanopores in an Array," Tahoe Nanofluidics 2022 Conference, Tahoe City, CA, May 2022

"Characterization of Evening Circadian Clock Genes in Fairchild Mandarin," RISE 2019 Conference, Riverside, CA, September 2019

ACADEMIC SERVICE AND OUTREACH

Young African American Science Foundation (Founder), November 2023
Cal Bridge, October 2021 to October 2023
Department of Physics and Astronomy Diversity Equity and Inclusion
National Society of Black Physicists (Vice President),
EmpowHER (Mentor and Speaker)

California Alliance of African American Parents
California Alliance for Minority Participation
Peers Offering Wellness Education Resources
Physics Graduate Caucus (Teaching Assistant Representative)
Dynamic Genome Group (High School Outreach)

ABSTRACT OF THE DISSERTATION

Modeling Small Nanopore Arrays for Biomimetic Ionotronics

by

DaVante DeVon Lee Cain

Doctor of Philosophy in Physics

University of California, Irvine, 2026

Professor Zuzanna Siwy, Chair

Solid-state nanopores provide a versatile platform for controlling ionic transport at the nanoscale and represent promising building blocks for biomimetic iontronic devices. However, while transport through isolated nanopores is relatively well understood, the behavior of small nanopore arrays cannot necessarily be predicted by treating individual pores as independent conductors. Ion concentration polarization (ICP), characterized by the formation of ion-depleted and ion-enriched regions adjacent to ion-selective nanopores, extends beyond the physical boundaries of a pore and can therefore mediate interactions among neighboring pores and surfaces. This dissertation investigates how ICP, nanopore geometry, surface charge, interpore spacing, electrolyte concentration, and neighboring electrostatic boundary conditions collectively govern ionic transport through single nanopores and small nanopore arrays.

Ionic transport was investigated experimentally using nanopores fabricated in silicon nitride membranes and computationally using three-dimensional finite-element models based on the coupled Poisson–Nernst–Planck equations. Two- and three-pore arrays were examined as functions of interpore distance and electrolyte concentration, while numerical simulations resolved the spatial distributions of ionic concentration, electrostatic potential, ion selectivity,

and ionic current. Additional models examined the effects of nanopore length, patterned surface charge, and neighboring conductive surfaces under floating-potential, fixed-charge, and externally applied gate-potential boundary conditions.

The results demonstrate that ICP is a central mechanism governing interactions among nanoscale ionic transport elements. Closely spaced nanopores develop overlapping depletion regions that suppress array conductance, with stronger coupling observed at lower electrolyte concentrations. ICP also produces a regime in which nanopores with substantially different physical lengths exhibit similar conductance because ion-depleted regions extending beyond the pore contribute significantly to the total transport resistance. Spatially patterned surface charge redistributes ICP and produces diode-like transport, whereas neighboring conductive surfaces modify depletion and enrichment through electrostatic coupling. Applied gate potentials provide further control over these distributions and generate spatially heterogeneous transport responses within small nanopore arrays.

Collectively, these results establish that nanopore conductance is determined not solely by pore geometry and intrinsic surface properties but also by the surrounding electrochemical environment. Consequently, small nanopore arrays can exhibit collective transport behavior that cannot be described as a simple parallel combination of independent nanopores. These findings provide physical design principles for controlling coupled ionic transport and developing nanopore-based diodes, gates, selective membranes, and biomimetic iontronic circuits.

CHAPTER 1 Nanopores in Nature and Ionic Circuitry

Nanopores are nanoscale channels that regulate the transport of ions, molecules, and solvent between spatially separated environments. Although broadly defined as pores having at least one characteristic dimension below 100 nm, their importance extends beyond their physical dimensions. As the characteristic dimensions of a pore decrease, the surface-area-to-volume ratio increases substantially, causing interfacial interactions to become increasingly important. Consequently, transport through nanopores can differ fundamentally from transport through macroscopic channels, where bulk solution properties often dominate. Recent advances in nanofabrication and nanoscale characterization have enabled systematic investigation of these effects and established nanofluidics as a rapidly developing field spanning molecular sensing, selective separations, energy conversion, and ionic information processing.[1]

For electrolyte solutions confined within nanopores, surface charge and the associated electrostatic environment can strongly modify local ionic distributions. Charged pore surfaces attract counterions and repel coions, producing an electric double layer (EDL) adjacent to the pore walls. When characteristic pore dimensions approach relevant electrostatic screening lengths, a substantial fraction of the electrolyte contained within the nanopore can be influenced by these interfacial interactions. Ionic transport is therefore determined not only by bulk conductivity and pore geometry but also by surface charge, electrostatic screening, ion selectivity, and the spatial distribution of ions within and surrounding the nanopore.[1]

Under an applied transmembrane potential, these effects can produce strongly nonlinear transport behavior. Selective transport through a charged nanopore can generate ion-enriched and ion-depleted regions near opposing pore entrances, a phenomenon known as ion concentration polarization (ICP).[2–4] Because the concentration of mobile charge carriers determines the local

conductivity of the electrolyte, enrichment and depletion can substantially modify the total electrical resistance of the nanopore system. Importantly, ICP is not necessarily confined to the physical boundaries of the nanopore. Concentration gradients can extend into the surrounding reservoirs, allowing nanopore transport to depend on an electrochemical environment extending well beyond the pore itself.[2–4]

These properties enable nanopores to exhibit ionic selectivity, ion-current rectification, nonlinear conductance, electrostatic gating, and history-dependent transport. Such phenomena have motivated nanopore systems for applications including molecular sensing, desalination and selective separations, osmotic energy conversion, and ionic circuitry.[1,5,6] At the same time, the nonlocal nature of nanoscale ionic transport raises an important fundamental question: when several nanopores occupy the same local electrochemical environment, can their transport properties still be understood independently?

The research presented throughout this dissertation addresses this question using solid-state nanopores, with particular emphasis on nanopores fabricated in silicon nitride membranes. The conceptual foundation for controlling ionic transport at nanometer length scales, however, originates largely from biological systems. Living organisms employ nanoscale channels to achieve remarkable control over water and ionic transport, allowing cellular membranes to perform selective transport, electrochemical signaling, gating, and information processing. Biological nanopores therefore provide both physical insight and functional inspiration for synthetic nanopore systems and biomimetic iontronic devices.

1.1 Biological Nanopores and Molecular Selectivity

Biological membranes contain diverse protein-based channels responsible for regulating the transport of water, ions, and other molecular species between cells and their surrounding

environments. Despite dimensions of only a few nanometers, these channels can combine high permeability with exceptional molecular or ionic selectivity. Their performance arises from combinations of geometric confinement, electrostatic interactions, chemical functionality, molecular recognition, and conformational changes in channel structure.[7–9]

Aquaporins and ion-selective channels provide two particularly instructive examples. Although their microscopic transport mechanisms differ substantially, both illustrate a principle that is central to synthetic nanofluidic systems: at nanometer length scales, small variations in geometry, charge distribution, and interfacial chemistry can produce large changes in transport.

Aquaporins are transmembrane protein channels that facilitate rapid water transport across biological membranes while strongly restricting proton transport and, for classical water-selective aquaporins, ionic permeation.[7,8] Their selectivity results from a combination of nanoscale confinement and precisely organized chemical and electrostatic interactions within the channel.

The constricted regions of aquaporins impose strong steric constraints on permeating species, but geometric exclusion alone does not explain their selectivity. The arrangement of amino acid residues within the channel creates a local chemical and electrostatic environment that controls the orientation and coordination of water molecules during permeation. Structural features within the pore also interrupt the continuous hydrogen-bonded configurations required for efficient proton hopping, allowing rapid water permeation without dissipating transmembrane proton gradients.[8]

Aquaporins therefore demonstrate how confinement and local interfacial chemistry can be combined to produce highly selective molecular transport without a macroscopic mechanical barrier. More broadly, they illustrate a recurring principle of nanoscale transport: when a channel

approaches molecular dimensions, the interface between the transported species and the channel becomes an active component of the transport mechanism rather than merely a passive boundary. Synthetic nanopores generally lack the atomistic precision and conformational complexity of biological proteins. Nevertheless, analogous physical principles can be introduced through control of pore dimensions, surface chemistry, surface charge, and externally applied electric fields. These approaches provide routes for manipulating ionic transport using comparatively simple and mechanically robust solid-state structures.[1]

Biological ion channels provide an even more direct analogy to the solid-state nanopores considered in this dissertation. Potassium, sodium, calcium, and chloride channels regulate ionic transport across cellular membranes and can discriminate strongly among competing ionic species. Such selectivity arises from combinations of confinement, local electrostatic interactions, dehydration energetics, and chemically specific coordination within selectivity filters.[9–11]

Potassium channels provide a canonical example. Structural determination of the KcsA potassium channel revealed a narrow selectivity filter lined by backbone carbonyl oxygen atoms positioned to coordinate permeating K^+ ions. [9–11] Passage through this region requires substantial reorganization of the ion's hydration environment. The geometry and chemical coordination of the selectivity filter compensate effectively for this energetic cost for K^+ while strongly discriminating against Na^+ despite its smaller ionic radius. [9–11]

Two-part comparison of molecular selectivity in biological nanopores. Panel (a) shows an aquaporin water channel and the molecular interactions responsible for selective water transport, including size restriction, electrostatic repulsion, and dipole inversion. Panel (b) shows the KcsA potassium channel and its selectivity filter, where potassium ions occupy defined binding sites

and alternate with water molecules during conduction.

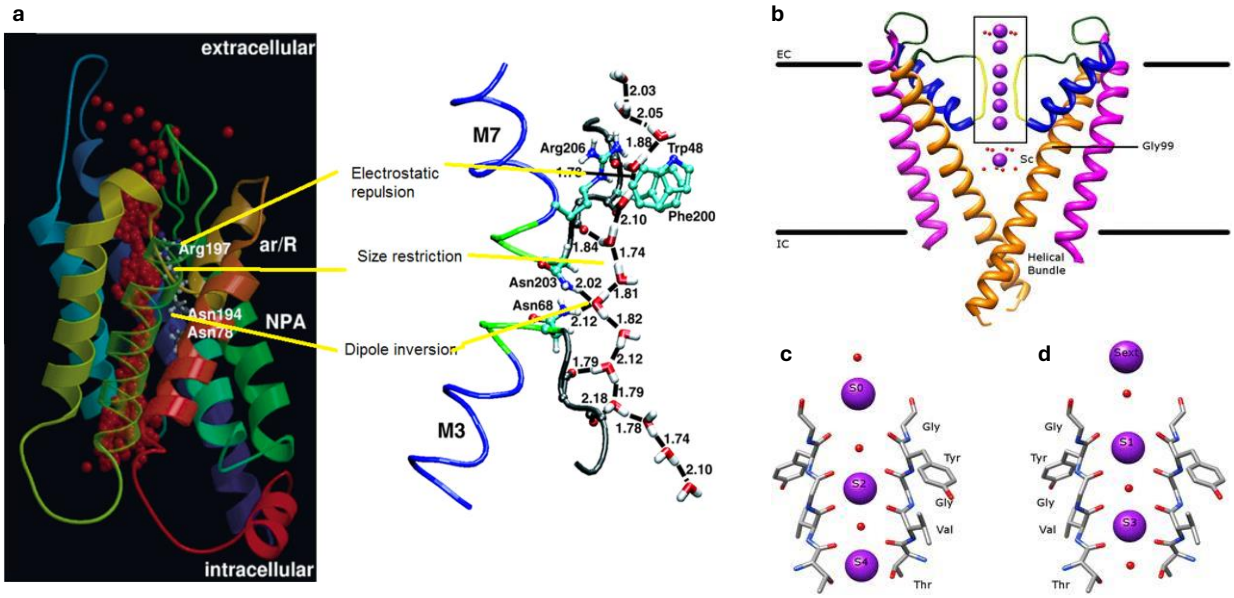

Figure 1.1 Molecular Selectivity in Biological Nanopores. (a) Aquaporin water channels facilitate highly selective water transport through molecular-scale confinement and precisely organized chemical and electrostatic interactions while suppressing ionic and proton transport. (b) Structure and selectivity filter of the KcsA K^+ channel from *Streptomyces lividans*. K^+ selectivity arises within the narrow selectivity filter, where permeating K^+ ions are stabilized by coordination with backbone carbonyl oxygen atoms. The S1–S4 binding sites provide an energetically favorable pathway for K^+ permeation, with K^+ ions and water molecules occupying alternating positions during conduction, while strongly discriminating against competing ions such as Na^+. Adapted from[7,12].

This mechanism demonstrates that nanoscale ion selectivity cannot generally be understood from steric size alone. Instead, selectivity emerges from the free-energy landscape generated by confinement, solvation, chemical coordination, and electrostatic interactions. Although continuum models of solid-state nanopores do not reproduce the atomistically specific binding and dehydration processes present in biological proteins, the broader principle remains

directly relevant: the local environment experienced by an ion can determine whether its transport is energetically and kinetically favorable. Surface charge, nanoscale confinement, electrolyte composition, and externally imposed electrostatic potentials can therefore be engineered in solid-state nanopores to control ion distributions and transport. These principles provide the first connection between biological ion channels and engineered nanofluidic devices. A second and particularly important connection emerges when individual channels are considered not in isolation but as components of larger interacting systems.

1.2 Collective Ionic Transport in Biological Systems

The functionality of biological membranes does not arise solely from the properties of individual ion channels. Many biological processes instead depend on coordinated transport through populations of channels whose states and ionic currents collectively determine the electrical and chemical response of the membrane.

The propagation of an action potential provides a prominent example. Classical electrophysiological studies established that voltage-dependent sodium and potassium conductances underlie the generation and propagation of action potentials.[13,14] When a region of an excitable membrane becomes sufficiently depolarized, voltage-gated sodium channels open and generate inward ionic current. The resulting local circuit current depolarizes adjacent membrane regions, promoting activation of neighboring voltage-gated channels and allowing the electrical disturbance to regenerate along the axon. [13,14]

This mechanism should be distinguished from the direct ICP-mediated coupling investigated later in this dissertation. Neighboring neuronal channels do not interact simply because concentration-depletion regions overlap in the same manner as closely spaced solid-state

nanopores. Nevertheless, biological signal propagation illustrates a broader principle motivating the present work: the functional response of an individual ionic transport element can depend on changes in its electrochemical environment generated by other elements within the system.

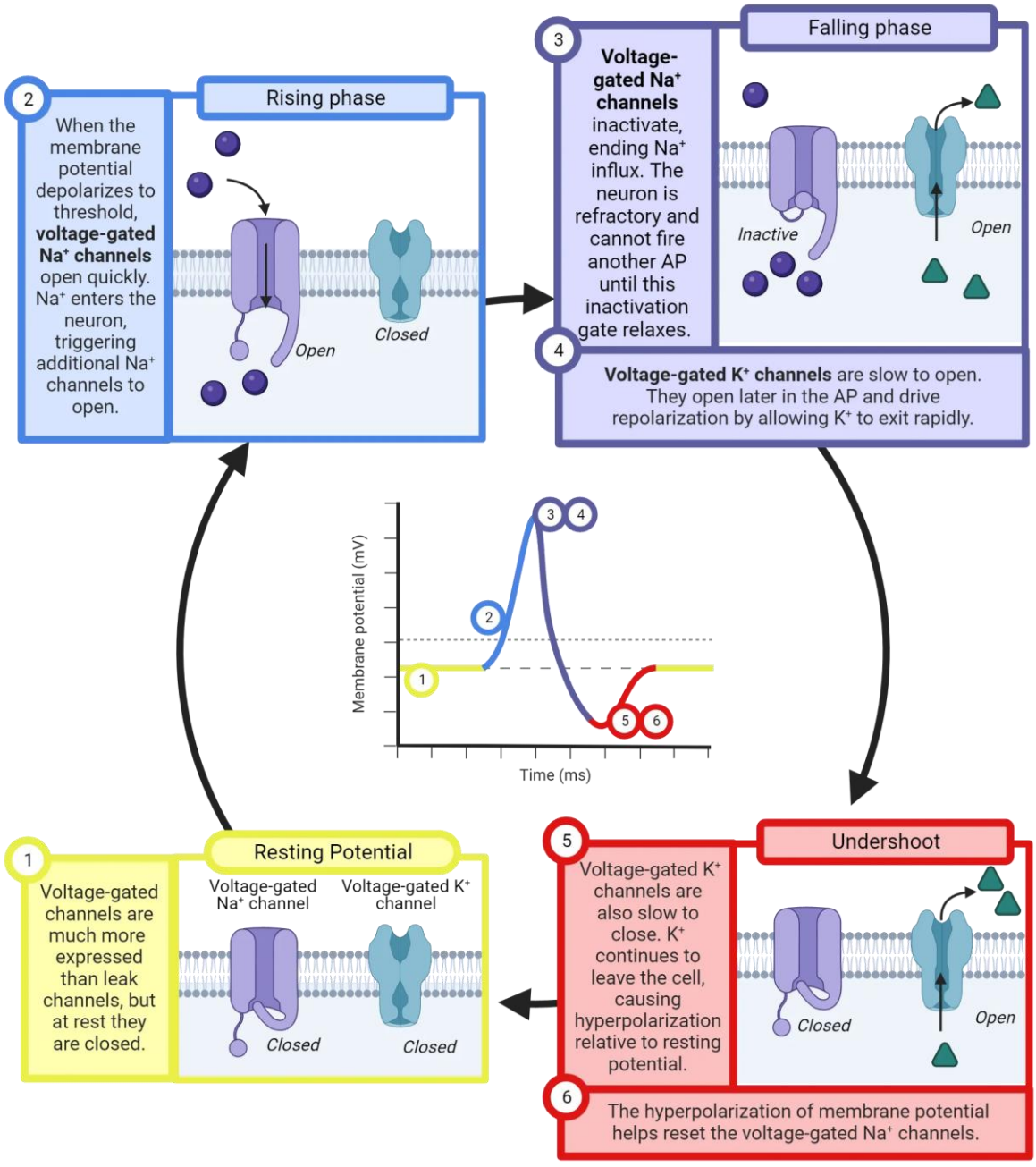

Figure 1.2 Voltage-gated Na^+ and K^+ Channel Dynamics During Neuronal Action-Potential Generation. At the resting membrane potential, voltage-gated Na^+ and K^+ channels remain

closed. Upon reaching the threshold potential, voltage-gated Na^+ channels rapidly open, producing Na^+ influx and membrane depolarization. Near the peak of the action potential, Na^+ channels inactivate while the more slowly activated voltage-gated K^+ channels open. The resulting K^+ efflux drives membrane repolarization. Because K^+ channels close more slowly, continued K^+ efflux produces a transient hyperpolarization before the membrane returns to its resting potential. The coordinated gating of Na^+ and K^+ channels therefore produces the characteristic action-potential waveform. Reproduced from OpenStax, *Introduction to Behavioral Neuroscience*, Figure 2.27. Copyright Rice University, OpenStax, under CC BY-NC-SA 4.0 license.

From this perspective, biological membranes can be regarded as sophisticated ionic networks. Individual channels provide selective conduction, voltage-dependent gating, and other nonlinear transport functions, whereas their collective organization enables signal generation, propagation, and processing. Unlike conventional electronic circuits, in which information is predominantly carried by electrons or holes in solid conductors and semiconductors, biological systems rely extensively on ionic motion, electrochemical gradients, and dynamically evolving membrane potentials.

The ability of biological systems to generate complex functionality from interacting ionic transport processes provides strong motivation for constructing synthetic systems capable of manipulating ions in related ways. Solid-state nanopores offer a particularly useful platform because their geometry, surface properties, spatial arrangement, and electrostatic boundary conditions can be engineered systematically.

1.3 Solid-State Nanopores and Nanofluidic Devices

Synthetic nanopores have been fabricated in a broad range of materials, including polymers, silicon-based dielectrics, oxides, and atomically thin materials.[1] Fabrication methods include ion-track etching, focused ion and electron beams, dielectric breakdown, lithographic approaches, and direct drilling or sculpting using charged-particle beams. [1]

A landmark development in solid-state nanopore technology was reported by Li and co-workers in 2001, who used low-energy ion-beam sculpting to fabricate a molecular-scale nanopore in a thin Si_3N_4 membrane and demonstrated detection of individual DNA molecules through the resulting solid-state pore.[15] This work established silicon nitride as an important platform for robust nanoscale ionic transport and single-molecule sensing.

Electron-beam-based approaches subsequently provided direct visual feedback and increasingly precise control over nanopore dimensions. Storm and co-workers demonstrated transmission-electron-microscopy-based fabrication of solid-state nanopores with single-nanometer precision in silicon oxide in 2003.[16] In 2006, Kim and co-workers demonstrated rapid fabrication of uniform 2–20 nm nanopores and nanopore arrays directly in Si_3N_4 membranes using a high-intensity electron beam in a transmission electron microscope.[17] The latter approach enabled controlled fabrication of multiple closely spaced pores and is particularly relevant to the small nanopore arrays considered in this dissertation.

Silicon nitride has remained an important material for solid-state nanopore research because of its mechanical robustness, compatibility with thin freestanding membranes, and compatibility with established micro- and nanofabrication methods.[1] The systems considered throughout this dissertation primarily consist of nanoscale pores formed in silicon nitride membranes separating two electrolyte reservoirs. Depending on solution conditions and surface

chemistry, the nanopore walls acquire surface charge, which alters local ionic distributions and can produce preferential transport of counterions relative to coions.

Application of a transmembrane voltage drives ionic flux through the nanopore. When transport is sufficiently ion-selective, the resulting flux can modify the concentrations near the nanopore entrances and generate ICP.[2–4] A depleted region is particularly important because its reduced concentration of mobile charge carriers produces increased local electrical resistance. Consequently, a substantial fraction of the total resistance measured for a nanopore system can originate outside the geometrical pore.

Cain et al. demonstrated this nonlocal contribution directly by examining nanopores with different physical lengths.[3] Despite large differences in pore length, the nanopores could exhibit nearly identical conductance because ICP and the associated access-region resistance contributed substantially to the total resistance of the system. The result demonstrates that the effective electrical dimensions of a nanopore need not coincide with its geometrical dimensions and emphasizes the importance of the surrounding electrolyte in determining nanoscale transport.

Redistribution of ions can also produce asymmetric current–voltage characteristics. When the magnitude or spatial distribution of enrichment and depletion differs between opposite voltage polarities, the resulting ionic current can rectify. Nanopores exhibiting ion-current rectification therefore function as ionic analogues of electronic diodes, providing one of the fundamental nonlinear elements used in nanofluidic and iontronic systems.[5,18]

Although isolated nanopores provide the simplest platform for understanding these phenomena, practical nanoporous membranes and integrated nanofluidic devices frequently contain multiple transport pathways. Once the spatial extent of the electrochemical perturbation

generated by one pore becomes comparable to the separation between neighboring pores, the assumption of independent transport must be reconsidered.

1.4 From Individual Nanopores to Small Nanopore Arrays

For sufficiently separated identical nanopores, the simplest description of an array treats each pore as an independent conductor. Under this approximation, the total ionic current through an array containing (N) identical pores is

$$I_{array} \approx NI_{single}$$

where I_{array} is the current through an isolated nanopore under otherwise identical conditions. This description implicitly assumes that the concentration and electrostatic environment experienced by each pore remains unaffected by neighboring pores.

Recent experimental and computational results demonstrate that this assumption can fail when nanopores are sufficiently close. Cao, Cain, Silva, and Siwy investigated minimal arrays containing two and three nanopores in silicon nitride membranes with interpore separations ranging from approximately 15 to 200 nm.[2] The experiments and three-dimensional continuum simulations showed that neighboring nanopores interact through overlapping ion-depletion regions generated by ICP. As interpore separation decreased, overlap between depletion zones suppressed the total array current relative to the value predicted by linear superposition of independent single-pore currents. The interaction was additionally controlled by electrolyte concentration and applied voltage.[2]

These results establish that nanopore coupling can be mediated through the electrolyte itself. A nanopore occupies only a small volume within the membrane, yet the concentration distribution generated by selective transport can extend substantially farther into the reservoirs.

When the depletion region generated by one pore extends into the transport environment of another, the neighboring pore no longer experiences the same electrochemical conditions as an isolated pore. Its conductance consequently becomes dependent on both its intrinsic properties and the collective state of the array.[2]

More recent modeling of multi-nanopore membranes has further demonstrated that pore number, spacing, and surface-charge configuration can determine the magnitude of these interactions and the deviation of array current from the independent-pore approximation.[19] In particular, the strength of coupling depends on the ability of individual pores to generate substantial ICP, emphasizing that interpore distance alone is insufficient to characterize array behavior. This leads to a central question addressed throughout this dissertation: When does a nanopore cease to behave as an independent ionic transport element?

The answer depends on several coupled physical parameters. Interpore separation determines the extent to which neighboring concentration distributions can overlap. Electrolyte concentration controls electrostatic screening and strongly influences ion selectivity and ICP. Surface charge determines interactions between the nanopore and mobile ions. Nanopore geometry controls the relative contributions of internal pore resistance and external concentration polarization. Applied voltage determines both the magnitude and direction of ionic flux.[2,3]

Importantly, coupling does not require all nanopores within an array to exhibit identical transport behavior. Differences in surface charge, spatial position, geometry, or electrostatic environment can cause pores within the same membrane to experience distinct local concentration and potential distributions. The functional response of an individual nanopore may therefore emerge from its position and interactions within the larger array rather than being determined solely by its isolated properties.

This concept has consequences for both nanoporous membranes and ionic circuitry. For membrane applications, interpore interactions can cause total conductance to deviate from the value predicted from isolated-pore measurements. For iontronic applications, however, the same coupling represents an opportunity. If interactions can be understood and deliberately controlled, the surrounding electrochemical environment becomes an additional design variable for determining the functionality of individual nanoscale transport elements.

1.5 Nanopores as Iontronic Circuit Elements

The controlled manipulation of ionic rather than electronic transport forms the basis of the emerging field of iontronics. Iontronic devices regulate the transport, accumulation, depletion, and redistribution of ionic species to perform functions analogous to components of electronic circuits. Recent developments have expanded the field from individual ionic diodes and gated channels toward memory, logic, neuromorphic architectures, and integrated ionic circuits.[6,20,21]

Individual nanofluidic structures can exhibit behaviors analogous to familiar circuit elements. A nanopore displaying an approximately symmetric current–voltage response can, over an appropriate operating range, be treated as an ionic resistor. A nanopore exhibiting strongly asymmetric current–voltage characteristics can function as an ionic diode. [5,18] Ionic conductance can also be modulated through electrostatic gating, producing transistor- or switch-like behavior. Systems in which the instantaneous conductance depends on the previous ionic or structural state can exhibit memristive behavior and provide physical analogues of synaptic memory.[6,20]

Recent experiments have moved these concepts beyond isolated components. Emmerich et al. demonstrated nanofluidic mechano-ionic memristive switches and assembled interacting

devices into logic circuits, illustrating the potential for circuit-scale ionic information processing.[20] Contemporary work on bioinspired nanofluidic iontronics similarly emphasizes the potential of confined ionic systems for artificial neurons, synaptic behavior, and brain-inspired computing.[6]

Despite these analogies, ionic devices differ fundamentally from conventional electronic circuit elements. Their charge carriers reside within a mobile electrolyte whose local concentration can evolve during device operation. Consequently, the conductivity of the transport medium itself can change dynamically. Ionic enrichment increases the local availability of charge carriers, whereas ionic depletion increases local resistance. These concentration distributions may also extend beyond the physical boundaries of an individual device.[2,3,5]

This distinction becomes particularly important when multiple nanofluidic elements are integrated within a small spatial region. In conventional circuit descriptions, individual components can often be assigned approximately independent constitutive relationships and connected through well-defined nodes. In nanoscale ionic systems, neighboring components may instead share concentration and electrostatic fields. Integration can therefore modify the characteristics of the individual components themselves.

For example, a nanopore that exhibits one current–voltage response in isolation may exhibit a substantially different response when positioned near another nanopore or an electrostatically active surface.[2] A nearby charged or conductive interface can redistribute ions near the nanopore entrance, modifying depletion or enrichment and thereby changing ionic current. If the neighboring surface is electrically addressable, its potential provides an additional mechanism for controlling transport.

This coupling creates both a challenge and an opportunity for ionic circuit design. Reliable iontronic devices require an understanding of when individual elements can be treated independently and when collective interactions dominate. Conversely, deliberately engineered coupling may allow functionality to emerge from comparatively simple nanopore geometries. Closely spaced pores can therefore serve not merely as replicated conduction pathways but as interacting elements whose transport characteristics depend on their collective electrochemical state.

Such behavior is particularly relevant to biomimetic iontronics. Biological systems achieve sophisticated functionality not simply from individual channels but through the organization and regulation of many transport elements within shared electrochemical environments. Synthetic nanopore arrays need not reproduce biological channels at the molecular level to exploit a related design principle. Instead, control over geometry, surface charge, concentration polarization, interpore spacing, and external electrostatic boundaries may provide a route toward engineering collective ionic behavior using robust solid-state structures.

1.6 Knowledge Gap and Motivation

Extensive research has established many of the fundamental mechanisms governing transport through isolated nanopores, including surface-charge-dependent selectivity, electric-double-layer effects, ion-current rectification, and ICP.[1,5] Considerably less straightforward is the behavior of small nanopore arrays in regimes where the electrochemical perturbation produced by one transport element extends into the environment of another.[2,19]

The observation of ICP-mediated interpore coupling demonstrates that increasing the number of nanopores does not necessarily produce a proportional increase in membrane current.[2]

Moreover, the observation of nearly pore-length-independent conductance demonstrates that the electrochemical region determining nanopore resistance can extend substantially beyond the geometrical boundaries of the pore. Taken together, these findings suggest that nanopore transport must be understood as a property of the coupled pore–surface–electrolyte system, rather than as a property of pore geometry alone.

Several fundamental questions consequently remain. First, the characteristic separation at which neighboring nanopores cease to behave independently must be related to electrolyte conditions, surface properties, and the spatial extent of ICP. Second, when interactions occur, it is necessary to determine whether they simply modify total array current or whether individual pores can acquire distinct transport functions. Third, the role of nanopore geometry must be reconsidered when substantial transport resistance originates from concentration-depleted regions outside the physical pore. Finally, if nanopore transport is sensitive to its surrounding electrochemical environment, nearby charged or conductive surfaces may provide a mechanism for deliberately controlling individual pores.

Addressing these questions is necessary for developing a physical description of small nanopore arrays that extends beyond the independent-pore approximation. It is also necessary for determining whether collective nanopore interactions can be exploited rather than merely minimized. A predictive understanding of such coupling could provide design principles for arrays in which the transport function of an individual nanopore is controlled through its geometry, neighbors, surface properties, and surrounding electrostatic boundary conditions.

1.7 Objectives and Central Thesis of This Dissertation

The central objective of this dissertation is to determine how ion concentration polarization and electrostatic coupling govern ionic transport through small solid-state nanopore arrays and to establish how these interactions may be controlled to produce functional iontronic behavior.

This dissertation addresses six interconnected questions concerning the mechanisms governing ionic transport in small nanopore arrays:

1. Under what conditions do neighboring nanopores cease to behave as independent ionic conductors and instead exhibit coupled transport behavior?
2. How do interpore spacing and electrolyte concentration determine the magnitude and spatial extent of ion concentration polarization (ICP)-mediated interactions between neighboring nanopores?
3. How does nanopore geometry, particularly pore length, influence ionic conductance when a significant fraction of the total transport resistance originates from concentration polarization outside the physical nanopore?
4. How do nearby charged and conductive surfaces modify local ion concentration polarization and, consequently, ionic transport through a nanopore?
5. Can externally applied electrostatic potentials actively regulate ionic transport through individual nanopores and produce spatially heterogeneous transport responses within small nanopore arrays?
6. Can these collective and actively controlled transport behaviors be interpreted as functional ionic circuit elements, including resistors, diodes, and electrostatic gates?

Together, these questions test the central hypothesis that ion concentration polarization provides a mechanism through which nanoscale ionic transport extends beyond the physical

boundaries of individual nanopores. Consequently, nanopores and neighboring surfaces can become electrostatically and diffusively coupled over nanometer-scale distances, enabling collective transport phenomena that are absent in isolated-pore descriptions. Understanding and controlling these interactions provides a foundation for engineering small nanopore arrays with spatially differentiated and externally tunable transport characteristics, ultimately enabling their development as functional components of biomimetic iontronic circuits.

The central thesis of this dissertation is that nanopores within small arrays cannot, under sufficiently strong concentration and electrostatic coupling, be treated as independent ionic conductors. ICP extends the influence of a nanopore beyond its physical boundaries, allowing neighboring pores and surfaces to modify its local electrochemical environment and, consequently, its transport response.[2,3] These interactions can suppress or enhance ionic current, modify ion-current rectification, alter the apparent dependence of conductance on pore geometry, and produce spatially distinct transport behavior among nanopores within the same array. Control over geometry, surface charge, electrolyte concentration, spatial arrangement, and electrostatic boundary conditions therefore provides a means of engineering coupled nanoscale ionic transport.

1.8 Organization of the Dissertation

The remainder of this dissertation develops this argument progressively, beginning with the physical description of nanoscale ionic transport and advancing toward increasingly complex coupled nanopore systems.

Chapter 2 establishes the theoretical and computational framework used throughout the dissertation. The governing principles of diffusion, electromigration, electrostatics, electric-

double-layer formation, ion selectivity, and ICP are introduced, followed by the coupled Poisson–Nernst–Planck framework used to model ionic transport. Particular attention is given to the assumptions and boundary conditions required to represent solid-state nanopores and their surrounding electrolyte environments.

Chapter 3 investigates interactions among closely spaced nanopores and establishes the role of overlapping ICP regions in producing nonadditive conductance in small nanopore arrays.[2] The dependence of these interactions on interpore spacing and electrolyte concentration provides a physical basis for identifying conditions under which the independent-pore approximation fails. The subsequent research chapters extend this framework by examining how pore geometry, surface-charge distributions, spatial arrangement, and neighboring electrostatic boundaries modify ionic transport. In particular, the dependence of nanopore conductance on physical pore length is reconsidered when ICP contributes substantially to the total electrical resistance.[3] The influence of neighboring charged and conductive surfaces is then examined as a means of extending passive pore–pore coupling toward deliberate electrostatic control of depletion, enrichment, rectification, and individual nanopore transport responses.

Together, these studies establish a unified description of small nanopore arrays as coupled ionic transport systems. Rather than treating each nanopore as an isolated device whose function is determined entirely by its internal geometry and surface properties, this dissertation demonstrates the importance of the surrounding electrochemical environment in determining nanoscale transport. This perspective provides a foundation for designing solid-state nanopore systems in which collective interactions are intentionally controlled to produce functional ionic circuitry.

CHAPTER 2 Ion Transport at the Nanoscale and Continuum Modeling

Nanopores constitute a powerful platform for probing molecular and ionic behavior under extreme nanoconfinement. Within this regime, ionic transport departs fundamentally from the predictions of classical bulk electrolyte theory. At macroscopic length scales, ion transport in aqueous solutions is well described by continuum electrochemical models that assume bulk electroneutrality and spatially uniform material properties. These approximations, however, break down when transport is restricted to nanometer-scale geometries.

Under nanoconfinement, the pronounced surface-area-to-volume ratio elevates interfacial effects to a dominant role in governing system behavior. In particular, charged pore walls strongly modulate the local electrostatic environment, giving rise to overlapping electric double layers, selective ion partitioning, ionic concentration polarization, and highly nonlinear current–voltage responses. These coupled electrostatic and transport phenomena fundamentally redefine ionic conduction in nanopores and cannot be captured within conventional bulk frameworks.

Consequently, understanding and accurately modeling these effects is essential for the design and interpretation of nanofluidic systems. The physical mechanisms described here underpin the operation of nanopore-based devices and are central to the analyses presented throughout this dissertation.

Because the physical dimensions of nanopores are often comparable to the characteristic electrostatic screening length in solution, the assumptions that hold in bulk systems must be revisited. The ionic distributions are no longer spatially uniform near interfaces, and transport can no longer be understood as arising solely from simple diffusion between well-mixed reservoirs. Instead, ion motion becomes governed by the coupled effects of concentration gradients, electric fields, and confinement imposed by the pore geometry and surface charge.

These effects interact in a highly nonlinear way and are often not analytically tractable for realistic device geometries. For this reason, continuum simulations are an essential component of this work.

The purpose of this chapter is therefore twofold. First, it reviews the physical principles governing ionic transport in electrolyte solutions and in charged nanopores. Second, it presents the continuum modeling framework used throughout this dissertation, with particular emphasis on the Transport of Diluted Species interface in COMSOL Multiphysics and its coupling to the Electrostatics interface. While the physical concepts discussed here overlap strongly with those in related nanopore research, the present discussion places greater emphasis on how those concepts are translated into a computational model and how the governing equations are implemented numerically. This emphasis is important because many of the conclusions drawn in later chapters rely on simulated concentration fields, electric potential distributions, and current responses obtained from COMSOL.

2.1 Ions in Aqueous Solution

When a salt dissolves in water, it dissociates into charged species. For the salt potassium chloride, KCl, dissolution produces potassium cations, K^+, and chloride anions, Cl^-. Water, being a polar solvent, stabilizes these ions by orienting its partial charges around them. Oxygen atoms, which carry partial negative charge, orient toward cations, while hydrogen atoms, which carry partial positive charge, orient toward anions. This ordered shell of water molecules surrounding an ion is referred to as the hydration shell. The hydrated state of an ion is important because it influences the ion's effective size, mobility, and transport behavior in solution.

In an unforced system, ions move randomly due to thermal motion and tend toward a spatially uniform concentration distribution. However, if a concentration gradient exists, ions move from regions of high concentration to regions of low concentration through a process referred to as diffusion. The diffusive flux of the i-th ionic species is described by Fick's law,

$$\mathbf{J}_i^{\text{diff}} = -D_i \nabla c_i \tag{2.1}$$

where D_i is the diffusion coefficient of species i, and c_i is its concentration. The negative sign indicates that diffusion acts to reduce concentration gradients. This expression represents one of the most fundamental transport relations in electrolyte theory and also forms the base diffusive term used in the COMSOL transport model.

The diffusion coefficient itself depends on temperature, solvent viscosity, and ion size. For a spherical particle, the Einstein relation gives

$$D_i = \frac{k_B T}{6\pi\eta r_i} \tag{2.2}$$

where k_B is the Boltzmann constant, T is the absolute temperature, η is the dynamic viscosity of the solvent, and r_i is the effective hydrodynamic radius of the ion. This relation indicates that the diffusion coefficient scales linearly with temperature and inversely with both viscosity and ionic size. In aqueous systems at room temperature, these parameters are well established, enabling transport models to be parameterized directly using experimentally tabulated diffusivities or ionic mobilities.

Potassium chloride is employed extensively throughout the experiments and simulations presented in this dissertation due to the near equivalence of the mobilities of potassium and chloride ions. Consequently, the governing transport equations are approximately symmetric with respect to each ionic species, which simplifies both the analytical treatment and numerical implementation of the transport model.

In addition to diffusion, ions respond to electric fields because they carry charge. If an electric field $\mathbf{E}$ is applied, an ion of charge q_i experiences a force

$$\mathbf{F} = q_i\mathbf{E} \tag{2.3}$$

in liquid solution, this electric driving force is balanced by viscous drag. For slow motion in a Newtonian fluid, the drag on a spherical particle is given by Stokes' law,

$$\mathbf{F}_{\text{drag}} = 6\pi\eta r_i\mathbf{v}_i \tag{2.4}$$

where $\mathbf{v}_i$ is the drift velocity of the ion. Balancing electrical and viscous forces gives

$$\mathbf{v}_i = \frac{q_i\mathbf{E}}{6\pi\eta r_i}. \tag{2.5}$$

Substituting the Einstein relation into this expression yields

$$\mathbf{v}_i = \frac{D_i q_i}{k_B T}\mathbf{E}. \tag{2.6}$$

Since ionic flux is the product of concentration and drift velocity, the electro-migrative contribution to ionic flux becomes

$$\mathbf{J}_i^{\text{mig}} = c_i\mathbf{v}_i = \frac{D_i q_i}{k_B T}c_i\mathbf{E}. \tag{2.7}$$

Using the relation $q_i = z_i e$, where $z_i$is ionic valence and $e$is the elementary charge, together with $\mathbf{E} = -\nabla\phi$, where $\phi$is the electric potential, this expression becomes

$$\mathbf{J}_i^{\text{mig}} = -\frac{D_i z_i e}{k_B T}c_i\nabla\phi. \tag{2.8}$$

Combining diffusion and electromigration gives the total ionic flux,

$$\mathbf{J}_i = -D_i\nabla c_i - \frac{D_i z_i e}{k_B T}c_i\nabla\phi. \tag{2.9}$$

This is the **Nernst-Planck equation** for ionic flux in the absence of convection. It describes the two dominant transport mechanisms relevant to the present work: concentration-driven diffusion and field-driven migration. This equation is central to nanopore transport theory and serves as the continuum basis for numerical simulations of ion transport.

It is worth noting that some forms of the Nernst-Planck equation include a third term accounting for convection. In principle, convection may arise from pressure-driven flow or electroosmotic flow. However, in the systems studied in this dissertation, nanoscale confinement and the specific modeling assumptions used in COMSOL justify neglecting bulk convective transport in the transport equations, so that the dominant contributions arise from diffusion and electromigration. This is consistent with the simplifying assumptions often made for confined nanopore transport and with the model configuration employed here.

2.2 Continuum Modeling Approach in COMSOL

To study ionic transport in nanopores with realistic geometries and boundary conditions, this dissertation uses continuum simulations performed in COMSOL Multiphysics. Specifically, the Transport of Diluted Species interface is used to model the evolution of ionic concentrations, and this interface is coupled to electrostatics to account for electric-field-driven transport. The Transport of Diluted Species interface provides a predefined environment for solving mass conservation equations for species transported by diffusion, convection, and, when enabled, migration in an electric field. The interface assumes that the transported species are dilute relative to the solvent, such that solvent properties such as density and viscosity can be treated as constant. As a rule of thumb, the solvent concentration should exceed roughly 90 mol% for this dilute approximation to remain appropriate.

The governing mass conservation equation solved for each species i in the Transport of Diluted Species interface is

$$\frac{\partial c_i}{\partial t} + \nabla \cdot \mathbf{J}_i + \mathbf{u} \cdot \nabla c_i = R_i \tag{2.10}$$

where c_i is the concentration of species i, $\mathbf{J}_i$ is the diffusive or generalized flux, $\mathbf{u}$ is the mass-averaged fluid velocity, and R_i is a source or sink term that may represent reactions. In the present work, the focus is on nonreactive ionic transport, so $R_i = 0$. Furthermore, because the transport is modeled without fluid flow, the convection term is neglected, reducing the governing equation to a diffusion-migration transport problem. COMSOL explicitly allows the convection mechanism to be turned off, leaving a diffusion equation or, when migration is activated, a diffusion-electromigration equation.

When migration in an electric field is activated, COMSOL augments the flux expression to include an electric driving term. The generalized species flux becomes

$$\mathbf{J}_i = -D_i \nabla c_i - z_i u_{m,i} F c_i \nabla V \tag{2.11}$$

where $u_{m,i}$ is the ionic mobility, F is Faraday's constant, and V is electric potential. The mobility and diffusivity are related through the Nernst-Einstein relation,

$$u_{m,i} = \frac{D_i}{RT}, \tag{2.12}$$

where R is the gas constant and T is absolute temperature. This COMSOL formulation is fully consistent with the Nernst-Planck framework and is especially useful because it allows transport to be coupled directly to a separately solved electric potential field.

The importance of emphasizing this modeling framework in the chapter is that it clearly establishes that the simulations are not merely illustrative figures, but are instead numerical solutions to the coupled transport equations governing the system. In other words, the

concentration maps and current responses shown later in the dissertation arise from a finite element implementation of the same physical principles introduced analytically in this chapter.

2.3 Finite Element Formulation and Numerical Implementation

COMSOL solves the transport equations using the **finite element method (FEM)**. In this numerical approach, the computational domain is divided into many small subdomains called elements. Within each element, the field variables—such as concentration and electric potential—are approximated using interpolation functions. The governing partial differential equations are then converted into a weak form and assembled into a global algebraic system that can be solved numerically.

The strength of the finite element method in nanopore modeling lies in its ability to handle complex geometries, strong gradients, and multiphysics coupling. Nanopores typically involve abrupt changes in confinement and intense field gradients near charged boundaries, especially at pore openings where concentration polarization develops. These features are difficult to capture analytically except under idealized assumptions, but FEM can resolve them numerically with suitable meshing and boundary conditions.

The COMSOL documentation emphasizes that the Transport of Diluted Species interface supports diffusion, convection, and migration in one-, two-, and three-dimensional geometries, including axisymmetric systems. It also supports anisotropic diffusion and can be coupled to electrostatics or current-distribution physics as needed. In this dissertation, that flexibility is critical because nanopore transport depends sensitively on both geometry and the applied potential landscape.

Because steep concentration gradients can arise when electromigration dominates over diffusion, COMSOL also includes stabilization methods such as streamline diffusion and crosswind diffusion for numerically demanding transport problems with high cell Péclet number. This is relevant in nanopore systems subjected to strong applied biases, where ion depletion and enrichment zones may produce sharp spatial transitions in concentration. Even when these stabilization features are not the main scientific focus, acknowledging them strengthens the computational framing of the chapter by demonstrating awareness that the numerical solution of transport equations requires not only correct physics but also stable discretization.

2.4 The Electric Double Layer

The hallmark of nanofluidic transport is the outsized importance of surface charge. When a nanopore wall carries charge, ions in the surrounding electrolyte rearrange in response to that surface. Counterions, which have charge opposite in sign to the wall, accumulate near the interface, while coions are depleted. The resulting charge structure is the **electric double layer (EDL)**, sometimes also referred to as the Debye layer. The EDL is fundamental because it controls ionic selectivity, local conductivity, and the degree to which the pore prefers one ionic species over another.

Simplified model of ion distribution near a charged surface. Cations accumulate near the negative surface charges. Farther from the surface, the local concentration approaches that of the bulk salt concentration. The Deybe Length is inversely proportional to the bulk concentration.

To describe the EDL theoretically, consider a charged planar surface immersed in a symmetric electrolyte. The local concentration of ions can be related to the local electric potential through the Boltzmann distribution,

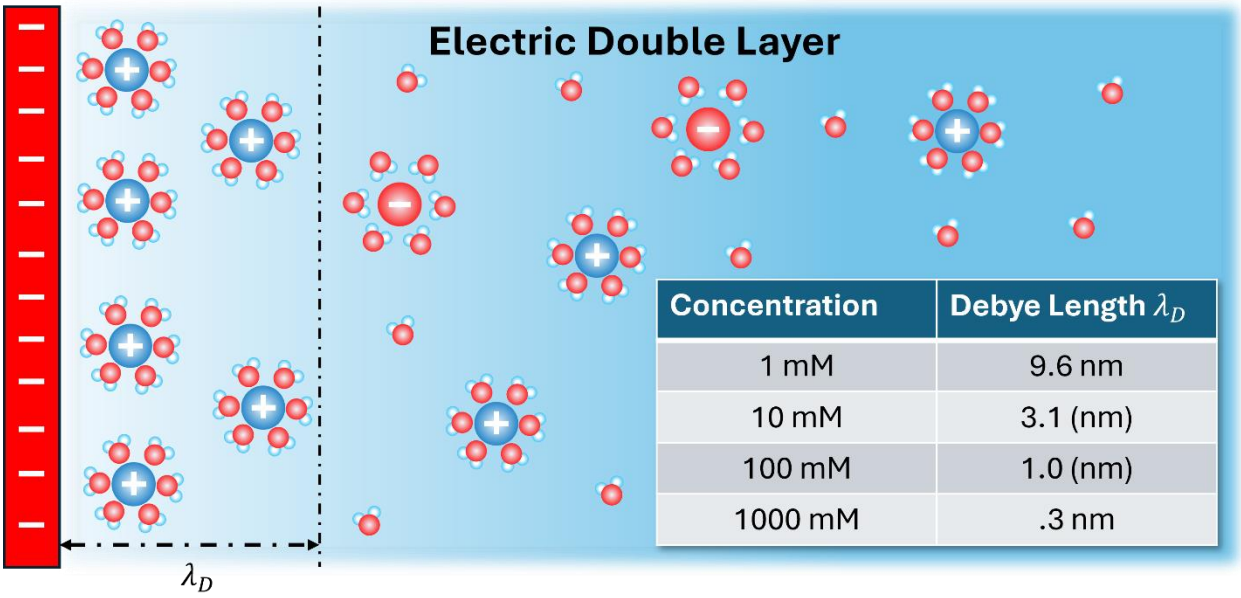

Figure 2.1 The Electric Double Layer and The Debye Length. Schematic representation of the electric double layer (EDL) formed adjacent to a negatively charged surface in an aqueous electrolyte. Counterions accumulate near the charged interface, while coions are depleted, producing a spatially varying ionic distribution that approaches the bulk electrolyte composition with increasing distance from the surface. The characteristic length scale over which the surface potential is screened is described by the Debye Length, (λ_D), which decreases with increasing electrolyte concentration. Representative Debye Lengths for a monovalent aqueous electrolyte are approximately 9.6, 3.1, 1.0, and 0.3 nm at bulk concentrations of 1, 10, 100, and 1000 mM, respectively. The dashed region illustrates the approximate spatial extent of electrostatic screening near the charged surface.

The EDL is fundamental because it controls ionic selectivity, local conductivity, and the degree to which the pore prefers one ionic species over another.

$$n_i = n_i^{\infty} \exp\left(-\frac{z_i e\phi}{k_B T}\right), \tag{2.12}$$

where $n_i^{\infty}$is the bulk number density of species i, $z_i$is its valence, $e$is the elementary charge, and $\phi$is the electric potential. This expression says that ions distribute according to the competition between electrostatic energy and thermal energy. Counterions are favored near a surface of opposite charge, while coions are exponentially suppressed.

The local charge density is then

$$\rho = e \sum_i n_i \, z_i. \tag{2.13}$$

This charge density generates an electric potential through Poisson's equation,

$$\nabla^2 \phi = -\frac{\rho}{\varepsilon_0 \varepsilon_r}, \tag{2.14}$$

where $\varepsilon_0$is the permittivity of free space and $\varepsilon_r$is the relative permittivity of the medium. Substituting the Boltzmann-distributed ionic concentrations into Poisson's equation yields the **Poisson-Boltzmann equation**,

$$\nabla^2 \phi = -\frac{e}{\varepsilon_0 \varepsilon_r} \sum_i n_i^{\infty} \, z_i \exp\left(-\frac{z_i e\phi}{k_B T}\right). \tag{2.15}$$

For a monovalent 1:1 electrolyte such as KCl, this simplifies to

$$\nabla^2 \phi = \frac{2en_{\infty}}{\varepsilon_0 \varepsilon_r} \sinh\left(\frac{e\phi}{k_B T}\right), \tag{2.16}$$

where n_{∞} is the bulk ion number density. This form makes clear that the EDL is a nonlinear electrostatic structure.

For sufficiently small potentials, the hyperbolic sine may be linearized using $\sinh x \approx x$, giving

$$\nabla^2 \phi = \kappa^2 \phi \tag{2.17}$$

with

$$\kappa^2 = \frac{2e^2 n_\infty}{\varepsilon_0 \varepsilon_r k_B T}. \tag{2.18}$$

The quantity κ^{-1} is the **Debye length**,

$$\lambda_D = \sqrt{\frac{\varepsilon_0 \varepsilon_r k_B T}{2e^2 n_\infty}}. \tag{2.19}$$

The Debye length gives the characteristic thickness of the EDL and represents the distance over which electric fields are screened in the electrolyte. For room-temperature aqueous KCl solutions, this length scale is often written in a convenient approximate form as

$$\lambda_D \approx \frac{0.3}{\sqrt{c_{\text{bulk}}}} \text{ nm} \tag{2.20}$$

with c_{bulk} in mol/L. This shows immediately that the EDL grows as the electrolyte concentration decreases. For example, the Debye length is on the order of 0.3 nm at 1 M, about 1 nm at 100 mM, about 3.1 nm at 10 mM, and about 9.5 nm at 1 mM. These are precisely the scales that make nanofluidic systems so sensitive to concentration.

This point is especially important for nanopores. In a microfluidic channel with dimensions far larger than λ_D, the EDL occupies only a thin layer near the walls and has limited effect on the bulk of the channel. In contrast, when the pore diameter becomes comparable to only a few Debye lengths, the double layers from opposite walls overlap. Once this happens, the entire cross section of the nanopore is influenced by the surface charge of the inner pore walls, and transport becomes strongly selective.

2.5 Permselectivity in Charged Nanopores

EDL overlap is the physical origin of **permselectivity** in many nanopores. A negatively charged nanopore favors cations because they serve as counterions; a positively charged nanopore favors anions for the same reason. In the overlapping-EDL regime, coions are strongly excluded from the pore volume, while counterions dominate transport. The channel therefore behaves as an ion-selective element rather than a neutral conduit.

This selectivity is not merely a surface effect in the intuitive sense; it is a volumetric effect arising from nanoconfinement. When the pore is sufficiently small or the electrolyte concentration sufficiently low, the entire pore can become enriched in counterions and depleted in coions. This alters both the conductivity inside the pore and the way the system responds to applied voltages. As a result, transport through nanopores is often asymmetric, nonlinear, and highly sensitive to solution conditions.

From a modeling perspective, permselectivity emerges naturally in continuum simulations when surface charge, diffusion, and electric-field-driven transport are correctly included. One of the strengths of a COMSOL-based treatment is that it allows this effect to be visualized spatially rather than described only qualitatively. By solving for concentration fields around and inside the nanopore, one can directly observe counterion enrichment, coion exclusion, and the dependence of selectivity on geometry and concentration.

2.6 Ionic Concentration Polarization

When a transmembrane potential is applied across a permselective nanopore, ionic selectivity leads to **ionic concentration polarization (ICP)**. In a permselective channel, the preferred ion species can pass through the nanopore much more readily than the rejected species.

Because of this imbalance, the reservoirs near the nanopore entrances do not remain at uniform concentration. Instead, one side of the pore develops a region of ion depletion while the other develops a region of ion enrichment.

To make this concrete, consider a nanopore with uniformly negative surface charge. Such a pore is selective for cations and rejects anions. If a transmembrane potential is applied such that cations are drawn through the pore from the top reservoir to the bottom reservoir, then cations are removed from the top side and deposited at the bottom side. Meanwhile, anions are unable to follow through the pore because they are excluded by the negative pore walls. The result is an ion depletion zone (IDZ) near the entrance from which cations are sourced and an **ion** enrichment zone (IEZ) near the exit where they accumulate. Reversing the polarity of the applied potential reverses the positions of the depletion and enrichment zones.

These depletion and enrichment zones are not confined strictly to the pore interior. One of the important findings visible in simulation is that ICP extends beyond the nanopore mouth into the surrounding reservoir space. This means that a nanopore modifies the ionic environment in a three-dimensional volume around it. Consequently, nearby nanopores may interact through overlapping concentration fields, and transport through one pore may influence transport through another. This observation becomes particularly important in later chapters where collective or interaction effects are discussed.

The strength and spatial extent of ICP depend on several parameters. Lower bulk concentration generally increases the thickness of the EDL and enhances surface-charge-driven effects, thereby strengthening ICP. Higher applied voltage increases electromigration and tends to expand depletion and enrichment regions. Surface charge density and nanopore geometry also

play central roles. Thus, ICP is not a fixed property but an emergent outcome of the coupled transport problem.

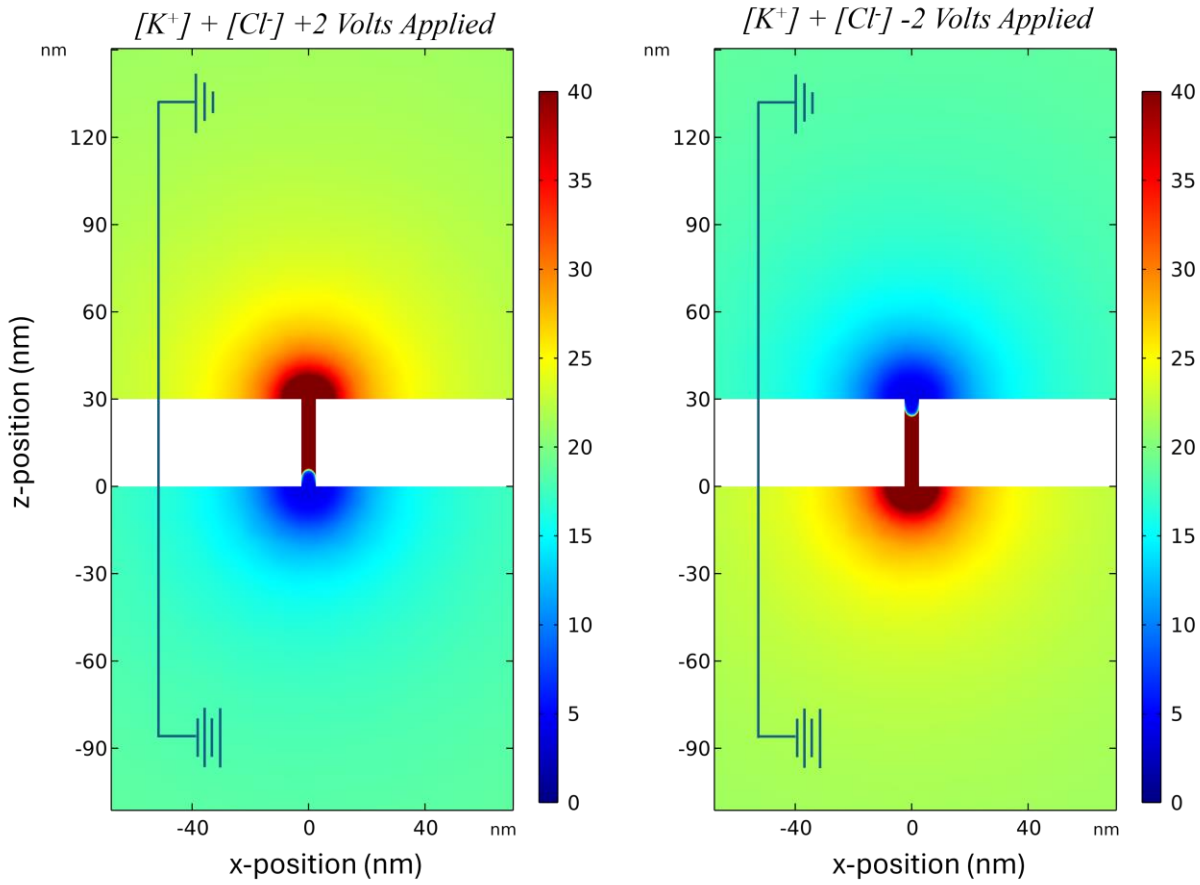

Figure 2.2 Ion Concentration Polarization Surrounding a Charged Nanopore. COMSOL Simulated spatial distribution of the total ionic concentration surrounding a negatively charged nanopore at transmembrane potentials of (+2) V (left) and (-2) V (right) with bulk concentration 10 mM. Under positive transmembrane bias, ion concentration polarization produces an ion-enrichment region on one side of the nanopore and a corresponding ion-depletion region on the opposite side. Reversal of the applied potential reverses the direction of ionic transport and consequently interchanges the locations of the enrichment and depletion regions. The spatially extended concentration gradients illustrate that ion concentration polarization is not confined to

the nanopore interior but extends into the adjacent reservoirs, providing a mechanism through which neighboring nanopores can interact when their polarization regions overlap.

2.7 COMSOL Interpretation of ICP and Selective Transport

A major advantage of the COMSOL framework is that it allows ICP to be analyzed not only conceptually but also quantitatively. Because the Transport of Diluted Species interface computes concentration fields throughout the domain, one can inspect the local concentration of each ionic species at any point in space. These simulations therefore provide direct access to the spatial extent of depletion and enrichment zones, the concentration contrast relative to bulk, and the way these features shift as applied bias, salt concentration, or surface charge are varied.

Within the COMSOL model, ICP emerges from the interplay between three ingredients: diffusion, electromigration, and electrostatic coupling. Diffusion acts to smooth concentration gradients, electromigration drives ions along or against the field depending on charge sign, and the charged nanopore surface imposes selective transport through the local potential environment. No separate ad hoc rule for depletion or enrichment is required; these regions arise naturally as the numerical solution of the transport equations. This is a key point to emphasize in the dissertation, because it demonstrates that the observed concentration maps are mechanistic predictions of the model, not merely schematic illustrations.

The electric potential used in the migration term may be imposed analytically or obtained by coupling to an electrostatics problem. COMSOL documentation notes that the potential distribution can be provided by coupling the Transport of Diluted Species interface to an electrostatics-type physics interface, and that this coupling is appropriate when migration in an electric field is important. This is the approach adopted in this work. The potential field obtained

from the electrostatic solution enters directly into the ionic flux expressions and therefore determines the electromigrative component of transport.

In systems with supporting electrolyte, the bulk potential field may often be approximated using an Ohmic current balance, where the electrolyte current density is proportional to the conductivity and electric field. COMSOL notes that for supporting electrolytes, electroneutral bulk transport can be represented through a conductivity-based relation of the form

$$\nabla \cdot (\kappa \nabla \phi) = 0. \tag{2.21}$$

Coupling this equation to the transport model provides a practical route for simulating ionic migration in dilute systems where the supporting electrolyte dominates the current transport.

2.8 Modeling Assumptions Used in This Dissertation

It is important to state clearly the assumptions that underlie the continuum simulations used throughout this dissertation.

First, the electrolyte is treated as a dilute solution. This is consistent with the use of the Transport of Diluted Species interface, which assumes that the transported ionic species are present at concentrations sufficiently low that the solvent properties can be approximated as constant.

Second, transport is modeled using diffusion and electromigration as the dominant mechanisms. Convection is neglected. This reflects both the nanoscale confinement of the systems under study and the desire to isolate the electrochemical transport mechanisms most relevant to ionic selectivity and concentration polarization. This assumption is also consistent

with the discussion in related nanopore theory where electroosmotic flow may be omitted in sufficiently confined geometries.

Third, the simulations are treated within a continuum framework. Individual ions are not modeled atomistically. Instead, concentrations are treated as continuous fields governed by coupled partial differential equations. This approximation is widely used in nanofluidics and is especially useful when the objective is to understand mesoscale concentration distributions, current-voltage behavior, and the influence of geometry and surface charge.

Fourth, the electric potential field is coupled into the transport equations through migration. This allows the simulations to capture field-driven ionic motion and the resulting concentration polarization. The inclusion of migration is essential; without it, the model would capture only diffusion and would fail to reproduce the voltage-dependent ion redistribution central to this dissertation.

Finally, the simulations are interpreted as a mechanistic tool for understanding trends, distributions, and relative changes rather than as an exact atomistic description of interfacial water structure or ion-ion correlations. The continuum model captures the dominant electrochemical transport physics relevant to the length scales and observables of interest.

2.9 Relevance to the Chapters That Follow

The theoretical and computational framework developed in this chapter underpins the remainder of the dissertation. Later chapters examine how nanopore geometry, surface charge, and applied transmembrane potential shape ionic transport behavior. The current responses, concentration maps, and nanopore interaction effects presented there are all rooted in the coupled transport processes introduced here.

In particular, the concept of EDL overlap explains why nanopores become selective at low enough concentrations or small enough diameters. The concept of permselectivity explains why counterion transport dominates in charged channels. The concept of ICP explains why applied potentials generate depletion and enrichment zones near pore openings. Finally, the COMSOL finite element framework provides the means by which these effects are computed in realistic geometries and compared across parameter sweeps.

Taken together, these ideas establish the physical and computational basis for the work that follows. The nanopore is not simply a passive opening connecting two electrolyte reservoirs. Rather, it is an electrochemically active nanoscale transport element whose behavior is governed by confinement, surface charge, and the coupled transport of ions in electric fields.

CHAPTER 3 Nanopore Fabrication, Functionalization, and Characterization

As previously discussed in Chapter 1, biological nanopores exhibit unparalleled selectivity in ionic transport. For example, potassium-selective channels can demonstrate selectivity ratios on the order of 10^4 for potassium over sodium, while aquaporin channels facilitate the rapid transport of water molecules at near-diffusive limits, all while effectively excluding nearly all other species, including protons.[9,22,23] Despite these remarkable capabilities, biological nanopores are subject to several important limitations. First, their functionality depends on tightly controlled physiological conditions; even slight deviations in salinity, pH, or temperature from their native environment can lead to protein denaturation and a subsequent loss of structural integrity and transport performance.[24] Second, biological nanopores are typically embedded within lipid bilayers, which are inherently fragile and difficult to integrate into engineered or technological systems due to their susceptibility to mechanical and chemical degradation.[24]

These limitations significantly restrict the applicability of biological nanopores in engineered systems, motivating the development of synthetic platforms that offer greater mechanical stability, environmental robustness, and tunable functionality.[25,26] This increased resilience enables the investigation of ionic transport across a much broader range of environmental conditions than is possible with biological systems.[25] Moreover, the tunability and durability of synthetic nanopores position them as promising candidates for integration into advanced nanofluidic devices, with potential applications extending to areas such as neuromorphic computing, protein sequencing, osmotic power generation, and molecular separation.[25,27–30]

3.1 Overview of Nanopore Fabrication Platforms

Early approaches to synthetic nanopore fabrication have evolved into a diverse set of techniques spanning multiple materials and fabrication paradigms, broadly categorized as top-down and bottom-up approaches.[31,32] A comprehensive overview of these methods highlights both their capabilities and limitations in the context of controlled nanofluidic device fabrication.[32,33]

One of the earliest and most widely used techniques is track-etching in polymer membranes, such as polyethylene terephthalate (PET) or polycarbonate.[34] In this approach, high-energy heavy ions such as gold (Au), xenon (Xe), or uranium (U), are accelerated to kinetic energies in the MeV to GeV range and used to generate latent damage tracks within the polymer matrix. These tracks are subsequently developed into nanopores through chemical etching, typically using strong alkaline solutions such as sodium hydroxide (NaOH). The etchant preferentially dissolves the damaged regions due to their increased chemical susceptibility, forming conical or cylindrical nanopores that span the membrane.[35] While this method is relatively inexpensive and experimentally accessible, it provides limited control over nanopore placement and inter-pore spacing, particularly when multiple pores are generated, making it less suitable for applications requiring deterministic spatial control.[34,36]

Another widely utilized fabrication method is anodic oxidation of aluminum, which produces highly ordered nanopore arrays in anodic aluminum oxide (AAO).[37,38] Under carefully controlled electrochemical conditions, self-organized pore structures can form with high densities and tunable diameters ranging from a few nanometers to hundreds of nanometers.[38] Although this method is advantageous for creating large-area, uniform nanopore arrays, it lacks

the flexibility required for single-pore fabrication and precise positioning, limiting its applicability in studies focused on individual or interacting nanopores.[36,38]

In silicon-based systems, dielectric breakdown has emerged as a simple and accessible technique for nanopore fabrication.[33,39] By applying a sufficiently large electric field across a thin dielectric membrane, such as silicon nitride, defects accumulate until a conductive path forms, resulting in nanopore creation. While this approach enables sub-nanometer pore formation without the need for advanced instrumentation, it inherently produces stochastic pore locations and limited control over pore geometry, posing challenges for reproducibility and array fabrication.[33,39,40]

More controlled fabrication methods rely on focused ion beam (FIB) and transmission electron microscopy (TEM) milling, where highly focused ion or electron beams are used to directly sculpt nanopores in thin membranes.[15,16,33,36] These techniques allow for sub-nanometer precision in both pore size and placement, as well as post-fabrication tuning through beam-induced material modification. As a result, electron microscopy based fabrication methods have become the standard for applications requiring deterministic control over nanopore geometry, particularly in studies involving nanopore arrays and inter-pore interactions.[15,16,33,36] These techniques are central to the experimental work presented in this dissertation and will be discussed in detail later in this chapter and in Chapter 4.

In addition to these top-down approaches, alternative platforms such as glass nanopipettes, tunable elastomeric nanopores, and two-dimensional (2D) material nanopores have also been developed.[36] Glass nanopipettes are fabricated by thermal pulling of glass capillaries, enabling nanoscale openings without lithographic techniques.[36,41] Tunable nanopores utilize deformable polymer membranes to dynamically adjust pore size through mechanical strain.

Meanwhile, nanopores in atomically thin materials such as graphene or MoS_2 offer unprecedented spatial resolution due to their minimal thickness, making them promising candidates for single-molecule sensing applications.[36,42,43]

Finally, bottom-up approaches such as DNA origami nanopores provide atomically precise control over pore geometry and surface chemistry through molecular self-assembly. While these systems offer unmatched precision, their integration into larger device architectures remains challenging due to their limited structural scale and mechanical stability.

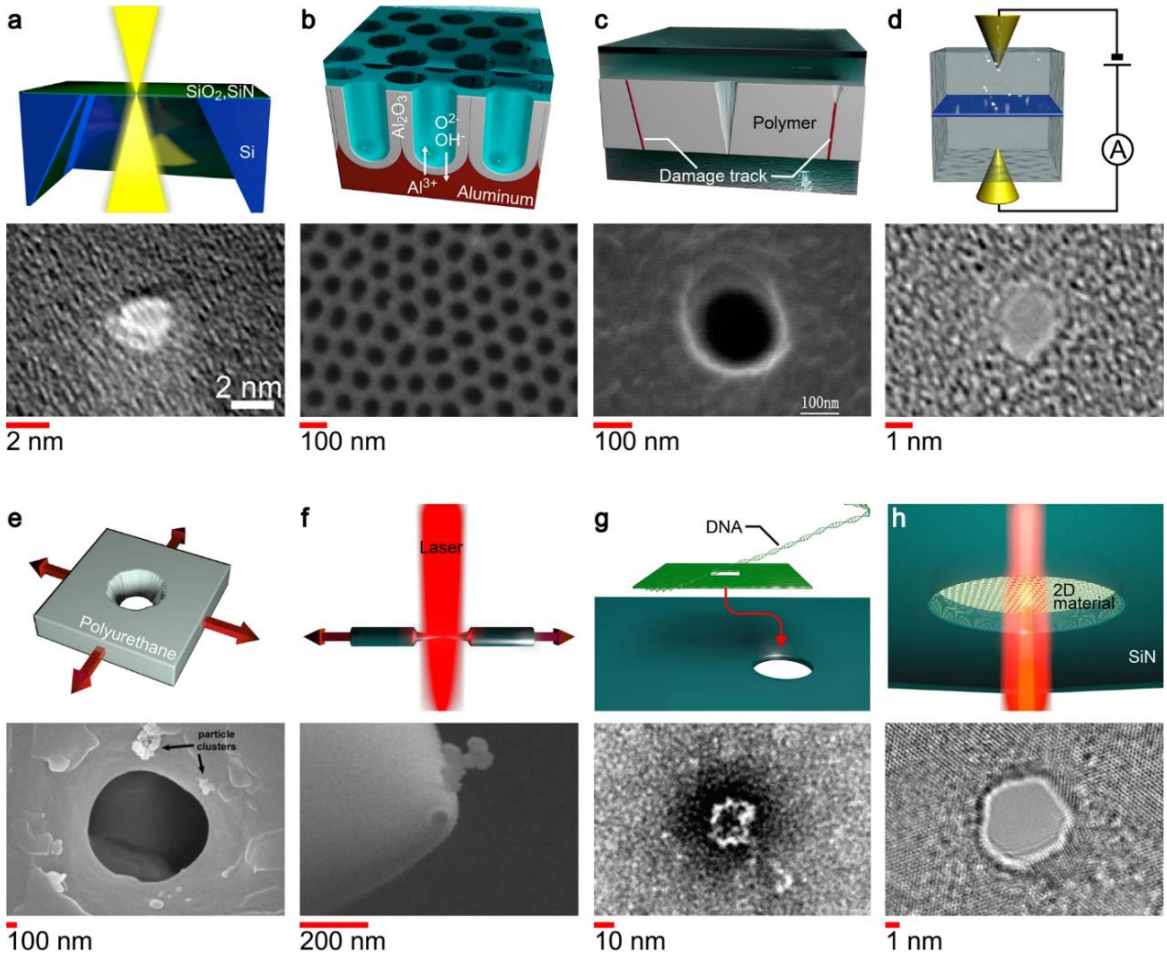

Figure 3.1 Overview of Nanopore Fabrication Techniques. (a) focused ion or electron beam milling for deterministic nanopore formation in solid-state membranes; (b) anodic aluminum

oxide fabrication producing highly ordered nanopore arrays via electrochemical self-organization; (c) track-etching, where high-energy ion irradiation followed by chemical etching forms nanopores along latent damage tracks; (d) dielectric breakdown, in which a strong electric field induces pore formation in thin dielectric membranes; (e) tunable nanopores utilizing mechanically deformable materials to dynamically control pore size; (f) glass nanopipettes fabricated through thermal pulling of capillaries; (g) DNA origami nanopores assembled via molecular self-organization with near-atomic precision; and (h) nanopores in two-dimensional materials, such as graphene, enabling ultrathin membrane transport. Representative scanning electron micrographs illustrate the diversity of nanopore geometries and material platforms from. Reproduced from[36].

Despite the wide range of available fabrication techniques, a central challenge across all platforms is achieving simultaneous control over nanopore size, geometry, and spatial positioning while maintaining the mechanical and chemical robustness required for scalable, industry-relevant applications. This level of geometric precision is particularly essential for studies involving coupled transport phenomena, such as interactions between neighboring nanopores. Consequently, the work presented in this dissertation employs TEM based fabrication nanopore systems embedded in silicon nitride membranes, which enables nanometer-scale precision in both nanopore diameter and placement, providing a robust and versatile platform for investigating ionic transport in both single-pore and multi-pore systems.

3.2 Silicon Nitride Membrane Fabrication

The nanopore devices used throughout this work are fabricated on commercially available silicon nitride (SiN_x) membrane chips obtained from Norcada. Although the exact

fabrication protocols used by commercial vendors are proprietary, these devices are produced using well-established wafer-scale microfabrication techniques that are widely reported in the literature and follow standard semiconductor processing workflows.[16,44]

The fabrication process typically begins with a double-side polished silicon wafer, commonly oriented along the ⟨100⟩ crystallographic direction to enable anisotropic wet etching. A low-stress silicon nitride thin film is deposited on both sides of the wafer using low-pressure chemical vapor deposition (LPCVD), a critical step that ensures mechanical stability of the final suspended membrane. Film thicknesses for nanopore applications are generally in the range of 20–50 nm, with thinner membranes preferred for enhancing spatial resolution during nanopore fabrication and measurement.

Following deposition, photolithographic patterning is used to define membrane windows on one side of the wafer. Reactive ion etching (RIE) is then employed to selectively remove the exposed silicon nitride, creating openings that expose the underlying silicon substrate. These patterned regions determine the lateral dimensions of the final membrane.[16,44]

Subsequently, anisotropic wet etching of silicon is performed, most commonly using potassium hydroxide (KOH). Due to the crystallographic dependence of silicon etching, KOH preferentially removes material along the ⟨100⟩ direction while leaving the slower-etching ⟨111⟩ planes intact, resulting in the formation of pyramidal cavities beneath the patterned windows. As etching progresses, silicon is removed until only the thin silicon nitride layer remains, forming a free-standing membrane. The final membrane thickness is dictated by the initial LPCVD deposition, while the lateral dimensions are defined by the photolithographic mask.

Following membrane fabrication, the wafer is diced into individual chips, typically on the order of a few millimeters in size, each containing a central freestanding SiN_x membrane window

(~50 × 50 μm²) supported by a silicon frame. This wafer-scale fabrication process enables the reproducible production of mechanically robust yet ultrathin membranes that provide a stable platform for subsequent nanopore formation. In this work, nanopores are introduced into these suspended SiN_x membranes using controlled electron-beam sculpting in a transmission electron microscope, as described in the following section.Building on this platform, nanopores are then introduced through high-resolution fabrication techniques. In this work, nanopore formation is achieved via controlled electron beam sculpting using a transmission electron microscope.

3.3 Nanopore Formation via Transmission Electron Microscopy

At the nanoscale, the ability to precisely remove individual atoms enables direct control over material structure. In this work, nanopores are fabricated using a TEM, operated at accelerating voltages on the order of 200 keV, where the incident electron beam transfers sufficient energy to displace atoms from the silicon nitride lattice. The electron beam is focused to a high-intensity point and positioned with nanometer precision on the membrane surface, enabling deterministic placement of nanopores.

The nanopore formation process is governed primarily by electron beam induced sputtering, in which incident electrons transfer energy to lattice atoms, resulting in their displacement and removal. As this process continues, a continuous void is formed through the membrane, producing a nanopore. Typical drilling times are on the order of several minutes, depending on beam conditions and membrane thickness.

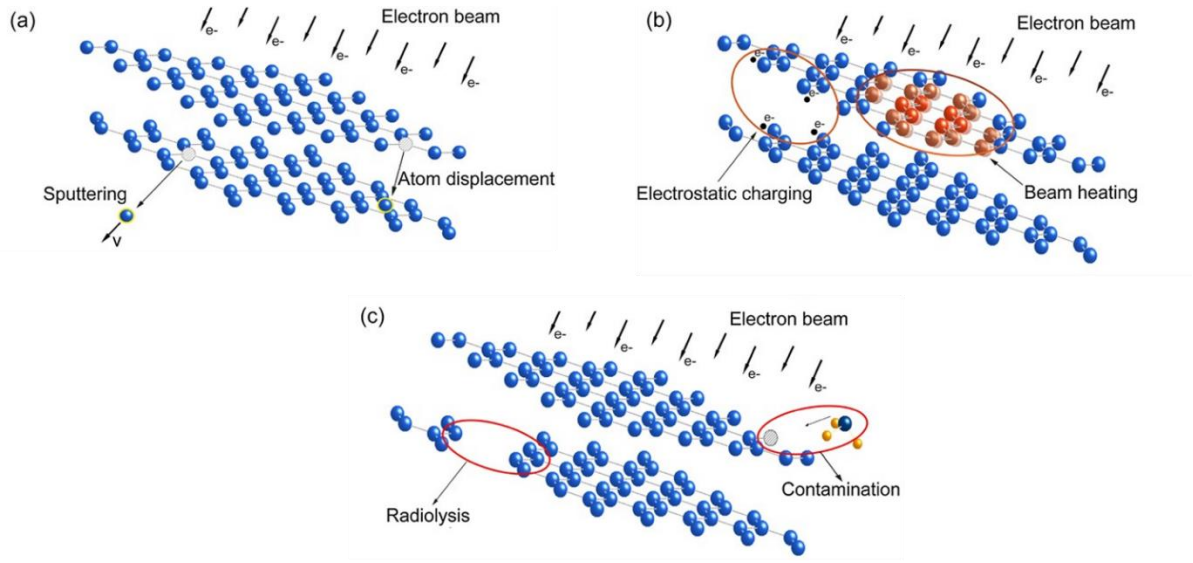

Figure 3.2 Schematic Overview of Electron-Beam–Induced Damage Mechanisms. Adapted from Walker et al.[45] © 2016 Wiley-VCH GmbH. (a) momentum-transfer processes leading to sputtering and lattice atom displacement; (b) charge accumulation and localized thermal effects due to beam interaction; and (c) radiolytic bond breaking and contamination buildup under prolonged irradiation.

A key advantage of TEM-based fabrication is the ability to dynamically tune nanopore size through post-drilling beam modulation. High-intensity focused beams promote continued material removal and pore enlargement, while lower-intensity or defocused beams induce thermally activated surface diffusion. This results in surface reflow driven by minimization of surface energy, enabling nanopore shrinkage.

This shrinkage mechanism is effective only below a critical diameter, typically on the order of 10 nm, beyond which sputtering dominates over diffusion. As a result, precise control over nanopore diameter can be achieved through iterative cycles of drilling and beam-induced reshaping.

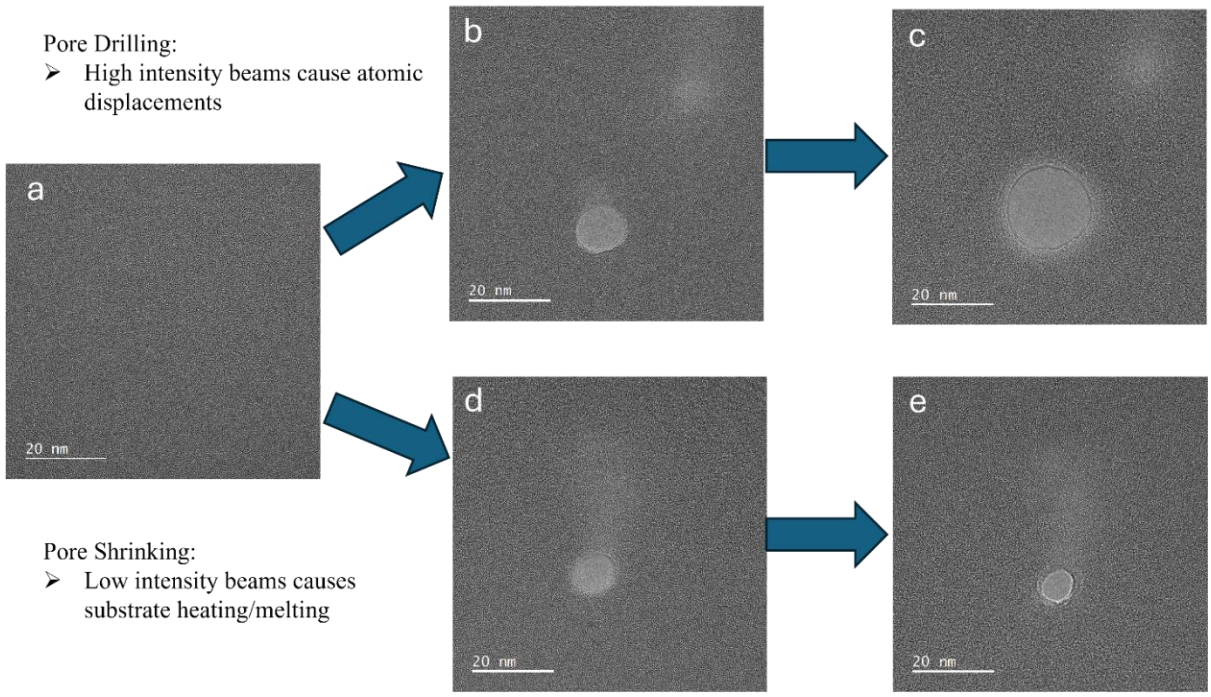

Figure 3.3 Nanopore Refinement via Electron Beam Control. The diameter of a nanopore can be precisely tuned by adjusting the intensity of the incident electron beam. This schematic illustrates the drilling of an individual nanopore, followed by controlled expansion or contraction of the pore size through beam-induced material removal or restructuring.

Nanopores fabricated via TEM do not exhibit ideal cylindrical geometries, but instead adopt an hourglass-shaped profile characterized by a narrow constriction near the center of the membrane and wider openings at the surfaces. This geometry arises from the spatial distribution of electron beam intensity as well as scattering effects within the membrane.

The resulting structure can be approximated as a double-conical geometry, where the effective cone angle depends on the membrane thickness and beam parameters. This non-uniform geometry has significant implications for ionic transport, as it leads to electric field focusing within the constriction region and modifies ion distributions relative to idealized cylindrical models. This effect will be discussed in detail when considering its effect on ionic

conductance in chapter 4 as such geometric effects are particularly important in nanoconfined systems, where even small deviations from ideal geometry can strongly influence ionic selectivity, conductance, and nonlinear transport behavior.

One of the primary advantages of TEM-based fabrication is the ability to precisely control nanopore placement, enabling the creation of multi-pore systems with well-defined geometries. By adjusting the position of the electron beam, nanopores can be fabricated with nanometer-scale accuracy, allowing for systematic variation of inter-pore spacing.

This capability is critical for investigating interactions between nanopores, particularly in regimes where electrostatic effects extend beyond individual pore boundaries. When nanopores are sufficiently close, electric double layers and ionic concentration polarization regions may overlap, leading to coupled transport behavior. These interactions give rise to collective phenomena such as depletion zone coupling, field amplification, and nonlinear ionic conductance, which are explored in later chapters. The ability to fabricate controlled nanopore arrays therefore provides a powerful platform for studying many-body effects in nanofluidic systems.

3.4 Surface Charge and Chemical Modification

Following fabrication, nanopore devices are immersed in aqueous electrolyte solutions, typically potassium chloride (KCl) at near-neutral pH. Under these conditions, the silicon nitride surface undergoes deprotonation, resulting in a negatively charged surface. The surface charge density is typically on the order of −0.01 to −0.05 C/m², depending on environmental conditions such as pH and ionic strength. This intrinsic surface charge establishes the baseline electrostatic

environment within the nanopore and induces the formation of an electric double layer at the solid–liquid interface, which governs ionic transport behavior.

At sufficiently low electrolyte concentrations, the Debye length increases and can become comparable to the nanopore dimensions. In this regime, overlapping electric double layers extend across the pore volume, leading to enhanced ion selectivity and significant deviations from bulk transport behavior. As a result, surface charge becomes the dominant factor controlling ionic transport, providing a natural entry point for tuning nanopore functionality through surface modification.

To further control the interfacial properties of the nanopore, a variety of post-fabrication surface modification techniques may be employed. These include silane-based functionalization, polymer coatings, biomolecular attachment, and thin-film deposition. Such approaches enable direct tuning of surface charge, wettability, and chemical interactions without altering the underlying nanopore geometry. In addition to modifying electrostatic properties, surface coatings are often used to suppress non-specific interactions between the nanopore walls and analytes, including electrostatic attraction, van der Waals forces, and hydrophobic effects, which can otherwise lead to pore clogging or unstable transport behavior.

More advanced fabrication strategies involve introducing spatially non-uniform surface modifications to create asymmetric nanopore structures.[46] This can be achieved through selective functionalization of specific regions of the pore or through sequential chemical processing steps. These approaches generate controlled variations in surface charge along the pore axis, effectively transforming the nanopore into a functional nanofluidic element. In such systems, the resulting asymmetry can produce direction-dependent ionic transport, giving rise to diode-like behavior where the measured current depends on the polarity of the applied bias.

Beyond chemical functionalization, additional fabrication pathways include the integration of metallic structures. Thin metal films, such as gold, may be deposited and patterned to create metal–dielectric interfaces in proximity to the nanopore. These configurations enable electrostatic coupling between the conductive layer and the ionic solution within the pore, allowing for either passive polarization effects or active control of transport behavior when externally biased. Such hybrid approaches extend nanopore functionality toward dynamically tunable nanofluidic systems.

In the present work, surface modification is achieved through silane-based functionalization using aminopropyltrimethoxysilane (APTMS).[2] Due to the presence of surface hydroxyl groups on silicon nitride, APTMS readily forms covalent bonds with the membrane surface, introducing amine functional groups within the nanopore. Under aqueous conditions, these amine groups can become protonated, thereby modifying the native negative surface charge and enabling controlled tuning of the electrostatic environment within the pore. This approach provides a robust method of developing heterogenous surface charge densities along the pore wall, a method that is reproducible and discussed later I chapter 4 for its effects on ionic transport.

3.5 Gold Integration and Electrostatic Gating

Chapter 6 explores the behavior of nanopores fabricated in close proximity to a junction between gold (Au) and silicon nitride (SiN_x). To realize these structures, hybrid devices are fabricated through a multi-step process that integrates thin-film deposition, microfabrication, and electron microscopy–based nanopore drilling.

First, a thin metallic layer of gold, with a thickness of approximately 10 nm, is deposited onto the silicon nitride membrane using chemical vapor deposition. Following deposition, a localized region of the gold film is selectively removed using SEM, creating a defined window (approximately 10 × 10 μm²) within the larger 50 × 50 μm² membrane area. This process exposes the underlying ~30 nm thick SiN_x layer while preserving a well-defined Au/SiN_x interface.

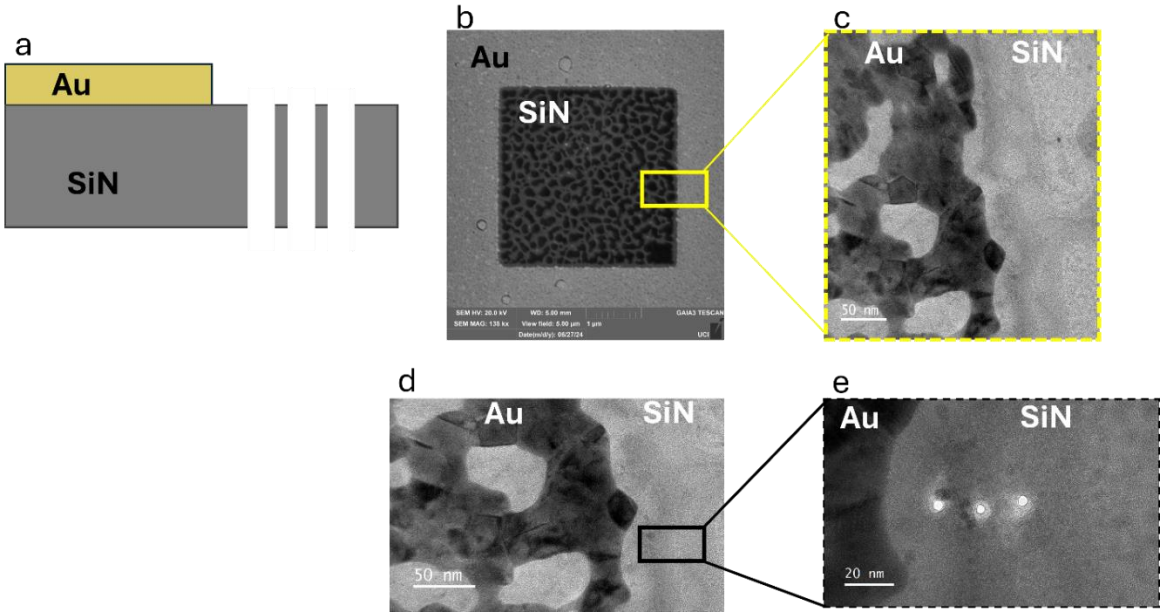

Figure 3.4 Fabrication Pathway for Nanopore Arrays at a Au/SiN_x Interface. (a) Schematic illustrating the target device geometry, showing a two-dimensional representation of a nanopore array positioned in close proximity to the gold–silicon nitride interface. (b) SEM image following removal of the gold layer, exposing the underlying SiN_x membrane. (c) TEM image of the Au/SiN_x interface, highlighting the junction between the gold film and silicon nitride layer. (d) High-magnification TEM image of the membrane region prior to nanopore drilling. (e) TEM image of a nanopore array fabricated near the Au/SiN_x interface, with the closest pore located within 20 nm of the gold layer.

The sample is then transferred to a transmission electron microscope (TEM), where the interface between the gold and silicon nitride regions is identified with nanometer-scale precision. Nanopore arrays are subsequently fabricated within the exposed SiN_x region using controlled electron beam sculpting, with pore placement carefully positioned relative to the Au/SiN_x boundary. This approach enables systematic control over the distance between the nanopores and the metallic interface, which is critical for investigating interfacial effects in later chapters.

If electrical access to the metallic layer is desired, additional fabrication steps can be implemented. These include further thin-film deposition and electron beam lithography to define conductive pathways, as well as the incorporation of insulating layers to isolate the gold from the surrounding electrolyte. Such modifications enable the gold layer to be electrically addressed, allowing for controlled manipulation of the local electrostatic environment.

While the primary focus of this section is on fabrication, it is worth noting that nanopores positioned near a metallic interface exhibit enhanced electrostatic coupling. As discussed in later chapters, this configuration enables modulation of ionic transport through both externally applied bias and induced polarization effects, providing a pathway toward actively tunable nanofluidic devices.

3.6 Experimental/Electrochemical Characterization of Nanopore Arrays

Once nanopore devices are fabricated, their transport properties are probed through electrochemical measurements designed to capture ionic dynamics under nanoconfinement. Because this work is motivated by bio-inspired transport phenomena, the system is studied in an aqueous environment, with water serving as the solvent due to its relevance in both biological

systems and nanofluidic experiments. Electrolyte solutions are prepared using potassium chloride (KCl), a commonly employed salt that provides a well-characterized and relatively simple ionic system.

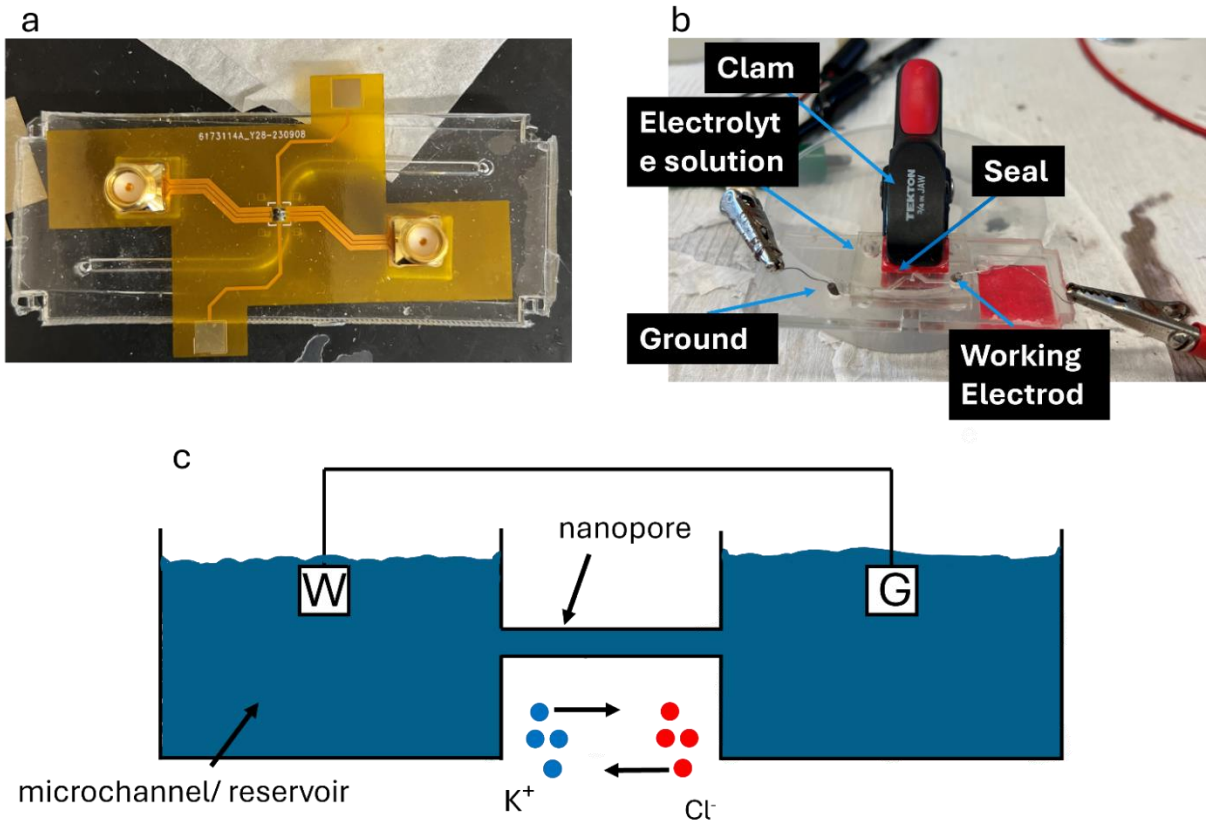

Figure 3.5 Device Characterization for Nanopore Array Systems. The schematic shows the basic layout for contacting the device and in general the setup for conductivity cells so that we can measure the current through the nanochannel.

KCl is particularly advantageous because it introduces minimal complexity into the electrostatic description of the system. In addition, the mobilities of the constituent ions, K^+ and Cl^-, are nearly identical in aqueous solution ($\mu_{k^+} \approx 7.6 \times 10^{-8}$ m²/V·s and $\mu Cl^- \approx 7.9 \times 10^{-8}$ m²/V·s). As a result, any observed asymmetry in ionic transport can be attributed primarily to the nanopore geometry, surface properties, or applied boundary conditions, rather than differences in

ion mobility. This simplifies interpretation and allows for more direct analysis of nanopore-driven effects.

Ionic transport is measured by placing the nanopore device between two fluid reservoirs, each containing electrolyte solution. In this work, the devices are integrated into a measurement platform consisting of polydimethylsiloxane (PDMS) microchannels that interface with both sides of the nanopore membrane. These channels have characteristic dimensions on the order of millimeters, which are significantly larger than the nanoscale dimensions of the pore. The device is mechanically clamped to form a sealed system, ensuring that ionic transport between the reservoirs occurs exclusively through the nanopore.

Due to the large disparity in length scales, the nanopore represents the dominant resistive element in the system. For example, a nanopore with dimensions on the order of tens of nanometers in length and diameter exhibits a resistance on the order of megaohms, whereas the surrounding microchannels contribute a comparatively negligible resistance. This ensures that the measured signal is highly sensitive to transport through the nanopore itself.

To probe ionic current, Ag/AgCl electrodes are inserted into each reservoir. These electrodes facilitate reversible redox reactions involving chloride ions, enabling the conversion of ionic current in solution into an electronic current in the external circuit. As ions migrate through the nanopore under an applied electric field, charge imbalances begin to develop in the reservoirs. These imbalances are continuously neutralized by electrochemical reactions at the electrode surfaces, allowing steady-state current to be maintained. The resulting electron flow through the external circuit is directly proportional to the ionic current through the nanopore.

By applying a voltage bias across the device and measuring the resulting current, current–voltage (I–V) characteristics can be obtained. These measurements provide a direct means of

characterizing nanopore behavior, including conductance, selectivity, and nonlinear transport phenomena. Although conceptually simple, I–V curves contain rich information about the underlying transport mechanisms and serve as a primary tool for analyzing nanopore systems, as discussed in detail in Chapter 4.

CHAPTER 4 Ion Concentration Polarization and Interpore Interactions in Nanopore Arrays

Single nanopores have become important platforms for biological sensing,[47–49] deoxyribonucleic acid (DNA) and protein sequencing,[50–56] the development of biomimetic channels,[57–61] and fundamental studies of nanoscale transport.[62,63] These studies have demonstrated that controlling ionic transport through nanopores requires consideration not only of pore geometry, particularly pore diameter, but also of the physicochemical properties of the pore walls. Tailoring the electrochemical properties of nanopore surfaces has enabled the development of ionic diodes,[63–65] hydrophobic valves for controlling the transport of water and dissolved species,[66–69] as well as systems capable of ion-selective transport and osmotic power generation.[70,71]

Much of the motivation for studying nanopore transport originates from biological systems, where physiological processes generally depend not on the function of a single ion channel, but rather on the coordinated behavior of many channels embedded within the same membrane.[72] In an axon, for example, channels with different functionalities respond to external stimuli and operate collectively to enable the propagation of electrochemical signals in both space and time. [72] Extending the single-nanopore platform toward arrays of interacting nanopores is therefore a natural step toward constructing biomimetic ionic circuits.

The transition from isolated nanopores to interacting nanopore arrays introduces several fundamental questions. Which physical mechanisms govern interactions between neighboring nanopores? How closely must nanopores be positioned before their transport properties become coupled? How do the electrochemical properties of the pore walls influence both interpore interactions and the overall transport characteristics of an array?

Several types of nanopore arrays have previously been investigated. For example, nanopore arrays have been employed for DNA sensing and sequencing.[73,74] In these applications, the distance between neighboring nanopores is typically hundreds of times larger than the pore diameter, allowing each nanopore to function essentially independently.[73,74]

Nanopore arrays have also been used in fundamental studies of nanoscale diffusion. In one such system, arrays were fabricated in 50 nm thick silicon nitride membranes and contained pores approximately 90 nm in diameter.[75] Transport through these low-aspect-ratio nanopores was limited by diffusion toward the pore openings, which could be treated as sinks. [75] When neighboring nanopores were sufficiently separated, the radial diffusion profiles associated with individual pores were preserved and each nanopore behaved independently. As the pores were positioned more closely, however, the diffusion profiles of neighboring nanopores overlapped and transport through the individual pores could no longer be considered independently. Interestingly, some overlap of the diffusion profiles remained even when the ratio of interpore distance to pore radius approached 20.[75]

Arrays have also been investigated to determine how electric-field-driven ion transport depends on nanopore number and spatial arrangement.[76] In these systems, the constituent nanopores were approximately 200 nm in diameter and 50 nm in length.[76] Ionic transport through the arrays increased sub-linearly with the number of nanopores because of overlapping access-resistance regions at the nanopore entrances.[76,77] As the nanopores became more densely packed and the number of pores increased, the total ionic conductance of the array became smaller than the value predicted by simply summing the conductances of the individual nanopores.[78]

Similar behavior has been reported for arrays of approximately 10 nm diameter charged nanopores fabricated in a 12 nm thick layer of hexagonal boron nitride.[79] Under an applied salt concentration gradient, the magnitude of the osmotic current decreased by approximately a factor of 10 when the interpore distance within a 3 × 3 array was reduced from 1000 to 200 nm.[79] This behavior was attributed to ion concentration polarization, which produces a region of depleted ionic concentration on one side of the membrane and a region of enhanced ionic concentration on the opposite side.[78,80–82]

ICP occurs when a voltage is applied across a membrane that is at least partially selective toward one ionic species.[78,80–82] In densely packed nanopore arrays, the depletion zones associated with neighboring nanopores can overlap, forming a larger depletion region that extends across the membrane surface and limits the overall conductance of the array.[78,79] Porous nanofiltration membranes provide another example of systems that can be considered nanopore arrays.[83–85] These membranes typically possess high porosity, and their performance can likewise be strongly affected by concentration polarization.[78] Unlike nanopore arrays fabricated with well-defined geometries, however, polymer membranes often contain interconnected nanovoids rather than discrete nanopores of precisely controlled dimensions.[84,86]

Beyond understanding interpore interactions, an important consideration is how the transport properties of nanopore arrays can be controlled. Ionic transport can first be tuned through the number and spatial arrangement of the constituent nanopores.[76] In addition, when the pore radius becomes comparable to the thickness of the electrical double layer, ionic transport through both individual nanopores and nanopore arrays becomes strongly dependent on the surface charge density of the pore walls, σ_p.[62,87,88]

The extent to which σ_p determines transport properties, including ion selectivity, also depends on the pore aspect ratio, defined as the ratio of pore length to pore radius. For nanopores with aspect ratios close to unity, transport is influenced by both the pore-wall surface charge and the regions of altered ionic concentration produced by ICP.[89,90] The influence of σ_p increases with increasing pore length and interpore distance, providing an additional mechanism for controlling transport through individual nanopores and nanopore arrays.[89,90]

For nanopores and nanopore arrays with aspect ratios below unity, transport is instead governed primarily by the properties of the external membrane surface rather than by the pore walls. This occurs because the resistance of low-aspect-ratio pores is dominated by the regions near the pore entrances and by ICP rather than by the internal pore geometry.[90–92] Consequently, both pore-wall surface charge and the properties of the external membrane surface must be considered when designing nanopore arrays and porous membranes for applications such as osmotic power generation.[90]

The work presented in this chapter investigates minimal nanopore arrays as model systems for identifying the roles of ICP and pore-wall properties in controlling interpore interactions and the overall transport properties of nanopore arrays. The central hypothesis is that ICP can serve as a mechanism through which neighboring nanopores interact. At the same time, the electrochemical properties of the pore walls determine important transport characteristics of the array, including ion selectivity and ion current rectification, as previously demonstrated for individual nanopores.[63,93] Because ICP itself depends on the electrochemical properties of the nanopore walls, modification of these surfaces provides a potential means of controlling the extent of interpore coupling.

To enhance the contribution of the pore walls to the transport properties of the arrays, nanopores with opening diameters below 10 nm and aspect ratios of at least 6 were investigated.[89,91] Individual nanopores were fabricated sequentially in 30 nm thick silicon nitride membranes using transmission electron microscopy.[16] The center-to-center distance between neighboring nanopores was varied from 15 to 200 nm.

The silicon nitride nanopore walls were negatively charged because of the presence of surface silanol groups.[94] The influence of these surface charges on the ionic conductance of the arrays was examined by varying the electrolyte concentration between 10 mM and 1 M KCl. Closely packed nanopores exhibited lower conductance than arrays with larger interpore distances. The effects of pore-wall surface charge became increasingly important at lower electrolyte concentrations, where larger depletion regions formed and stronger suppression of ionic conductance was observed.

The ability of pore-wall surface chemistry to tune array transport was further examined by introducing a surface-charge pattern that causes the constituent nanopores to function as ionic diodes.[63] This modification suppressed the formation of strongly depleted regions and reduced the effect of ICP on device conductance. Continuum modeling further confirmed that the diode behavior originated from the charge pattern along the nanopore walls and could occur even in the absence of charge on the external membrane surface.[60]

The nanopore arrays investigated here consist of two and three nanopores with equivalent surface characteristics and transport properties. These minimal arrays provide a foundation for the eventual development of heterogeneous nanopore arrays in which individual pores possess distinct functionalities and interact to form more complex ionic circuits.

4.1 Fabrication and Characterization of Nanopore Arrays

Arrays containing two and three nanopores were fabricated by electron-beam drilling using a transmission electron microscope.[16] In total, 10 two-nanopore arrays and 9 three-nanopore arrays were analyzed. Each array was characterized using two parameters: the average nanopore radius, R, determined from TEM images of all constituent nanopores, and the average center-to-center interpore spacing, S.

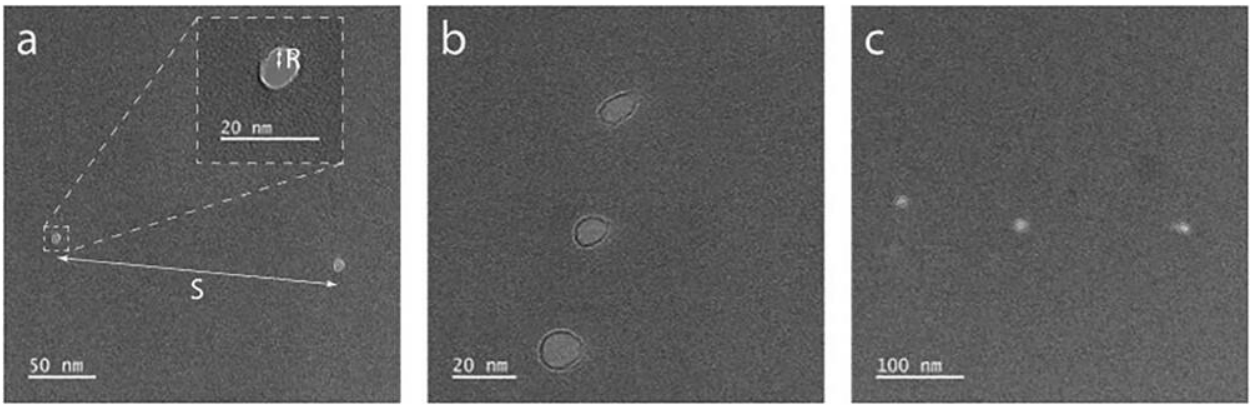

Figure 4.1 Fabrication of Nanopore Arrays via TEM. High resolution TEM micrographs of nanopore arrays. a) Image of an array containing two nanopores. The average pore radius R and average center-to-center pore spacing S is measured in the images. b,c) Images of arrays containing three pores that are in close proximity (b) and far away from each other (c).

Because the fabricated arrays contained nanopores with slightly different average opening diameters, a normalized interpore distance, S/R, was used to facilitate comparison among different devices. Similar normalized-distance parameters have previously been employed for electrode arrays.[75,95,96]

Transport through all two- and three-nanopore arrays was examined by recording current–voltage characteristics over a broad range of KCl concentrations at pH 8, where the silanol groups on the silicon nitride surfaces are deprotonated. Experimental conductance was

determined from the approximately linear region of each current–voltage curve between −1 and +1 V.

4.2 Nature of Interpore Interactions

A central question in understanding nanopore arrays is how nanopores embedded within the same membrane interact and how surface charge facilitates this interaction. In general, neighboring nanopores can interact through competition for ionic access in the regions surrounding their entrances.[78]

The arrays considered here contain nanopores with negatively charged walls and opening diameters below 10 nm. Because the membrane thickness is 30 nm, the geometrical resistance of each nanopore is substantially larger than the access resistance predicted by Hall's expression.[77] Nevertheless, because these pores have nanometer-scale dimensions, their total resistance is also influenced by ICP, which creates regions of altered ionic concentration at the pore entrances.[78,80–82]

ICP produces an ion enrichment zone (IEZ) on one side of a selective membrane and an ion depletion zone (IDZ) on the opposite side.[78,80–82] Of particular importance to transport is the depletion zone, which modulates ionic current in both a concentration- and voltage-dependent manner. As electrolyte concentration decreases and applied voltage increases, the depletion region associated with an individual nanopore becomes wider and contains progressively fewer ions.[88] Consequently, both the degree of overlap between depletion zones and the resulting interdependence of neighboring nanopores are expected to depend strongly on the operating conditions.

To determine the spatial extent of these depletion zones and examine ionic concentration distributions in arrays with different interpore distances, three-dimensional finite-element models of the arrays were developed in COMSOL Multiphysics. Ionic transport was described using the coupled Poisson–Nernst–Planck equations.[88] The pore lengths, diameters, and interpore spacings were selected to reproduce the experimentally fabricated systems. For computational simplicity, the modeled nanopores were assumed to be cylindrical. Because of the large dimensions of the three-dimensional computational domain, surface charges on the external membrane surfaces were not included.

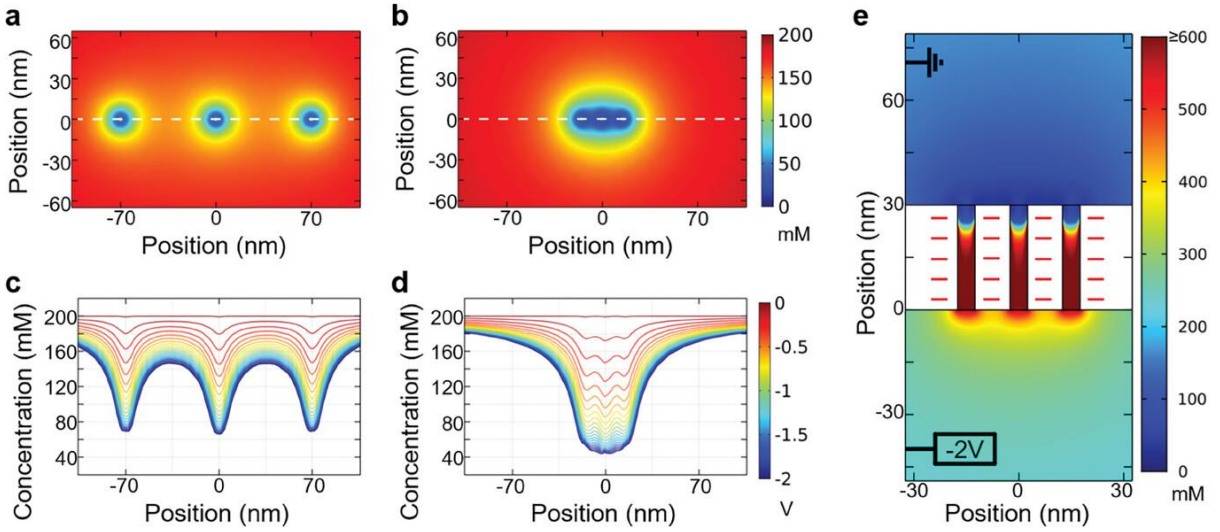

Figure 4.2 Simulated Ion Concentration Profiles. Openings of three neighboring nanopores with −2 V applied across the membrane in 100 mM KCl. The cumulative concentration of K^+ and Cl^- is shown. Formation of ion depletion zones (IDZ) for arrays with a) large interpore spacing of 70 nm and b) small interpore spacing of 15 nm at the side of the membrane that plays a role of cations source. Ion concentration along the white lines in (a,b) is shown in (c,d). IDZ overlap creates a more pronounced depletion in local ion concentrations in the tightly packed array d) compared to the array with pores spaced farther apart c). The magnitude of this depletion is also

dependent on the applied voltage. A cross section e) reveals the formation of the IDZ at the side of the membrane, and ion enhancement zones (IEZ) on the opposite side of the membrane. In (e) the interpore distance is 15 nm.

The numerical models considered three-nanopore arrays with interpore distances of 70 and 15 nm. Individual nanopores were 5 nm in diameter and 30 nm in length. The arrays were examined in 100 mM KCl under transmembrane voltages ranging from 0 to −2 V, with corresponding simulations also performed in 10 mM and 1 M KCl.

When neighboring nanopores were separated by 70 nm, the depletion region associated with each pore remained sufficiently localized that it did not substantially overlap with the depletion regions of neighboring pores. Under this condition, each nanopore behaved approximately independently and the array could be viewed as a collection of resistive elements connected in parallel.

A substantially different behavior emerged when the interpore distance was reduced to 15 nm. At this spacing, the depletion zones produced by individual nanopores overlapped strongly, reducing the local availability of ions for transport through each nanopore. At the entrances of these closely packed nanopores, the local ionic concentration was reduced by approximately 75%.

The depletion region was not confined exclusively to the membrane surface. Cross-sectional concentration profiles showed that the depletion zone extended approximately 10 nm into the nanopore interior. As the bulk concentration was reduced to 10 mM KCl, overlap between neighboring depletion regions became even more pronounced. Under these conditions, the local ionic concentration decreased to approximately 3 mM, corresponding to a reduction of approximately 85% relative to the bulk concentration.[88]

Even at 1 M KCl, where electrostatic surface charges are strongly screened, the influence of ICP was not completely eliminated. Although the minimum total ionic concentration was approximately 1.6 M, corresponding to a reduction of only approximately 20%, the depletion region still extended across all three nanopores when the interpore distance was 15 nm. These results demonstrate that ICP provides a mechanism through which neighboring nanopores can remain coupled even under relatively high ionic-strength conditions.

4.3 Ionic Conductance of Arrays with Different Interpore Distances as a Function of Salt Concentration

An individual nanopore can, to first approximation, be treated as a resistor within an ionic circuit.[76] Following this analogy, a nanopore array consisting of independently conducting pores can be represented as a collection of resistors connected in parallel. The equivalent resistance is therefore

$$\frac{1}{\Omega_{eq}} = \sum_i \frac{1}{\Omega_i} \tag{4.1}$$

which gives a total conductance

$$G_{eq} = \sum_i G_i \tag{4.2}$$

This treatment assumes that the ionic current through each nanopore is independent of transport through neighboring pores. The concentration profiles described above, however, indicate that ICP can violate this assumption when neighboring nanopores are sufficiently close.[78] Comparison between the experimentally measured array conductance, G_{exp}, and the conductance predicted by Equation 2 therefore provides a means of quantifying interpore interactions.

The experimentally measured conductance of each array was first compared with an equivalent conductance, $G_{eq,0}$, obtained by summing the bulk ionic conductances of the individual nanopores, $G_{0,i}$:

$$G_{eq,0} = \sum_i G_{0,i} \tag{4.3}$$

This calculation assumes that the nanopore walls carry no excess surface charge and that the pore interiors contain electrolyte at the bulk concentration. The subscript 0 denotes the absence of surface charge.

A relative conductance was then defined as

$$G_{rel,0} = \frac{G_{exp}}{G_{eq,0}} \tag{4.4}$$

for an array in which the constituent nanopores behave independently, $G_{rel,0}$ is expected to approach unity, particularly at high salt concentrations and large interpore distances. At high electrolyte concentrations such as 1 M KCl, surface charges are strongly screened and the nanopores can be approximated as uncharged pores filled with a solution of bulk conductivity.[62] ICP is also minimized under these conditions. Consequently, observing $G_{rel,0} \approx 1$ for widely separated nanopores provides evidence that all nanopores remain open for transport and that their conductance can be estimated from their geometrical dimensions.

The use of $G_{rel,0}$ also normalizes the measured conductance, allowing arrays containing nanopores with different average opening diameters to be directly compared. To determine $G_{0,i}$ the resistance of an individual nanopore, $\Omega_{0,i}$ was considered as the sum of its geometrical and access resistances. The nanopores were approximated as double-conical structures, consistent with previous descriptions of TEM-drilled nanopores,[97,98] with an estimated cone angle of 5.5°.

For this geometry, the geometrical resistance is

$$\Omega_{geom} = \frac{\mathrm{L}}{\kappa\pi\mathrm{r}\mathrm{R}} \tag{4.5}$$

where κ is the bulk electrolyte conductivity, L is the nanopore length, R is the pore opening radius, and $r = R - \frac{L}{2}\tan\theta$ is the minimum pore radius, assumed to occur at the center of the pore. The access resistance associated with the pore entrances is given by Hall's expression:[77]

$$\Omega_{access} = \frac{\mathrm{L}}{2\kappa\mathrm{R}} \tag{4.6}$$

The resulting resistance and conductance of an individual uncharged nanopore are therefore

$$\Omega_{0,i} = \frac{1}{\kappa}\left(\frac{L}{\pi r R} + \frac{1}{R}\right) \tag{4.7}$$

$$G_{0,i} = \kappa\left(\frac{L}{\pi r R} + \frac{1}{R}\right)^{-1} \tag{4.8}$$

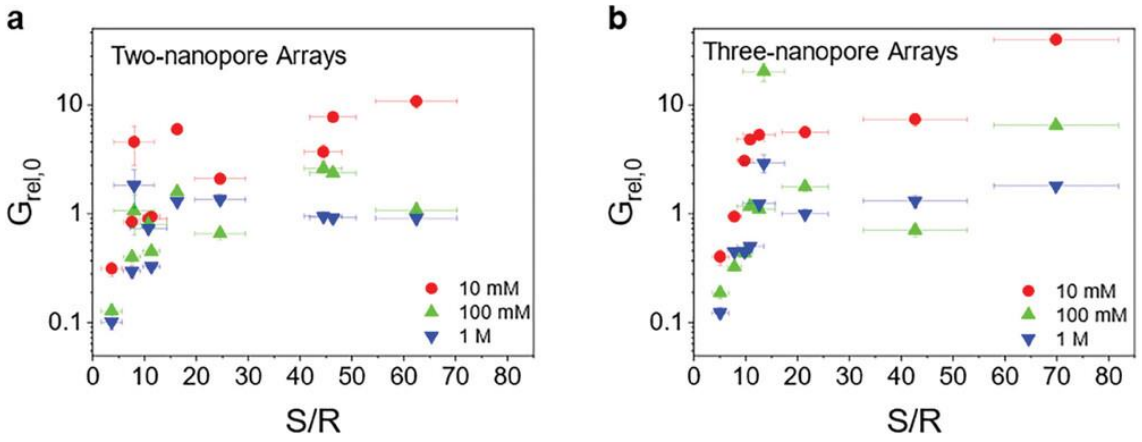

Figure 4.3 Relative conductance of arrays. $G_{rel,\,0}$, calculated as a ratio of experimentally measured conductance, G_{exp}, and summed conductances of constituent nanopores, $G_{eq,0}$ (Equation 4.4) assuming the pore walls did not carry any net charge. Results for arrays containing a) two and b) three nanopores are shown. At 10 mM, $G_{0,i}$ of individual nanopores underestimate the expected conductance due to the nanopores' surface charges enhancing ion transport across the pore.

Using these expressions, $G_{rel,0}$ was determined for the two- and three-nanopore arrays in 1 M, 100 mM, and 10 mM KCl. For S/R > 20 in 1 M KCl, $G_{rel,0}$ remained close to unity, confirming that the constituent nanopores remained open and that their resistance could be reasonably estimated from the pore diameters measured by TEM. A similar result was observed in 100 mM KCl for nearly all arrays with S/R > 20.

As the interpore distance decreased, however, the experimentally measured conductance increasingly deviated from the prediction based on independent nanopores. For S/R < 15, the measured conductance in both 1 M and 100 mM KCl could be as much as ten times smaller than the value predicted by Equation 4.8. These measurements demonstrate that the interdependence of transport through neighboring nanopores cannot be neglected in closely packed arrays, even under high-salt conditions.

A different trend was observed in 10 mM KCl. At this concentration, the electrical double-layer thickness becomes comparable to the nanopore radius. Surface charge can therefore increase the concentration of counterions within the nanopore above the bulk concentration, increasing conductance relative to an otherwise identical uncharged pore.[62,87] Consequently, $G_{rel,0}$ underestimates the expected conductance in 10 mM KCl, allowing $G_{rel,0}$ to exceed unity.

For S/R > 20, values of $G_{rel,0}$ as large as approximately 10 were observed, indicating strong surface-charge-assisted ionic transport in more widely separated nanopores, consistent with behavior previously observed in individual nanopores.[87] As the nanopores became more closely packed, however, ICP increasingly suppressed ionic transport, eventually reducing the measured conductance below the value predicted for uncharged nanopores such that $G_{rel,0} < 1$.

The error associated with these measurements was determined from the linear regression used to obtain conductance from the current–voltage curves and from variations in the radii of

the constituent nanopores. Current–voltage curves were obtained by averaging at least three consecutive voltage scans between −2 and +2 V, after which linear regression was performed between −1 and +1 V. Variations in nanopore dimensions within a given array were quantified using the standard deviation of the constituent pore diameters.

These observations demonstrate that surface charge can influence nanopore conductance through two competing mechanisms. First, surface charge enhances conductance by increasing the concentration of counterions inside the nanopore to maintain electroneutrality.[62,87] Second, surface charge in combination with an applied electric field produces concentration polarization, which can reduce ionic concentrations near the pore entrances and thereby suppress transport.[88,99]

Although $G_{eq,\sigma}$, is useful at high salt concentrations, it does not directly quantify the magnitude of ICP-induced current suppression at low electrolyte concentrations. To describe transport in 10 mM KCl more accurately, the surface-charge-assisted conductance, G_σ, was therefore considered as a contribution that conducts current in parallel with the geometric conductance.[91,94]

This contribution is given by

$$G_\sigma = \frac{3\pi rR(r+R)\sigma_p \mu_{K^+}}{L(r^2+rR+R^2)} \tag{4.9}$$

where μ_{K^+} is the mobility of potassium ions and σ_p is the surface charge density of the nanopore walls. Including the surface-charge contribution gives the predicted conductance of each nanopore as

$$G_{\sigma,i} = 2R\left\{\frac{1}{\kappa} + \frac{2L}{\pi r\left[\kappa + \frac{3\mu_{K^+}\sigma_p(r+R)}{r^2+rR+R^2}\right]}\right\}^{-1} \tag{4.10}$$

The additional ionic conductance arising from the surface charge density, along the pore walls can be treated as a contribution acting in parallel with the conductance associated with the electrolyte-filled pore volume. For a cylindrical nanopore, the surface-charge contribution to the conductance is given by

$$G_\sigma = 4\sigma_p \mu_{K^+} \frac{\pi r}{L}$$

where is the mobility of potassium ions, is the pore radius, and is the pore length. Extending this treatment to the double-conical pore geometry considered here gives

$$G_\sigma = \frac{3\pi r R(r+R)\sigma_p \mu_{K^+}}{L(r^2 + rR + R^2)}$$

Because surface-charge-mediated transport occurs in parallel with ionic conduction through the pore volume, the total pore conductance can be represented by an equivalent circuit containing these two contributions. Combining the bulk and surface conductance terms with the access resistance yields the equivalent conductance given in Equation (4.10).

Predicted conductance of an array, $G_{eq,\sigma}$, was then calculated by adding $G_{\sigma,i}$ of all constituent nanopores

$$G_{\mathrm{eq},\sigma} = \sum_i G_{\sigma,i.} \tag{4.11}$$

A second relative-conductance parameter was consequently defined as

$$G_{\mathrm{rel},\sigma} = \frac{G_{\mathrm{exp}}}{G_{\mathrm{eq},\sigma}}. \tag{4.12}$$

As with $G_{\mathrm{rel},0}$, a value of $G_{\mathrm{rel},\sigma} = 1$ indicates negligible interaction between neighboring charged nanopores, whereas $G_{\mathrm{rel},\sigma} < 1$ indicates conductance suppression caused by interpore coupling. In Figure 4.4 values of $G_{\mathrm{rel},\sigma}$ were determined in 10 mM, 100 mM, and 1 M KCl for two- and three-nanopore arrays using a pore-wall surface charge density of −50 mC/m².[94] The relatively

large standard deviations arise from uncertainties in the current measurements and the finite precision associated with determining nanopore diameters.

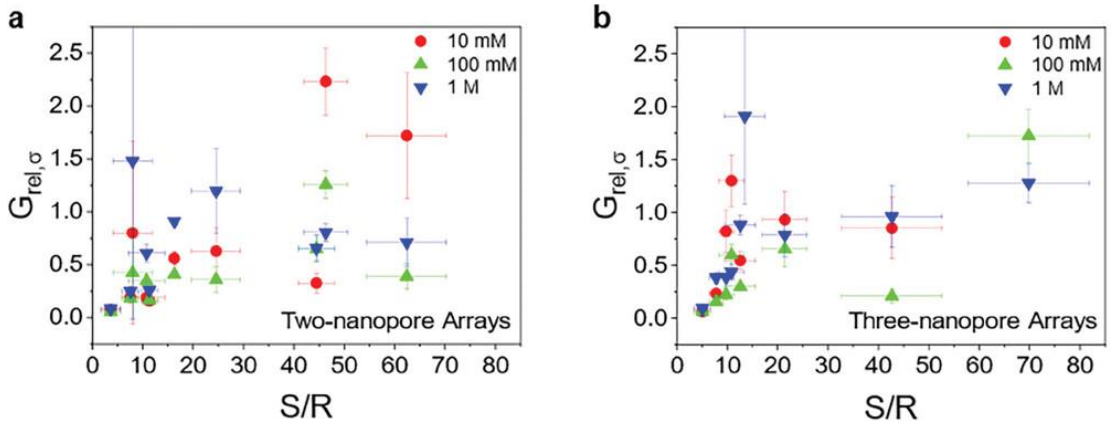

Figure 4.4 Experimentally Measured Conductance of Arrays. G_{exp}, divided by summed conductance of constituent nanopores, $G_{eq,\sigma}$, assuming the pore walls carried surface charge of −50 mC/m^{-2}. The ratio is defined in Equation (4.12) as $G_{rel,\sigma}$. At low S/R, the experimentally measured conductance is suppressed relative to the expected conductance, indicating strong interpore interactions. The error bars were obtained using the same methods as reported in Figure 4.3.

The three-nanopore arrays exhibited clear conductance suppression at small S/R for all electrolyte concentrations. The suppression also tended to become stronger as the electrolyte concentration decreased. The trend was less pronounced for two-nanopore arrays. This difference was attributed to the smaller number of neighboring pores in the two-pore system, where each nanopore interacts with only one neighboring pore, making the effects of interpore coupling more difficult to resolve experimentally.[88]

4.4 Numerical Modeling of Ion Current in Nanopore Arrays

Finite-element modeling of ionic current through two- and three-nanopore arrays was performed to further investigate the relationship between nanopore proximity and total array conductance.[88] For the numerical models, relative conductance was calculated by dividing the conductance of an array containing N nanopores, $G_{model,N}$, by N times the conductance of a single nanopore, $G_{model,1}$:

$$\frac{G_{\mathrm{model},N}}{N \times G_{\mathrm{model},1}}. \tag{4.13}$$

This quantity can be directly compared with the experimentally determined $G_{rel,\sigma}$ defined in Equation 4.12.

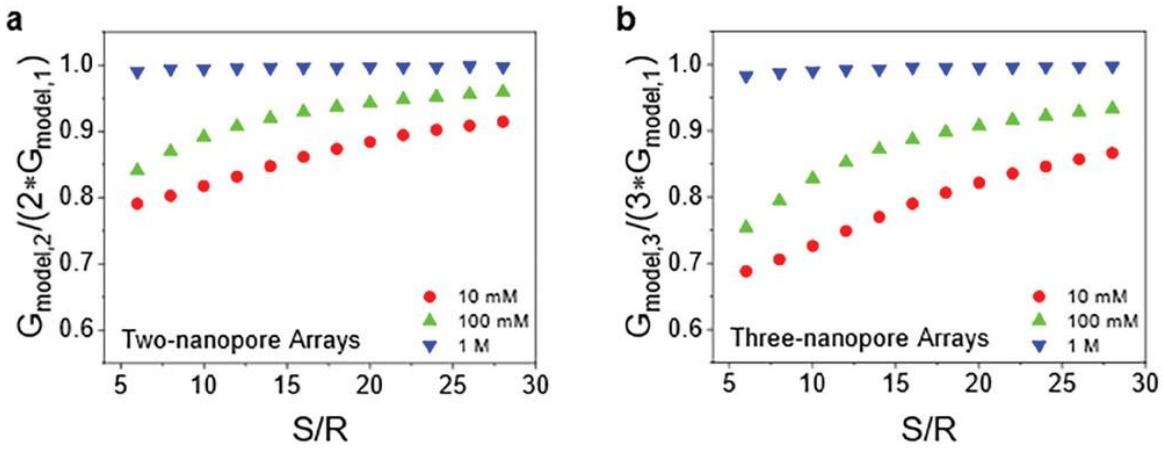

Figure 4.5 Computationally Modeled Relative Conductance. Arrays containing two nanopores a) and three nanopores b). Nanopores are 5 nm in diameter and 30 nm in length and carry a surface charge density on the pore walls of − 50 mC/m^{-2}. The ratio $G_{model,N}/(N*G_{model,1})$ compares the conductance of an N-sized array to that of N number of charged pores conducting current independently. Pore–pore interactions are indicated by $G_{model,N}/(N*G_{model,1}) < 1$.

The numerical simulations reproduced the experimentally observed suppression of conductance in closely packed nanopore arrays. The simulations further showed that conductance suppression becomes stronger and persists over larger interpore distances as the bulk electrolyte concentration decreases. This behavior originates from the IDZs produced at the nanopore entrances by concentration polarization.[88]

The simulations also predicted a greater reduction in relative conductance for three-nanopore arrays than for two-nanopore arrays, consistent with both the experimental measurements and previous studies.[76,78,88]

The magnitude of conductance suppression predicted numerically was in semiquantitative agreement with the experimental results. However, the experimentally measured conductance of tightly packed arrays was generally lower than predicted by the model. This discrepancy may arise from the simplified cylindrical nanopore geometry used in the simulations and from the omission of surface charges on the external membrane surfaces.

The simulations described above assumed a pore-wall surface charge density of −50 mC/m², consistent with the value used to determine $G_{rel,\sigma}$.[94] The extent to which ICP alters local ionic concentrations at nanopore entrances is, however, also dependent on the magnitude of the pore-wall surface charge.[82]

Additional simulations were therefore performed for three-nanopore arrays with surface charge densities ranging from −10 to −70 mC/m². These calculations confirmed that the magnitude of the pore-wall surface charge directly influences the degree of conductance suppression. Surface charge therefore represents an additional parameter through which the dependence of individual nanopore transport on neighboring pores can be controlled.

4.5 Tuning Conductance of Arrays by Introducing Surface-Charge Patterns

The experiments and simulations involving homogeneously charged nanopores demonstrated that ICP generated by surface charge and applied voltage can produce significant interactions between neighboring nanopores and suppress the overall conductance of an array. The next question was whether these interactions could be controlled by deliberately modifying the transport properties of the constituent nanopores. Specifically, it was important to determine whether the characteristic transport behavior of individual nanopores would be preserved within an interacting array or whether the depletion region generated by ICP would dominate the transport response.

This question is particularly important for the development of biomimetic nanopore arrays, where the desired functionality ultimately depends on interactions among nanopores that may exhibit different transport characteristics when studied individually.[72] Because nanopore transport can be controlled by introducing surface-charge patterns along the pore walls,[63] these patterns also provide a possible mechanism for controlling ICP and, consequently, interpore interactions.

To investigate this possibility, arrays were considered in which each constituent nanopore functioned as an ionic diode. Ionic diodes behave as nanoscale switches that preferentially transport ions for one voltage polarity. A nanopore or nanochannel can exhibit diode-like behavior when its electrochemical symmetry is broken, for example by creating a junction between regions carrying negative and positive surface charges.[57,63,93]

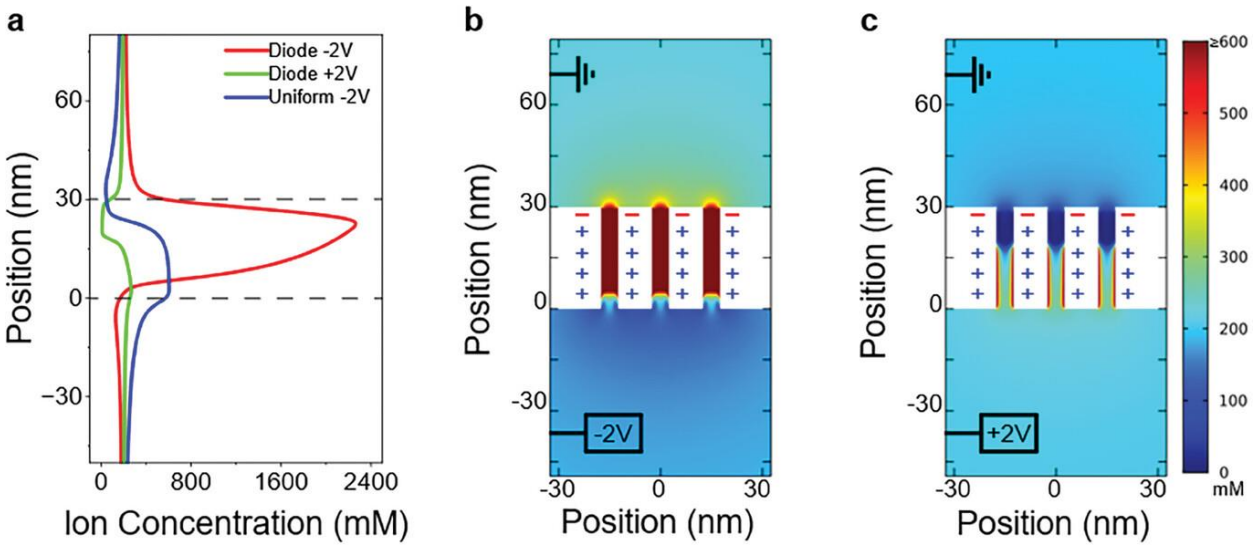

Figure 4.6 Ion Concentration Profiles Heterogeneous Surface-Charged Models. Array of pores containing a junction between a zone with positive surface charges and a zone with negative charges at 100 mM KCl. The interpore distance in the array is 15 nm. a) The distribution of total ion concentration along the central pore axis for the centermost pore in an array containing ionic diodes (in red and green). For comparison, ionic concentration in a middle nanopore in an array consisting of homogeneously charged nanopores is shown as well (in blue). The dashed lines indicate the pore location. b,c) Cross-section heat map of local ionic concentrations in (b) the "on" state of the diode and (c) the "off" state of the diode.

Arrays of ionic diodes therefore provide a model system for examining the relationship between pore-wall charge distribution and total array conductance. The hypothesis was that arrays consisting of ionic diodes would experience a different degree of conductance suppression than arrays containing homogeneously charged nanopores with otherwise identical geometrical properties.

The local ionic concentrations within diode arrays were first examined numerically. In these simulations, 80% of each nanopore wall carried positive surface charge while the remaining 20% remained negatively charged. This surface-charge pattern was selected because it

had previously been achieved experimentally in individual silicon nitride nanopores using asymmetric amination.[46]

The unmodified region was assigned a surface charge density of −50 mC/m², whereas the aminated region was assigned +50 mC/m².

For an applied voltage of −2 V, the total ionic concentration within the nanopore increased, producing the conducting, or "on," state of the diode. At +2 V, the nanopore instead became strongly depleted of ions, producing the "off" state.

Reversing the surface charge over the majority of the nanopore wall also reversed the locations of the IEZ and IDZ relative to the applied voltage compared with homogeneously negatively charged nanopores. Importantly, the IDZ associated with the "on" state of the diode array contained substantially higher ionic concentrations than the corresponding depletion region in arrays of homogeneously charged nanopores.

For example, for an interpore distance of 15 nm in 100 mM KCl, the minimum total ionic concentration in the diode array was approximately 140 mM. Under otherwise equivalent conditions, the ionic concentration in an array of homogeneously negatively charged nanopores decreased to approximately 40 mM.

The influence of these weaker depletion zones on interpore interactions was then quantified by modeling current–voltage characteristics for arrays containing two and three ionic diodes in 10 mM, 100 mM, and 1 M KCl and comparing the results with current–voltage curves obtained for individual diodes.

When the potential difference was applied from the side of the nanopore carrying positive surface charge, the magnitude of the negative current was predicted to exceed that of the positive current.[64,100]

Because ionic diodes exhibit nonlinear current–voltage characteristics, the analysis used the current measured at −2 V rather than a conductance obtained from linear regression. Relative current was calculated by dividing the current through an array by the current through a single diode multiplied by the number of nanopores in the array.

The simulations showed that ionic current through diode arrays remained suppressed relative to the current expected from noninteracting diodes. However, the magnitude of this suppression was appreciably smaller than that observed for arrays containing homogeneously charged nanopores.

The enhanced ion transport through arrays of ionic diodes may also contribute to the improved osmotic energy conversion previously reported for rectifying membranes relative to homogeneously charged membranes.[70,90,93]

The final question was whether an array composed of ionic diodes would retain the nonlinear transport characteristics of the individual constituent diodes. To quantify this behavior, the ion current rectification ratio was defined as[63]

$$\mathrm{ICR} = \left|\frac{I_{-2\mathrm{V}}}{I_{+2\mathrm{V}}}\right|. \tag{4.14}$$

The ICR was evaluated as a function of S/R in 10 mM, 100 mM, and 1 M KCl. The numerical results predicted ion current rectification for all interpore distances and electrolyte concentrations considered. In addition, the magnitude of rectification exhibited only a relatively weak dependence on interpore spacing.

These simulations therefore predicted that ion current rectification is a robust transport property that can be preserved even when ionic diodes are positioned sufficiently close for their depletion regions to interact.

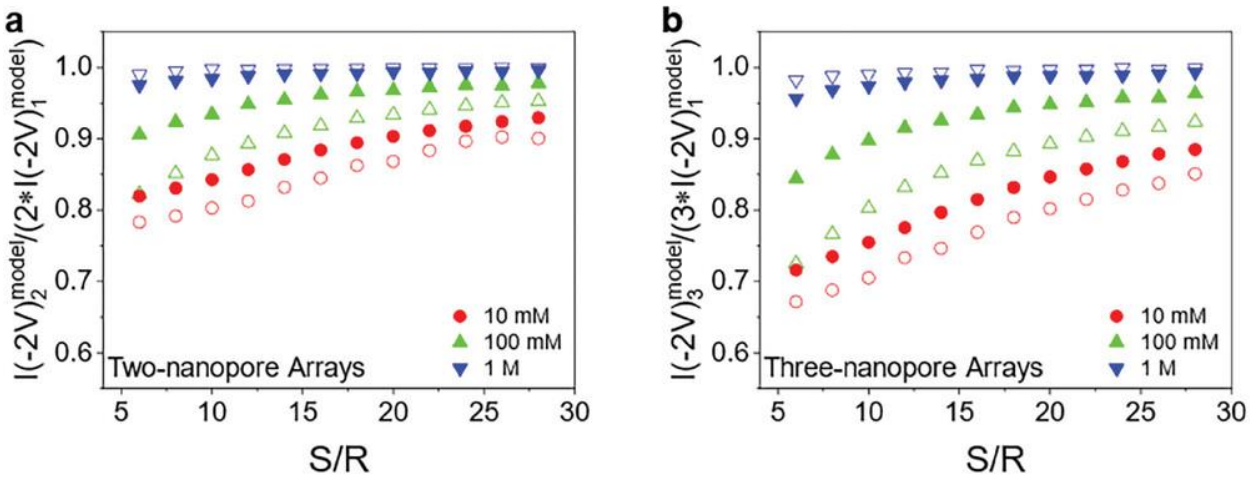

Figure 4.7 Comparison of simulated relative Ion Currents. Nanopore arrays pre- and post-modification with APTMS. Arrays containing two ionic diodes a) and three ionic diodes b) are shown. Filled points represent the current ratio of diode arrays and unfilled points represent the current ratio of arrays of nanopores with uniform negative charge. The APTMS modification mitigates current suppression at small values of S/R as shown by the higher relative current ratios for the chemically modified nanopores.

To experimentally test this prediction, junctions between positively and negatively charged surface regions were introduced into two- and three-nanopore arrays using a procedure previously developed for individual nanopores. One side of the nanopore array was exposed to a 1% solution of 3-(aminopropyl)trimethoxysilane (APTMS) for 30 min, resulting in amination of approximately 80% of the nanopore walls.[46]

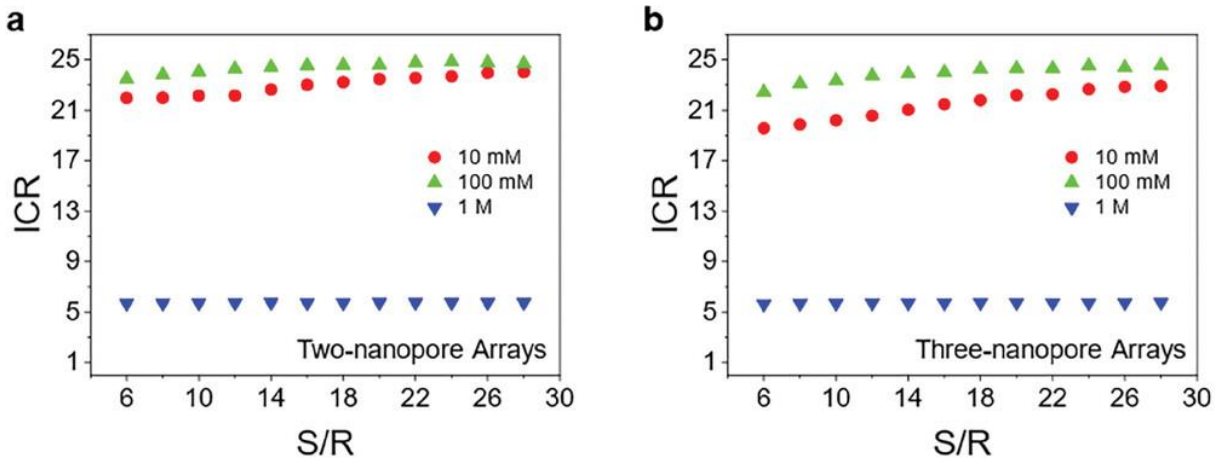

Figure 4.8 Simulated Ion Current Rectification (ICR) Two-nanopore arrays a) and three-nanopore arrays b) as a function of pore proximity S/R. Current rectification is predicted to occur for all KCl concentrations and S/R we considered. ICR is defined by Equation 4.13.

Transport through the partially aminated arrays was subsequently measured in 10 mM, 100 mM, and 1 M KCl at pH 7, where the silanol groups are deprotonated and the amine groups are protonated.

Current–voltage measurements of a two-nanopore array with S/R = 7.5 and a three-nanopore array with S/R = 13 confirmed that the surface-charge pattern produced ion current rectification even in tightly packed nanopore arrays. The experimental results therefore supported the numerical prediction that diode behavior can be retained despite strong spatial coupling between neighboring nanopores.

The two-nanopore array contained pores with diameters larger than the 5 nm pores used in the numerical model, contributing to the smaller experimentally measured ICR and the apparent absence of rectification in 1 M KCl. More generally, the experimentally observed ICR values were smaller than those predicted numerically. One possible explanation is the finite spatial width of the transition between the positively and negatively charged regions in the experimental nanopores, whereas the numerical model assumes an infinitely sharp junction.

Previous simulations have demonstrated that sharper transitions between oppositely charged regions produce stronger ion current rectification.[101]

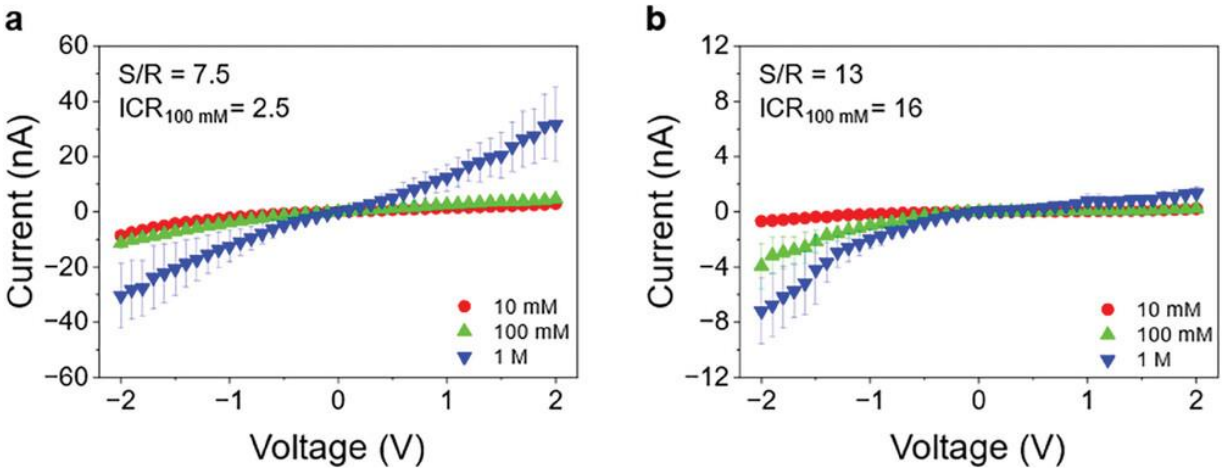

Figure 4.9 Experimental Recordings of Current–Voltage Curves. a) Two and b) three nanopore arrays consisting of ionic diodes. The bipolar surface charge distribution leads to ion current rectification even for arrays with small S/R. The arrays shown in (a) and (b) have an average opening diameter of 7 and 3 nm, respectively. The current–voltage curves represent the average of at least three subsequent voltage scans, and the error bars are standard deviations.

4.6 Reflections and Summary

The results presented in this chapter identify several fundamental phenomena that become important when a single-nanopore system is extended to arrays of closely spaced nanopores. The nanopores investigated here possess aspect ratios greater than unity, such that their transport properties are controlled by both the electrochemical characteristics of the nanopore walls and ion concentration polarization.

Experimental measurements and numerical modeling demonstrate that significant interactions occur even in minimal arrays containing only two or three nanopores. These

interactions alter the total ionic conductance of the array relative to the conductance expected from independently operating nanopores.

The coupling between neighboring nanopores is mediated by the ion depletion zones generated by ICP. As the distance between nanopores decreases, the depletion regions associated with neighboring pores begin to overlap. The extent of this overlap depends on electrolyte concentration, applied voltage, and the electrochemical properties of the nanopore walls. In arrays containing closely packed, homogeneously charged nanopores, the overlapping depletion zones reduce the availability of ions near the pore entrances and suppress the total ionic conductance.

The magnitude of this current suppression can be modified through chemical functionalization of the nanopore walls. Introducing a junction between regions carrying positive and negative surface charges produces ionic diodes and reduces the severity of the depletion region in the conducting state. Consequently, arrays of ionic diodes exhibit less current suppression than arrays of homogeneously charged nanopores with otherwise similar geometrical properties.

Importantly, the diode-like behavior of individual nanopores was preserved even in the most closely packed arrays considered. These results demonstrate that the electrochemical properties of nanopore walls can be used not only to control the transport characteristics of individual nanopores but also to tune the strength of interactions between neighboring nanopores.

Together, these findings provide an important foundation for extending nanopore systems beyond isolated pores toward arrays containing interacting components. Such systems could ultimately enable the construction of biomimetic ionic circuits,[86,93,102] including devices capable

of controlled feedback and systems in which electrochemical signals propagate through space and time.

4.7 Nanopore Fabrication and Electrochemical Measurements

All nanopore arrays were fabricated by electron-beam drilling of freestanding 30 nm thick silicon nitride membranes using a JEOL 2100F transmission electron microscope (TEM).[54] Individual nanopore diameters and center-to-center interpore distances were determined from TEM micrographs.

Because the electron-beam drilling process produced small variations in nanopore dimensions, an average pore radius, R, and average interpore spacing, S, were calculated for each array. The normalized ratio S/R was subsequently used as the primary measure of nanopore proximity.

Before electrochemical measurements, the membranes were cleaned and rendered hydrophilic by immersion for 1 h in piranha solution, consisting of a 3:1 mixture of H_2SO_4/H_2O_2, heated to 120 °C.

Ion transport through the nanopore arrays was characterized by recording current–voltage curves over a broad range of KCl concentrations using a Keithley 6487 picoammeter/voltage source and a pair of Ag/AgCl pellet electrodes.

For each electrolyte concentration, at least three forward and reverse voltage scans were performed between −2 and +2 V using 100 mV increments. Average ionic currents and corresponding standard deviations were calculated from these measurements.

For conductance measurements, linear fits were performed over the voltage range from −1 to +1 V. The corresponding standard deviations include uncertainties associated with these

linear fits. For measurements of ion current rectification, average values and standard deviations were obtained directly from at least three voltage scans.

In-house Python scripts were used to analyze and plot all current–voltage measurements. Electrolyte solutions were buffered to pH 8 for experiments involving unmodified silicon nitride nanopores. At this pH, the surface silanol groups are deprotonated, producing a uniformly negative surface charge along the nanopore walls.

4.8 Introduction of Positive Surface Charges

Positive surface charges were introduced through modification with APTMS. The nanopore devices were mounted between in-house PDMS-based microchannel devices. The bottom channel was filled with a 1% solution of APTMS in ethanol, while the top channel contained ethanol only.[46,67]

The devices were exposed to the modification solution for 30 min, rinsed with ethanol, and subsequently heated at 70 °C for 60 min. Arrays modified with APTMS were characterized electrochemically using KCl solutions buffered to pH 7.

4.9 Computational Modeling of Nanopore Arrays

Finite-element simulations were performed using COMSOL Multiphysics. Ionic transport was described using the coupled Poisson–Nernst–Planck equations to determine the spatial distributions of ionic concentration and electric potential and to calculate ionic current throughout the computational domain.[88]

Three-dimensional models were constructed for arrays containing two and three nanopores. Corresponding single-nanopore models were also constructed to provide reference systems for determining the relative conductance and relative current of the arrays.

In all simulations, the nanopores were modeled as cylindrical channels with radii of 2.5 nm and lengths of 30 nm. The nanopores connected two cylindrical reservoirs, each with a height and radius of 0.5 μm. Center-to-center interpore distances ranging from 15 to 70 nm were considered.

Surface charge was applied to the internal walls of the nanopores. A surface charge density of −50 mC/m² was used to model unmodified silicon nitride nanopores, while regions modified with APTMS were assigned a surface charge density of +50 mC/m².

CHAPTER 5 Ion Concentration Polarization and Pore-Length-Independent Nanopore Conductance

The presence of surface charge within a nanopore provides one of the primary mechanisms through which ionic transport can be controlled at the nanoscale. When the nanopore radius becomes comparable to the Debye screening length, electrostatic interactions between the charged pore walls and mobile ions can strongly modify the ionic composition within the pore. Negatively charged nanopores preferentially attract cations and exclude anions, whereas positively charged nanopores preferentially attract anions and exclude cations.[30,62,87,91,103–107] Consequently, when an electric field is applied across a sufficiently selective nanopore, the ionic current can be carried predominantly by one type of charge carrier.

The degree of ion selectivity, however, depends not only on the nanopore diameter and surface charge, but also on the length of the nanopore. Previous numerical studies have demonstrated that ion selectivity decreases as the nanopore length approaches the pore diameter, particularly when the external membrane surfaces remain uncharged.[90,108] Thus, maximizing both ionic conductance and selectivity requires consideration of pore length in addition to pore diameter and surface chemistry.[90,109]

Understanding the relationship between nanopore length, conductance, and ion selectivity is particularly important for applications that rely on selective ionic transport. One prominent example is osmotic energy conversion, in which an ion-selective nanopore or nanoporous membrane separates electrolyte solutions of different concentrations.[110–112] A naturally occurring concentration gradient, such as that formed where freshwater and seawater meet, can provide the chemical potential required to drive selective ionic transport and generate an electrical potential across the membrane.[113] Several single-nanopore systems have demonstrated substantial osmotic

energy conversion efficiencies, motivating continued interest in nanoporous membranes for so-called blue-energy technologies.[110,111,113,113,114]

From a purely geometrical perspective, decreasing nanopore length is attractive because a shorter conducting pathway is generally expected to produce lower electrical resistance and therefore larger ionic current. This simple relationship becomes considerably more complicated, however, when nanopores are arranged into arrays. In nanoporous membranes, ion concentration polarization can reduce the effective concentration gradient experienced by neighboring nanopores and substantially decrease the power-conversion efficiency of the membrane.[90,92] Consequently, maximizing nanopore conductance cannot be accomplished simply by reducing membrane thickness or increasing nanopore density.

Ion concentration polarization (ICP) occurs when selective ionic transport produces unequal ion distributions on opposite sides of a nanopore or membrane.[63,92] Under an applied electric field, selective transport produces a region of reduced ionic concentration on one side of the nanopore and a region of enhanced ionic concentration on the opposite side. These regions are commonly referred to as the ion depletion zone (IDZ) and ion enrichment zone (IEZ), respectively. Importantly, these concentration changes are not necessarily restricted to the external reservoirs. ICP can also substantially modify ionic concentrations within the nanopore itself, thereby changing the local conductivity and effective electrical resistance of the channel.

The effects of ICP become especially important when multiple nanopores are positioned near one another. In closely spaced nanopore arrays, the depletion zones generated by neighboring pores can overlap, causing transport through one nanopore to become dependent on transport through neighboring nanopores.[78,86,92] Previous work demonstrated that this coupling can suppress the ionic conductance of nanopore arrays relative to the conductance expected from

an equivalent number of independently operating pores.[2] The spatial extent and magnitude of these depletion regions depend on electrolyte concentration, applied voltage, nanopore geometry, and surface charge, making ICP a central consideration in the design of both individual nanopores and nanoporous membranes.

This chapter examines how nanopore length influences ionic conductance, ion selectivity, and ICP in individual nanopores and small three-nanopore arrays. Particular emphasis is placed on identifying conditions under which the conventional relationship between pore length and resistance no longer adequately describes ionic transport. Cylindrical nanopores with a constant diameter of 5 nm and lengths of 5, 10, 20, and 30 nm are considered, while the center-to-center distance between neighboring pores in the arrays is maintained at 15 nm. The pore walls carry surface charge, whereas the external membrane surfaces remain uncharged.

The results reveal a surprising regime in which ionic conductance becomes nearly independent of the physical nanopore length. At low electrolyte concentrations and sufficiently low applied voltages, nanopores with substantially different lengths can conduct nearly identical ionic currents. This behavior originates from ICP, which modifies ionic concentrations not only near the pore entrance but also throughout a significant portion of the nanopore interior.[78,80–82] As a result, the effective resistance of the system is determined by the spatial extent and magnitude of the depletion region rather than simply by the physical length of the nanopore.

The relationship between ICP and ion selectivity is particularly important in understanding this behavior. Ion concentration polarization requires selective transport, and therefore changes in nanopore selectivity can directly alter the magnitude of the depletion and enrichment regions.[78,86,92] Very short nanopores can lose ion selectivity as the applied voltage increases, thereby weakening ICP and changing the expected relationship between pore length and ionic

current.[109] Consequently, pore length, applied voltage, electrolyte concentration, and ion selectivity must be considered collectively rather than as independent parameters.

In addition to homogeneously charged nanopores, this chapter examines nanopores containing a junction between regions carrying positive and negative surface charges. Such bipolar surface-charge distributions break the electrochemical symmetry of the nanopore and produce ionic diode behavior, in which the magnitude of ionic current depends strongly on the polarity of the applied voltage.[86,100] These systems provide an important comparison with homogeneously charged nanopores because the principal regions of ion depletion and enrichment can develop within the nanopore itself near the junction between oppositely charged surfaces.

Together, the results presented in this chapter establish that the electrical resistance of a charged nanopore cannot always be inferred directly from its physical dimensions. Instead, nanopore conductance emerges from the coupled effects of pore geometry, surface charge, electrolyte concentration, applied voltage, ion selectivity, and the spatial redistribution of ions caused by ICP. Understanding these relationships provides important design principles for selective nanopores, nanopore arrays, separation membranes, and systems intended for osmotic energy conversion.

5.1 Computational Methods

Ionic transport through individual nanopores and three-nanopore arrays was investigated using three-dimensional finite-element simulations performed in COMSOL Multiphysics. The ionic concentration and electric potential distributions were determined by solving the coupled Poisson–Nernst–Planck equations.

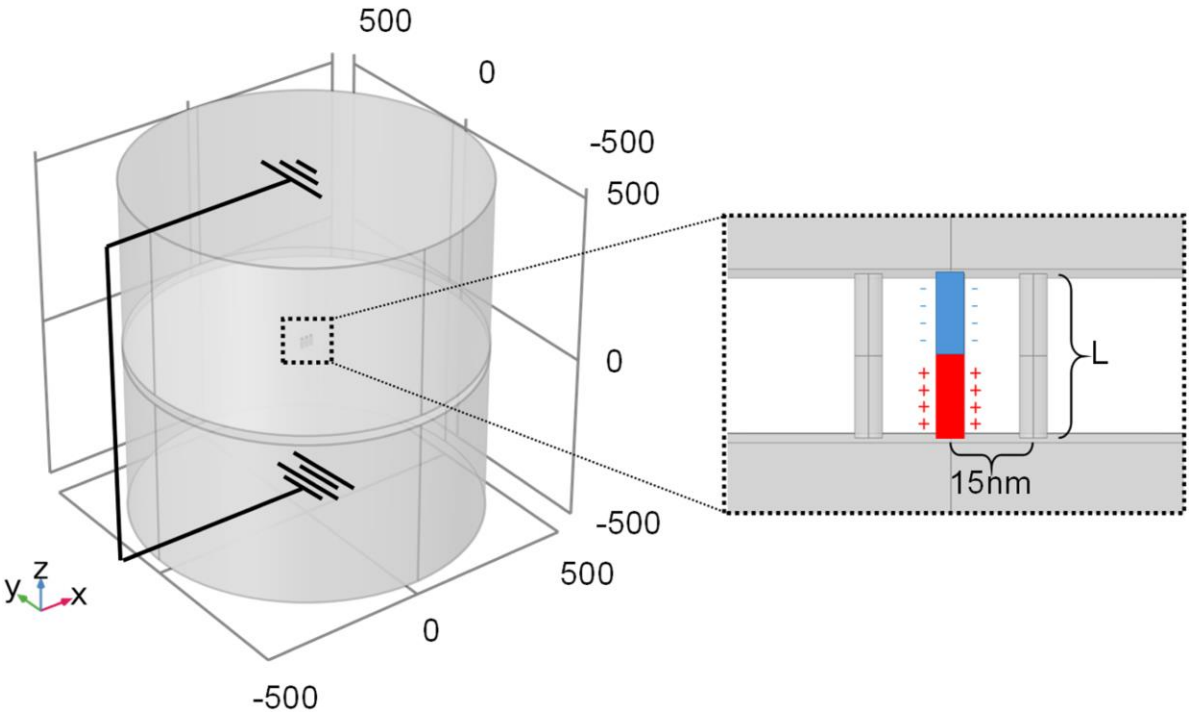

Figure 5.1 Geometrical Setup for Nanopore-Array Modeling. Cylindrical reservoirs of 0.5 μm radius and 0.5 μm height are connected with a membrane containing a single nanopore or a 3-nanopore array with the pore-to-pore distance set to 15 nm. The nanopore diameter was 5 nm in all simulations, while the pore length, L, was varied between 5 nm and 30 nm. Blue and red regions indicate negatively and positively charged pore walls, respectively.

The electrostatic potential was described using Poisson's equation,

$$\nabla \cdot (\varepsilon \nabla \varphi) = -F \sum_i z_i \, c_i \tag{5.1}$$

where φ is the electric potential, ε is the fluid permittivity, F is the Faraday constant, z_i is the valence of ionic species i, and c_i is its local concentration. Transport of each ionic species was described using the steady-state Nernst–Planck equation,

$$\nabla \cdot \mathbf{J}_i = \nabla \cdot \left[-D_i \nabla c_i - \frac{z_i F}{RT} D_i c_i \nabla \varphi \right] = 0 \tag{5.2}$$

where J_i is the flux of ionic species i, D_i is the corresponding diffusion coefficient, R is the universal gas constant, and T is the absolute temperature.

Equation 5.2 accounts for the two transport mechanisms considered in the model: diffusion produced by concentration gradients and electromigration produced by the local electric field. Coupling this equation to Poisson's equation allows the ionic concentration and electric potential distributions to be determined self-consistently throughout the nanopore and reservoirs.

Both K^+ and Cl^- were assigned diffusion coefficients of $D_{K^+} = D_{Cl^-} = 2 \times 10^{-9}\ \mathrm{m^2\ s^{-1}}$. The relative permittivity of the electrolyte was taken as 80. Three-dimensional models were required because the nanopore arrays lacked axial symmetry. The Navier–Stokes equations were initially considered; however, including fluid flow produced negligible changes in the predicted transport behavior while substantially increasing computational cost and convergence time. Fluid flow was therefore omitted from the final simulations.[115] The models consequently describe transport through diffusion and electromigration without including electroosmotic or pressure-driven convection.

The simulations also did not include ion adsorption onto the nanopore walls. Adsorbed ions can alter the effective surface-charge density and therefore modify nanopore selectivity.[116] In the present model, the imposed surface-charge density was instead treated as a fixed electrostatic boundary condition.

5.2 Nanopore Geometry

The basic computational geometry consisted of either a single cylindrical nanopore or a three-nanopore array positioned between two cylindrical electrolyte reservoirs. This geometry

follows the modeling framework previously used to investigate interactions between neighboring nanopores.[2]

Each reservoir had a radius and height of 0.5 μm. The nanopore diameter was fixed at 5 nm, while the pore length, L, varied systematically among 5, 10, 20, and 30 nm. Additional calculations with nanopores as long as 100 nm were performed to determine the pore-length regime in which ionic conductance begins to recover the conventional geometrical dependence on L.

For three-nanopore arrays, the center-to-center interpore distance was fixed at 15 nm. This spacing places neighboring nanopores sufficiently close for their ICP-induced depletion zones to interact and overlap.[2,75,78,96,117] The array geometry therefore provides a direct comparison between transport through an isolated nanopore and transport through nanopores subjected to interactions with neighboring pores.

The electrolyte consisted of KCl at bulk concentrations of 10 mM, 100 mM, and 1 M. These concentrations were selected to examine transport over conditions ranging from strong surface-charge-mediated behavior at low ionic strength to strongly screened surface-charge effects at high ionic strength. A transmembrane potential was swept between −2 and +2 V using increments of 0.2 V and, for selected analyses requiring greater resolution, increments of 0.1 V.

5.3 Surface-Charge Configurations

Two distinct nanopore surface-charge configurations were considered.
The first consisted of nanopores carrying a homogeneous negative surface-charge density along the entire internal pore wall, $\sigma = -0.05\ \mathrm{C\,m^{-2}}$.

The external membrane surfaces remained uncharged. These nanopores preferentially transport cations and consequently provide a model system for examining ICP associated with a uniformly charged, ion-selective nanopore.

The second configuration consisted of nanopores containing a junction between oppositely charged regions. One half of the nanopore wall carried a positive surface-charge density, $\sigma = +0.05\ \mathrm{C\,m^{-2}}$, while the remaining half carried $\sigma = -0.05\ \mathrm{C\,m^{-2}}$. The positively and negatively charged regions were equal in length.

Nanopores containing junctions between oppositely charged regions are known to behave as ionic diodes.[63,64,100] Reversing the polarity of the applied voltage alters whether ions become enriched or depleted near the internal charge junction, producing strongly asymmetric current–voltage characteristics.

Comparing these bipolar nanopores with homogeneously negatively charged nanopores makes it possible to determine how the spatial location of concentration polarization influences the relationship among pore length, conductance, and ion selectivity.

5.4 Ion Concentration Polarization in Nanopores of Varying Length

The transport properties of charged nanopores cannot be understood by considering the nanopore interior independently from the surrounding electrolyte reservoirs. Under an applied transmembrane potential, ICP modifies the local ionic concentrations at the nanopore entrances and can extend into the nanopore itself.[78,80–82,117] These changes in local concentration alter both ionic conductivity and the spatial distribution of the applied electric potential.

The effects become particularly important in nanopore arrays. When neighboring nanopores are sufficiently close, the depletion zones produced by individual pores overlap and

reduce the ionic concentration available to each nanopore.[2,75,78,96,117] The resulting current through an array can therefore be smaller than would be predicted by simply adding the currents of the constituent nanopores.

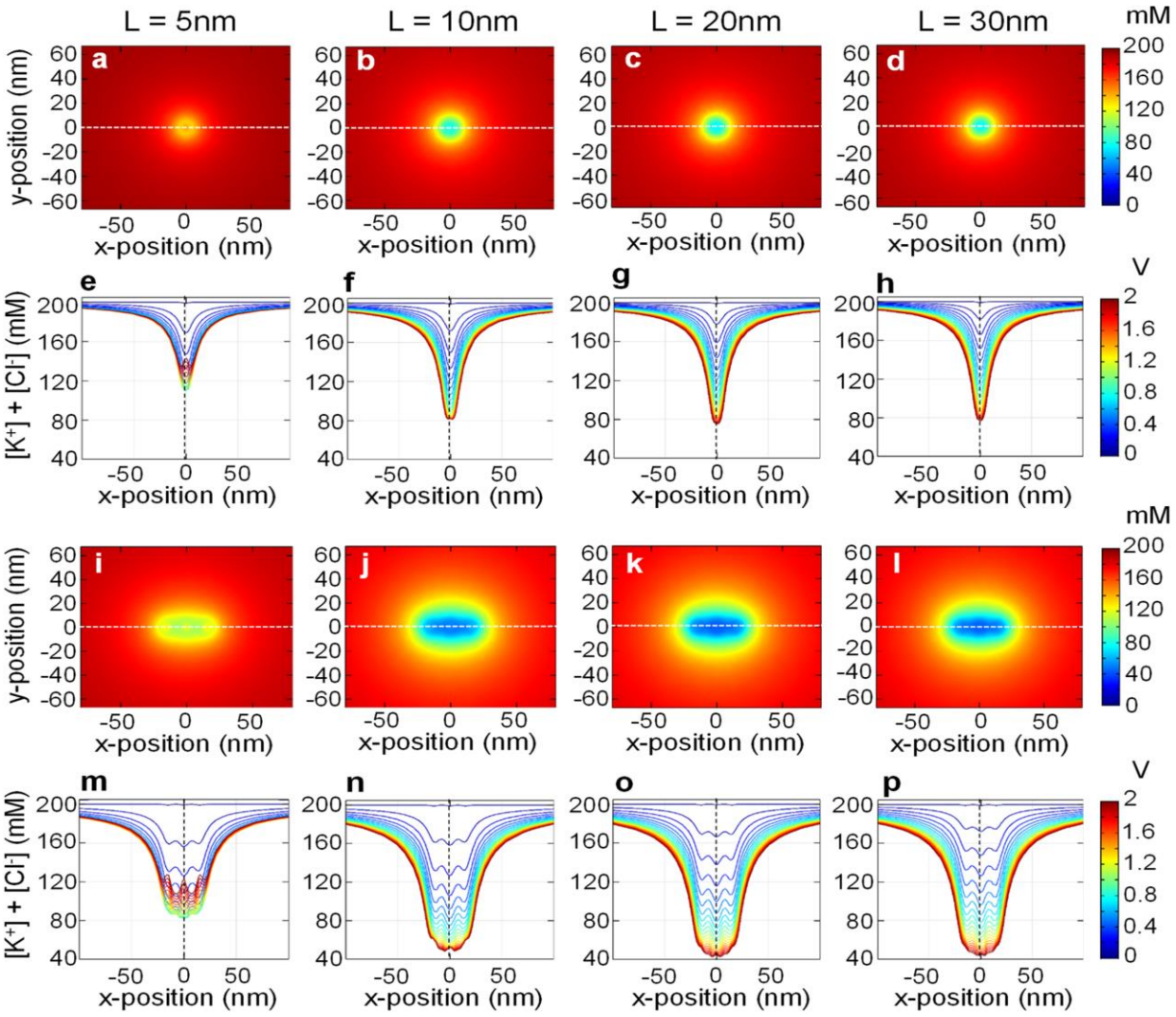

Figure 5.2 Ionic Depletion as a Function of Pore Length. Ionic depletion caused by ion concentration polarization in single nanopores (a–h) and in nanopore arrays with 3 pores (i–p) in 100 mM bulk KCl as a function of pore length and voltage. Results for 5, 10, 20, and 30 nm long pores are shown in subsequent columns from left to right. All nanopores had a surface charge density on the pore walls of −0.05 C m^{-2}. The depletion is formed on the side of the membrane

that is the source of cations, *i.e.*, the side kept at positive potential. (a–d) and (i–l) show surface heat maps, at 2 V, of the total concentration of K^+ and Cl^- at a distance 5 nm away from the membrane surface for single pores and arrays, respectively. (e–h) and (m–p) show ionic concentrations along the dashed horizontal line in the heat maps as a function of transmembrane potential between 0 V and 2 V, for single nanopores and arrays. For all arrays, an interpore spacing of 15 nm from center to center was used, with the center pore located at (0,0,0).

To examine how pore length influences this behavior, single nanopores and three-nanopore arrays containing pores with lengths of 5, 10, 20, and 30 nm were compared while maintaining a constant pore diameter of 5 nm. In the arrays, neighboring nanopores were separated by a center-to-center distance of 15 nm.[2]

The ionic concentration distributions demonstrate that ICP generates a depletion region on the side of the membrane that acts as the source of the preferred ionic species and an enrichment region on the opposite side. In three-nanopore arrays, the depletion zones generated by neighboring pores overlap substantially, producing a broader and more strongly depleted region than that observed for an isolated nanopore.[78]

Because transport through charged nanopores is influenced by the surrounding reservoirs, local ionic concentration immediately outside the nanopore provides a useful measure of the severity of ICP.[2,81,118] The total ionic concentration at the pore axis and 5 nm from the membrane surface was therefore monitored and denoted c_{dep}.

At 10 mM KCl and low applied voltages, c_{dep} was nearly independent of pore length for both individual nanopores and three-pore arrays. Only a weak decrease in concentration was observed as the nanopore length decreased. This behavior can be understood from the larger

electric field produced within shorter nanopores at the same applied voltage, which can initially promote stronger depletion.

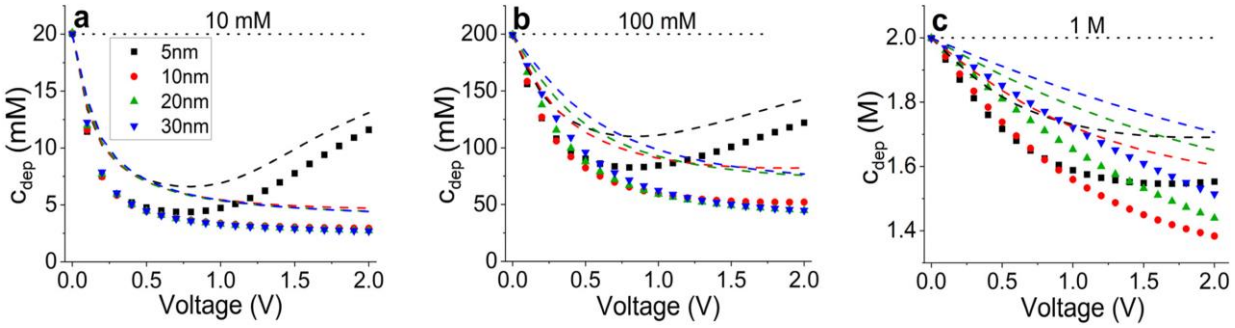

Figure 5.3 Total Ionic Concentration, c_{dep}, in the Depletion Zone. Total ionic concentration, c_{dep}, in the depletion zone just outside of single nanopores (dashed lines) and the center pore in the arrays (symbols), as a function of pore length and voltage, at (a) 10 mM, (b) 100 mM and (c) 1 M KCl. This graph shows concentrations at the pore axis at a distance of 5 nm to the membrane (vertical dashed lines shown in Figure 5.2 e-h and m-p). This concentration is treated as a measure of the degree of ionic depletion. The dotted horizontal lines show the total bulk concentration of ions.

At higher voltages, however, the behavior of the 5 nm long nanopore diverged from that of the longer pores. Above approximately 0.6 V in 10 mM KCl, cdep increased with increasing voltage for the 5 nm pore, whereas the 10–30 nm pores maintained similar and substantially depleted concentrations. This behavior indicates that sufficiently short nanopores enter a regime in which ICP becomes weaker at high voltage, consistent with a reduction in ion selectivity.[109]

Similar behavior was observed at 100 mM KCl, although the dependence on pore length became more pronounced. At low voltage, shorter nanopores again produced somewhat stronger depletion. At voltages above approximately 0.8 V, however, the 5 nm pore exhibited an increase in cdep, distinguishing its transport behavior from the longer nanopores.

At 1 M KCl, ICP was substantially weaker because electrostatic interactions associated with the nanopore surface charge were strongly screened. Nevertheless, depletion was not completely eliminated. The local concentration near the pore entrance still decreased below the bulk value, demonstrating that concentration polarization can influence ionic transport even under conditions where surface-charge effects are comparatively weak.

These results establish a nontrivial relationship among nanopore length, electrolyte concentration, and applied voltage. Importantly, they also demonstrate that the influence of ICP cannot be inferred solely from the physical nanopore length. The next consideration is how these concentration distributions translate into ionic current and nanopore conductance.

5.5 Nearly Pore-Length-Independent Ionic Conductance

Current–voltage characteristics calculated for nanopores of different lengths reveal one of the central findings of this chapter: under appropriate conditions, ionic current becomes nearly independent of nanopore length.

In 10 mM KCl, the currents through 10, 20, and 30 nm long nanopores were nearly indistinguishable. At low applied potentials, approximately −0.5 to +0.5 V, even the 5 nm long nanopore exhibited nearly the same ionic current as the longer pores. Similar behavior occurred in the three-nanopore arrays.

This result is unexpected from conventional geometrical resistance arguments. For an ideal cylindrical nanopore filled uniformly with electrolyte, the total resistance can be approximated as the sum of the geometrical pore resistance and access resistance.[2,77,91,94]

$$\Omega_{\mathrm{pore}} = \Omega_{\mathrm{geom}} + \Omega_{\mathrm{access}} \tag{5.3}$$

For a cylindrical nanopore,

$$\Omega_{\text{pore}} = \frac{1}{\kappa}\left(\frac{4L}{\pi D^2} + \frac{1}{D}\right) \tag{5.4}$$

where κ is the electrolyte conductivity, L is the nanopore length, and D is the nanopore diameter. According to this expression, increasing L while holding D constant should increase the nanopore resistance and decrease the ionic current. For a 5 nm diameter nanopore, increasing the length from 10 to 30 nm would be expected to increase the resistance by approximately a factor of 2.4. Likewise, relative to a 5 nm long nanopore, pores with lengths of 10, 20, and 30 nm would conventionally be expected to conduct substantially less current.

Current–voltage curves for single nanopores and three-pore arrays with pore lengths from 5 to 30 nm at 10 mM, 100 mM, and 1 M KCl. Charged nanopores exhibit nonlinear transport and a reduced dependence of current on pore length compared with the corresponding uncharged nanopores shown by dashed lines.

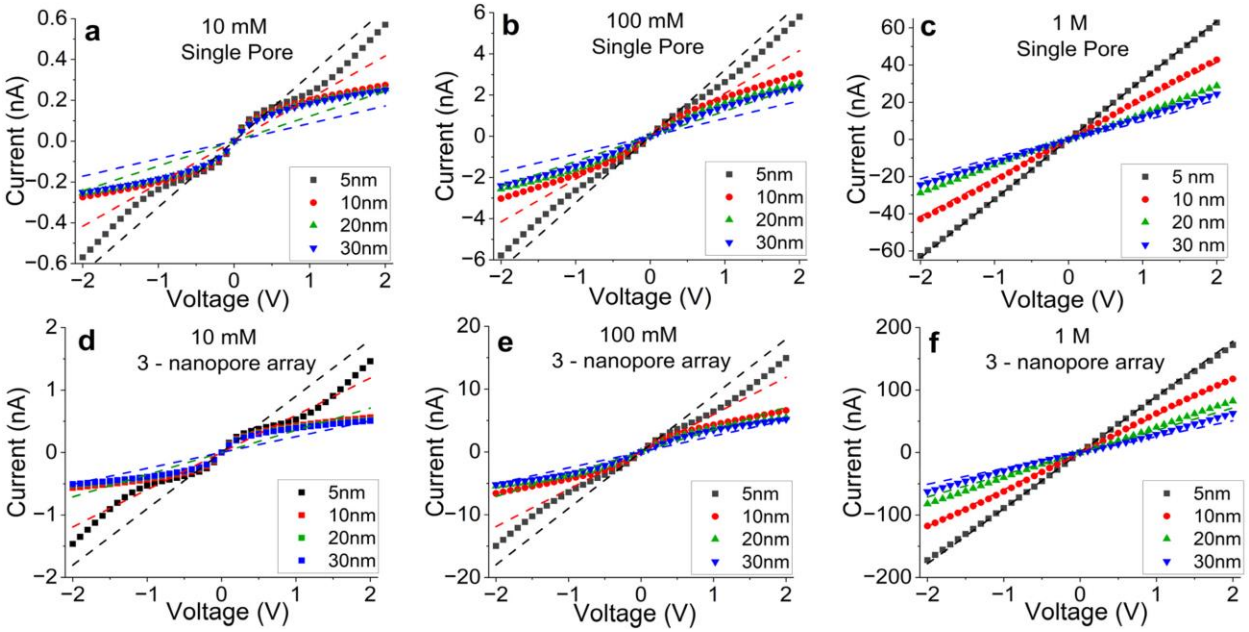

Figure 5.4 Current–voltage Curves for Single and Triple Nanopore Systems. (a–c) and 3-nanopore arrays (d–f) as a function of bulk salt concentration and pore length. Curves with

symbols were obtained for negatively charged nanopores/arrays with −0.05 C m^{-2} on the pore walls. Dashed lines represent the current–voltage curves of uncharged pores of the same length as indicated by the color in the legend. The legend indicates the pore length.

The numerical results demonstrate that this simple prediction fails at sufficiently low electrolyte concentrations. The reason is that the nanopore is not uniformly filled with electrolyte at the bulk concentration. Instead, ICP creates a spatially nonuniform conductivity distribution. The depletion region formed at the nanopore entrance extends into the pore volume.[2,119] This low-concentration region is followed by a region in which the ionic concentration can substantially exceed the bulk concentration. Consequently, different portions of the nanopore contribute very differently to the total electrical resistance.

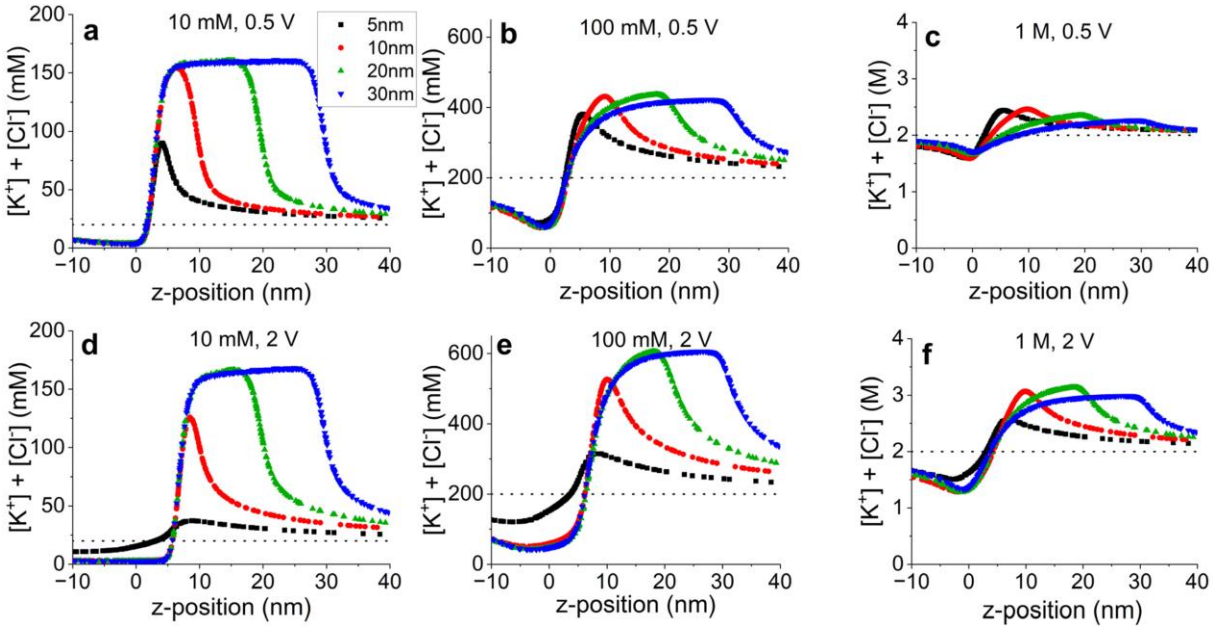

Figure 5.5 Total Ionic Concentration Along the Pore Axis. Total ionic concentration along the pore axis for the center pore in 3-nanopore arrays as a function of pore length and salt concentration at (a–c) 0.5 V and (d–f) 2 V. The blue, green, red, and black symbols indicate pores that are 30 nm, 20 nm, 10 nm, and 5 nm long. The entrance to all pores is at z = 0 nm. The

depletion zone is created at negative *z* positions where the positive voltage is applied. The dotted horizontal line shows the total bulk concentration of ions.

The depleted region possesses relatively low ionic conductivity and therefore contributes strongly to the total resistance. In contrast, the enriched portion of the nanopore can contain concentrations several times larger than the bulk concentration and contributes comparatively little resistance. Increasing the physical pore length can therefore add predominantly high-conductivity pore volume rather than proportionally increasing the electrically important resistive region.

This provides the physical origin of the nearly pore-length-independent conductance. Under conditions where the depletion regions of nanopores with different physical lengths possess similar spatial extents and ionic concentrations, those nanopores effectively possess similar resistive lengths. The remaining differences in physical length contribute comparatively little to the total system resistance.

The importance of the depletion region can be further quantified by considering the fraction of the applied transmembrane potential that drops across it. At 10 mM KCl and an applied potential of 0.5 V, approximately 90% of the total transmembrane potential drops across the depleted region. Thus, although the physical nanopore lengths vary substantially, the majority of the electrical resistance is concentrated within a similar spatial region.

At 2 V, the depletion region extends farther into the nanopore. For the 10–30 nm pores in 10 mM KCl, however, its extent and concentration remain similar among the different pore lengths, and more than 90% of the applied transmembrane potential continues to drop across this region. Consequently, these nanopores maintain nearly identical ionic currents.

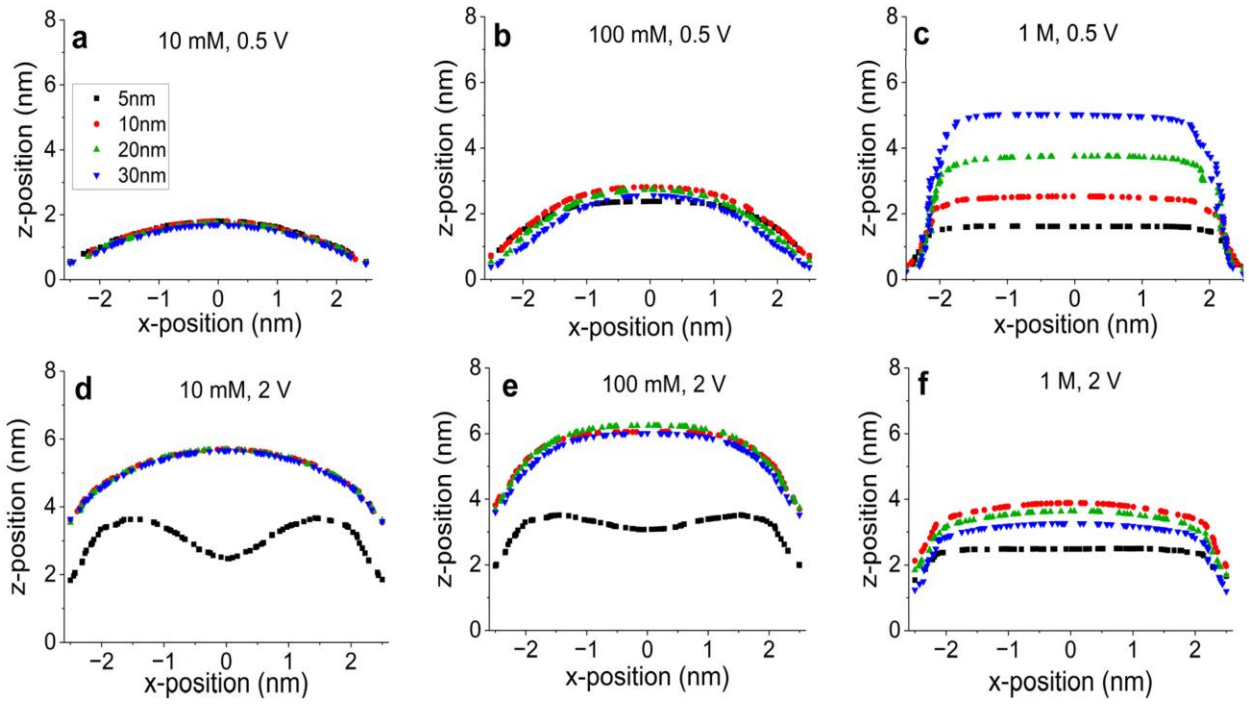

Figure 5.6 Contours of the Positions where the Total Ionic Concentration Reaches 95%. Contours of the position in the *xz*-plane inside the pore where the total ionic concentration reaches 95% of the bulk total concentration, at (a–c) 0.5 V and (d–f) 2 V. $x = 0$ nm indicates the middle of the center pore in 3-nanopore arrays of all lengths. The vertical axis indicates the position along the pore axis (*z*-direction) away from the entrance with the depletion zone.

The 5 nm long pore behaves differently at higher voltages. Its depletion region becomes less pronounced, and the ionic concentration throughout the pore approaches the bulk concentration more closely. The low-conductivity region therefore occupies a smaller effective portion of the transport pathway, producing a larger current than in the longer nanopores.

At 100 mM KCl, the same physical mechanism remains present but is less pronounced. The depleted concentration is not as low relative to bulk, while the enriched region exhibits a smaller concentration enhancement. Consequently, portions of the nanopore outside the depletion region contribute more significantly to the total resistance, and shorter nanopores exhibit somewhat larger currents.

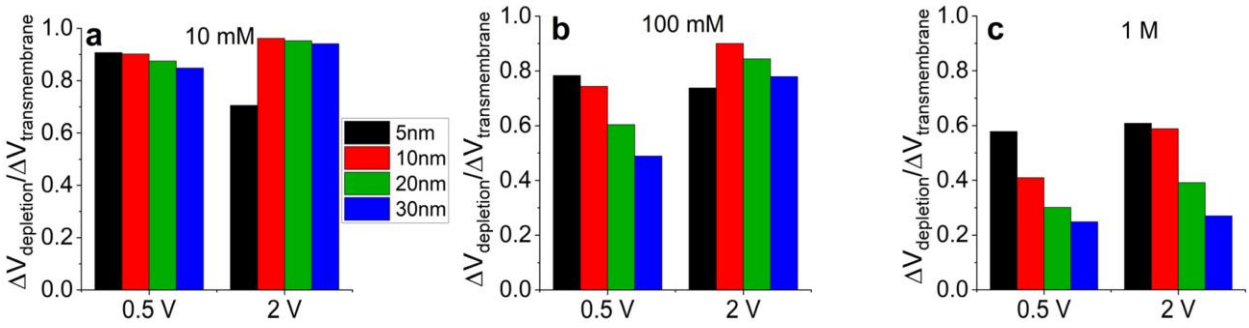

Figure 5.7 $\Delta V_{transmembrane}$ Drop over the Depletion Zone. Fraction of the transmembrane potential, $\Delta V_{transmembrane}$, that drops over the depletion zone at the pore entrance and in the pore with the voltage drop, $\Delta V_{depletion}$, at two values of transmembrane potential, 0.5 V and 2 V, in (a) 10 mM, (b) 100 mM, and (c) 1 M KCl as a function of pore length. A ratio $\Delta V_{depletion}/\Delta V_{transmembrane}$ approaching 1 indicates that the applied voltage drops predominantly over the depletion zone.

At 1 M KCl, ICP becomes sufficiently weak that the full nanopore length again contributes appreciably to the electrical resistance. The conventional relationship between pore length and conductance is therefore progressively recovered, with longer nanopores exhibiting lower conductance.

These results demonstrate that the relevant electrical length of a charged nanopore is not necessarily equal to its physical length. Under strong ICP conditions, the effective resistive length is determined primarily by the depletion region.

5.6 Relationship Between ICP and Ion Selectivity

The nearly pore-length-independent conductance observed in the simulations is intrinsically connected to ion selectivity. ICP develops because the nanopore preferentially transports one ionic species. Changes in selectivity therefore modify the magnitude of concentration polarization and, consequently, the effective resistance of the system.

Cation selectivity was quantified from the currents carried separately by K^+ and Cl^- according to[109]

$$\text{Selectivity} = \frac{I_{K^+} - I_{Cl^-}}{I_{K^+} + I_{Cl^-}} \tag{5.3}$$

At 10 mM KCl and low applied voltage, all nanopores were strongly cation selective. This behavior is consistent with the presence of substantial and nearly pore-length-independent depletion regions.

As the applied voltage increased, however, the 5 nm long nanopores became progressively less selective. The weakening of ion selectivity reduced ICP, increased the ionic concentration within the depleted region, and consequently increased the ionic current relative to the longer pores.

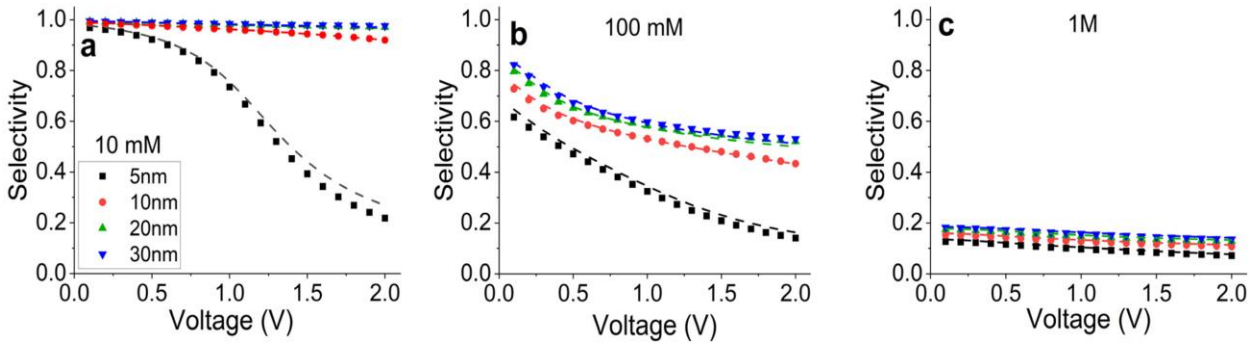

Figure 5.8 Selectivity of Nanopore Systems. Cation selectivity of single nanopores (dashed lines) and 3-nanopore arrays (symbols) as a function of pore length and voltage in (a) 10 mM, (b) 100 mM, and (c) 1 M KCl. Selectivity is calculated as the difference between the currents carried by cations and anions, divided by the total ion current (equation 4).

At 100 mM KCl, ion selectivity was lower overall than in 10 mM KCl, as expected from the stronger electrostatic screening at higher ionic strength. Nevertheless, the 10–30 nm long

nanopores maintained similar selectivities over a substantial voltage range and also exhibited similar ionic currents.

At 1 M KCl, selectivity remained below approximately 0.2 and approached zero at large applied voltages. The corresponding ICP effects were weak, and conductance therefore became much more strongly dependent on physical pore length.

These results confirm that pore-length-independent conductance is not simply a geometrical phenomenon. It results from a coupled electrochemical response in which ion selectivity produces ICP, ICP establishes a localized depletion region, and that depletion region controls the effective electrical resistance of the nanopore.

5.6 Ion Concentration Polarization and Conductance of Ionic Diodes

The preceding results considered nanopores with homogeneous negative surface charge. A second class of systems was examined to determine how the spatial pattern of surface charge modifies ICP and the relationship between pore length and conductance.

Previous work demonstrated that concentration polarization can be altered by introducing a junction between positively and negatively charged regions along the nanopore wall.[2] Nanopores containing such bipolar surface-charge distributions function as ionic diodes, producing substantially different currents for opposite voltage polarities.[63,64,100]

Current–voltage characteristics were therefore calculated for individual ionic diodes and arrays containing three diodes with a center-to-center spacing of 15 nm. The I–V curves were strongly asymmetric in 10 mM and 100 mM KCl, particularly for diodes with lengths between 10 and 30 nm.[64]

As observed for homogeneously charged nanopores, the current–voltage curves for 10–30 nm long ionic diodes in 10 mM KCl were nearly identical over a substantial voltage range. The 5 nm long diode exhibited similar current to the longer pores for the high-conductance voltage polarity but increasingly lost rectification at larger voltages of the opposite polarity.

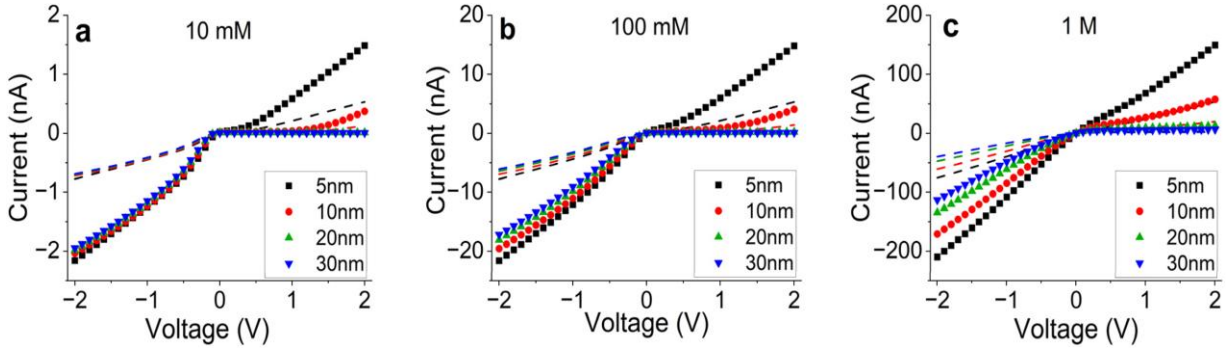

Figure 5.9 Current–Voltage Curves through Nanopore Diodes. Current–voltage curves through single nanopores (dashed lines) and arrays (symbols) that function as ionic diodes. The dependence on pore length and bulk salt concentration is shown: (a) 10 mM, (b) 100 mM, and (c) 1 M. The pores have a junction between two zones with opposite surface charges.

The concentration distributions reveal an important distinction between ionic diodes and homogeneously charged nanopores. For uniformly negatively charged pores, a substantial depletion region forms at the external nanopore entrance and extends into the pore. For ionic diodes, in contrast, the pore entrances remain in contact with electrolyte at approximately the bulk concentration. The strongest ion enrichment or depletion instead develops inside the nanopore near the junction between the oppositely charged regions.

For the high-conductance state of the diode, the transmembrane voltage produces substantial ionic enrichment within the nanopore. The magnitude of this enrichment increases with pore length. Consequently, the increase in geometrical resistance associated with a longer

nanopore can be offset by the decrease in resistance produced by the larger ionic concentration inside the channel.

At low voltage in 10 mM KCl, this balance is sufficiently strong that diodes with substantially different physical lengths can conduct approximately the same current. Thus, pore-length-independent conductance occurs in both uniformly charged nanopores and ionic diodes, although the underlying spatial distributions of ionic concentration differ.

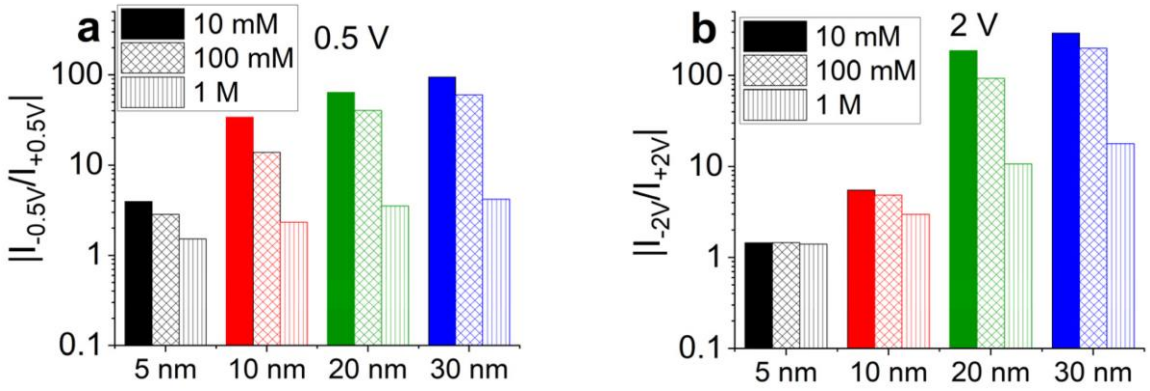

Figure 5.10 Rectification degrees of 3-nanopore arrays containing ionic diodes. Rectification degrees of 3-nanopore arrays containing ionic diodes, calculated based on the *I–V* curves shown in Fig. 9 as ratios of currents at (a) −/+ 0.5 V, and (b) −/+ 2 V. Rectification for diodes that are 5 nm, 10 nm, 20 nm, and 30 nm long is shown.

For the opposite voltage polarity, a depletion region develops inside the ionic diode. The extent of this depletion controls the low-conductance state and produces ion current rectification. Very short, 5 nm long diodes progressively lose selectivity at high voltages, weakening the depletion state and reducing their rectification.

These results demonstrate that the spatial distribution of surface charge provides an additional means of controlling where ICP occurs. Rather than allowing depletion to dominate

transport at the external pore entrance, bipolar charge patterns can shift the principal enrichment and depletion regions into the nanopore interior.

5.7 Conclusions

The results presented in this chapter demonstrate that ionic transport through charged nanopores can be strongly influenced by ion concentration polarization, which modifies ionic concentrations not only in the reservoirs near the nanopore entrances but also throughout a significant portion of the pore volume.

This effect becomes particularly important for low-aspect-ratio nanopores, where an ICP-induced depletion region can occupy a substantial fraction of the nanopore. Under these conditions, the electrical resistance of the system is dominated by the depleted region rather than by the full physical length of the pore. Consequently, nanopores with substantially different lengths can exhibit nearly identical ionic conductances.

For negatively charged nanopores in low electrolyte concentrations, 10–30 nm long pores displayed nearly identical ionic currents over broad voltage ranges. At sufficiently low voltages, even 5 nm long nanopores exhibited similar conductance. Analysis of the ionic concentration and electric-potential distributions demonstrated that the majority of the applied transmembrane potential drops across the depletion region, while the remaining portion of the nanopore contains enhanced ionic concentrations and contributes comparatively little resistance.

The results therefore suggest that increasing membrane thickness does not necessarily produce a proportional increase in nanopore resistance. Instead, there exists a range of geometrical and electrochemical conditions for which nanopores several times different in physical length can possess similar effective resistive lengths.

The range of pore lengths exhibiting nearly identical conductance was observed for both individual nanopores and three-nanopore arrays, although the effect was more pronounced in arrays because overlapping depletion zones enhance ICP-induced transport limitations.

Ion selectivity was shown to play a central role in establishing this behavior. At low electrolyte concentrations and low voltages, the nanopores remained strongly cation selective and produced pronounced ICP. Very short nanopores progressively lost ion selectivity as the applied voltage increased, weakening concentration polarization and increasing their conductance relative to longer nanopores. At high electrolyte concentrations, surface-charge effects were strongly screened, selectivity decreased, ICP weakened, and the conventional dependence of resistance on physical pore length was progressively restored.

Finally, simulations of ionic diodes demonstrated that the location of concentration polarization can be manipulated through spatial patterning of nanopore surface charge. In bipolar nanopores, the strongest ion depletion and enrichment occur within the nanopore near the junction between oppositely charged regions, while both nanopore entrances remain in contact with electrolyte at approximately the bulk concentration. This redistribution of ICP allows even very short nanopores to retain rectification at sufficiently low voltages.

Collectively, these results demonstrate that nanopore conductance cannot always be predicted from geometry and bulk electrolyte conductivity alone. The effective electrical resistance instead emerges from the coupled effects of nanopore geometry, surface charge, ion selectivity, electrolyte concentration, applied voltage, and ion concentration polarization. These findings provide important design considerations for selective separation membranes, nanopore arrays, ionic circuitry, and membranes intended for osmotic energy conversion

CHAPTER 6 Electrostatic Control of Ionic Transport in Small Nanopore Arrays

Solid-state nanopores have emerged as versatile platforms for studying ionic transport under nanoconfinement[1-4] and enabling applications in molecular sensing,[5-10] separations,[11-14] and energy conversion. [15, 16] In recent years, nanopores have also been explored as building blocks for biomimetic ionic systems in which transport phenomena such as selectivity, gating, and rectification can be engineered to emulate the functionality of biological ion channels.[2, 17-22] A central challenge in this field is achieving dynamic and spatially localized control over ionic transport, particularly in systems where multiple nanopores interact and exhibit collective transport behavior.[23-25]

Ionic transport in nanopores is governed by surface-dominated electrostatics, where the electrical double layer (EDL) and ion surface interactions dictate ionic distributions and conductance.[1] Under an applied transmembrane potential, these effects give rise to ionic concentration polarization (ICP), producing ion depletion and enrichment regions near pore entrances. If the nanopore systems exhibit broken symmetry in electrochemical potential, this will generate ionic current rectification (ICR),[23, 24, 26, 27] enabling nanopores to function as ionic diodes and iontronic circuit elements.[18, 28-39] Surface functionalization has consequently played a central role in tailoring nanopore transport behavior. Chemical modification of pore walls enables control over surface charge density, ion selectivity, and interfacial electrostatics within the EDL. However, such approaches are typically static and do not readily permit dynamic tuning of ionic transport in real time. More recent efforts have therefore focused on externally controlled electrostatic environments through electric gating potentials,[40-46] and preparation of

nanopores whose transport would be gated by other external stimuli including pH,[19, 29, 47] light,[48] voltage,[2, 18, 47] temperature[49-52] and molecules.[53, 54]

Metallic interfaces, and in particular gold, provide a promising route toward dynamically tunable ionic transport. Gold is widely utilized in nanofabrication because of its chemical stability, high electrical conductivity, and compatibility with nanoscale deposition and patterning techniques. In nanopore systems, gold has been employed for sensing, electrode integration, and electrostatic modulation of local ionic environments.[40, 55, 56] Notably, conductive surfaces support multiple electrostatic boundary conditions, including floating potentials, externally biased states, and effective surface charge distributions, providing a versatile platform for tuning local electric fields.

Previous work demonstrated that a thin gold layer positioned at the entrance of a nanopore can induce ionic current rectification through electrostatic polarization of the metallic surface, even in geometrically symmetric systems.[57] Polarization of metallic surface inside a nanopore also led to the formation of a wireless sensor, because according to the concept of a bipolar electrode, a metallic surface placed in electric field can function as an anode on end and cathode on the other.[58-61] More broadly, recent studies have shown that nanopore systems can exhibit collective transport behavior in which ionic concentration polarization mediates interactions between neighboring pores and these interactions can be tuned by functionality of the pores.[24, 62] These findings suggest that local electrostatic environments may be leveraged to create dynamically tunable iontronic systems.

Despite these advances, the role of a neighboring conductive surface positioned near, but not directly on, a nanopore remains largely unexplored. Unlike direct surface functionalization, such a geometry introduces a non-contact electrostatic coupling mechanism in which ionic

transport is modulated through polarization of the neighboring metallic surface. When a conductive surface such as gold is positioned near a nanopore, it polarizes in response to the applied transmembrane potential, producing spatially varying electric fields and modifying ionic concentration profiles near the pore entrance. Because ICP in solution is highly sensitive to local electrostatic conditions, even modest induced polarization can significantly alter depletion regions and transport properties.

Here, using finite element methods we investigate the influence of a neighboring gold surface on ionic transport in single-pore and small nanopore array systems. Using finite element simulations, we demonstrate that electrostatic polarization of the neighboring metallic surface provides a robust and tunable mechanism for controlling ICP and current–voltage behavior without direct pore functionalization or electrically addressing the Au layer. These results establish non-contact electrostatic coupling as a simple strategy for inducing and tuning ionic rectification and provide insight into the design of dynamically controllable nanofluidic and iontronic devices. The floating electrode boundary condition is compared to two additional cases. In the first case, the Au surface was rendered negatively charged without considering its conductive properties. We also modeled an electrically addressable Au layer with gate potentials that were lower and higher than the transmembrane potential. The results show that placing a gold layer in proximity to nanopores can induce a wealth of different transport properties.

6.1 COMSOL Simulations

Three-dimensional finite element models were employed because the neighboring surface geometry breaks axial symmetry. Simulations were performed using COMSOL Multiphysics by coupling electrostatics with the transport of diluted species module. Inclusion of the Navier–

Stokes equations produced negligible changes in ionic transport behavior while substantially increasing convergence times and was therefore omitted. The model additionally neglects specific ion adsorption to either the nanopore walls or the neighboring metallic surface.

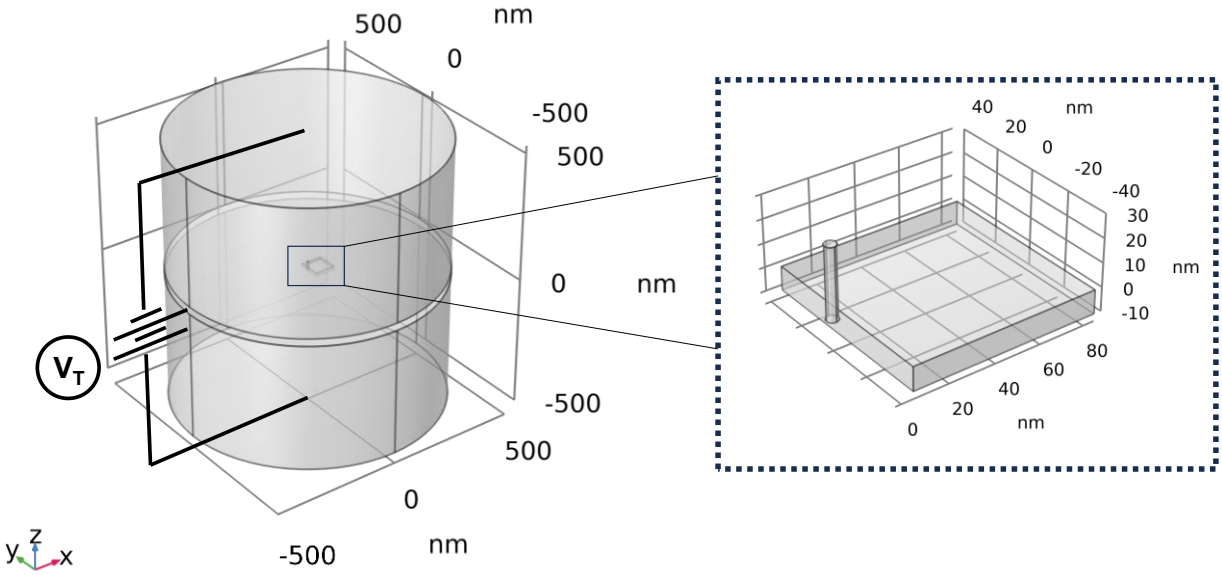

Figure 6.1 Schematic of the COMSOL Multiphysics simulation geometry. The model consists of cylindrical reservoirs connected by one or more nanopores positioned adjacent to a 10 nm tall neighboring conductive surface. The locations of the applied transmembrane potential and ground boundary conditions are indicated.

The basic structure of all models consisted of either a single cylindrical nanopore or a two- or three-pore nanopore array embedded between two cylindrical reservoirs, each with a radius and height of 0.5 μm. Individual nanopores had openings of 5 nm in diameter, and lengths of 30 nm. For nanopore arrays, the pore-to-pore distance was defined as the center-to-center separation between adjacent nanopores and was treated as a variable parameter throughout this work.

A transmembrane potential sweep ranging from −2 to +2 V was applied in increments of 0.2 V and, in selected cases, 0.1 V. Electrolyte bulk concentrations of 1 mM, 10 mM, 100 mM, and 1 M KCl were considered using diffusion coefficients of 2×10^{-9} m^2 s^{-1} for both ionic species. Homogeneously charged nanopores with surface charge densities of −0.05 C/m^2 were modeled adjacent to a neighboring conductive surface with dimensions of 80 (length) × 80 (width) × 10 (height) nm.

Three electrostatic boundary conditions were considered for the neighboring surface: floating potential, control, fixed surface charge density, and externally applied voltage. The floating potential condition consisted of an electrically floating boundary initialized with zero charge and zero potential. In control models, no electrostatic boundary condition was applied to the neighboring surface. Models with externally applied voltage utilized surface potentials ranging from −1 to +1 V, while models with fixed surface charge employed charge densities equal to those of the nanopore surface.

6.2 Results and Discussion

This chapter focuses on the possibility of gating ionic transport by a metallic 10 nm high layer positioned in proximity to the pore opening (Figures 6.1, 6.2). We will begin the analysis with the distance between the edge of the Au layer and the pore center of 5 nm. The diameter and length of the pore were 5 nm and 30 nm, respectively. To investigate how a neighboring conductive surface influences ionic transport and ion concentration polarization (ICP), we considered several electrostatic boundary conditions that may arise in experimentally realizable metallic nanostructures. Specifically, a conductive surface positioned near a nanopore may behave as an

electrically floating interface, an externally gated surface, or an effectively charged boundary, each of which modifies the surrounding electrostatic environment in distinct ways.

6.3 Au as a Polarizable Floating Electrode

Applying a floating potential boundary condition to the neighboring conductive surface produces a dynamically induced polarization that substantially modifies ionic concentration polarization near the nanopore entrance, and consequently current-voltage curves. Figure 6.2 compares current through a nanopore located next to a floating conductive layer with corresponding control models in which the neighboring geometry is retained but no electrostatic boundary condition is applied.

Even in the absence of electrostatic polarization, introduction of the neighboring surface generates weak rectification through asymmetric geometric confinement near the pore entrance. The physical presence of the neighboring structure excludes volume that would otherwise be accessible to ions. The effects of the layer are significant for positive transmembrane potentials that lead to the formation of a depletion zone on the side of the membrane with the Au layer. Consequently, positive currents are suppressed leading to rectification quantified as a ratio of currents (ICR) at -2 V and +2 V, equal to 1.1, 1.1, and 1.2 at electrolyte concentrations of 1 mM, 10 mM, and 100 mM, respectively.

When a floating potential boundary condition is applied, this geometric asymmetry is amplified through electrostatic coupling between the conductive surface and the surrounding region affected by the ion concentration polarization in the solution. Under positive transmembrane bias, the presence of the depletion zone at the pore entrance causes a significant potential drop in this region that as we hypothesize will affect polarization of the Au layer, and

local ionic concentrations (Figure 6.2a). For voltages of the opposite polarity, the metallic layer will be in contact with a zone containing enhanced ionic concentrations where the electric potential drop is minimal (Figure 6.2b). We expect therefore that negative currents will be similar in the two models, with polarizable Au and the control system.

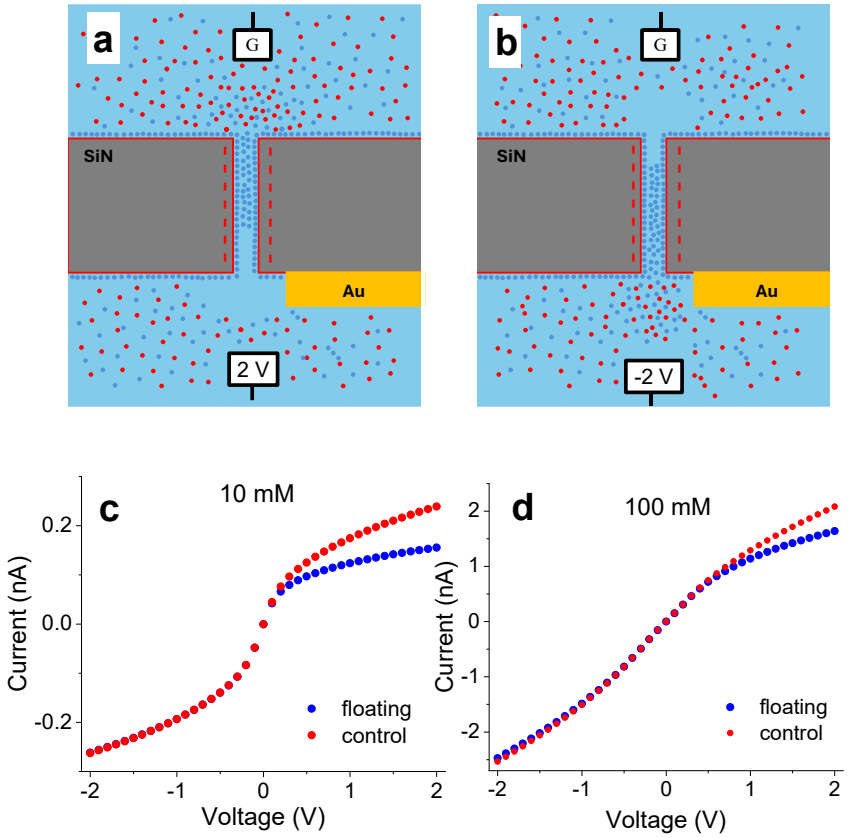

Figure 6.2 Gating of ion transport by a neighboring metallic layer. Schematic illustrating a nanopore positioned next to a metallic (e.g. Au) layer with dimensions of 80 nm x 80 nm x 10 nm. The nanopore dimensions are 5 nm in diameter, and 30 nm in length. The pore walls carry surface charge of -50 mC/m^2. (a) Electrode configuration in which the ionic depletion region forms on the same side as the gold surface. (b) Electrode configuration in which the ionic enrichment region forms adjacent to the gold surface. (c, d) Current-voltage (I–V) curves in 10

mM, and 100 mM, respectively comparing models where the Au layer functioned as a floating electrode (blue data points) and with Au being a geometric barrier without surface charge (red data points). The distance between the Au layer and the pore center was 5 nm.

Panels c–d of Figure 6.2 show that the floating potential models indeed exhibit substantially stronger rectification than the corresponding controls systems. The stronger rectification with a floating metal surface is caused by a more significant suppression of positive current, leading to ICR values of 1.9, 1.7, and 1.5 at 1 mM, 10 mM, and 100 mM KCl, respectively. These results demonstrate that geometric confinement alone produces only weak transport asymmetry, while electrostatic polarization of the neighboring conductive surface provides the dominant contribution to rectification enhancement. The magnitude of this effect decreases with increasing electrolyte concentration, consistent with enhanced electrostatic screening at higher ionic strengths. At +2 V, the percent suppression of ionic current between the floating and control systems decreased from approximately 45% at 1 mM to 22% at 100 mM, indicating that induced surface polarization becomes progressively screened as the Debye length decreases. Collectively, these results demonstrate that neighboring conductive surfaces dynamically regulate ionic transport primarily through modulation of ionic concentration polarization rather than direct electrostatic gating of the nanopore interior.

To better understand the mechanism responsible for ion current rectification induced by the polarizable Au surface, ionic concentration heat maps and concentration line profiles were generated at transmembrane potentials of ±2 V and compared with corresponding controls systems. Figures 6.3 and 6.4 show details of concentration distribution for potassium and chloride ions, respectively, focusing on heat maps and concentration profiles along the z-axis. Initially, based on the previous work of a nanopore containing a zone with Au,[57] we

hypothesized that the floating conductive surface would develop strongly heterogeneous local surface potentials near the nanopore entrance, producing nanoscale regions of opposing effective charge and asymmetric electric double layer structures along the metallic interface. Such localized polarization was expected to generate preferential ion enrichment and depletion near the pore entrance and thereby drive ionic current rectification.

However, the simulation results revealed that rather than producing highly localized regions of opposing surface potential, at positive voltages the floating conductive surface developed a comparatively homogeneous polarization distribution with depleted concentration of potassium ions next to the metallic surface (Figure 6.3a). Interestingly, the line profiles for K^+ along the z-axis revealed only small differences between the floating potential and control models, occurring mostly in the pore between z = 5 nm and z = 10 nm (Figure 6.3c). Concentrations profiles in the z-axis for Cl^- ions, on the other hand, revealed larger differences. For the floating potential boundary conditions the concentration was less diminished at the pore entrance but decreased in the pore volume compared to the control models, suggesting that the presence of the floating metallic surface made the nanopore more cation selective (Figure 6.4 a, c). As expected, at -2 V, concentrations of both ions are not affected by the presence of the metallic surface (Figure 6.3 d-f, Figure 6.4 d-f), in agreement with nearly identical currents for the control and floating Au models (Figure 6.2).

Due to the broken symmetry of the system through the presence of the Au layer, we also looked at the distribution of ionic concentrations in the direction of x-axis that is parallel to the membrane surface. At +2 V, the metal is equipotential at +2 V, and consequently, the biggest difference in K^+ and Cl^- concentrations occurred at the metallic surface. The distributions of both ions and electric potential are asymmetric with respect to the pore center (x = 0 nm), such that

e.g. K^+ concentration in the pore area further away from (closer to) the metallic surface is higher (lower) compared to the control system when the metallic surface acted as an uncharged geometric structure.

Figure 6.5 shows ionic distributions along the x-axis for three z-positions that revealed the degree of modulation of ionic concentrations is the strongest closest to the membrane surface and pore entrance. We believe the different degrees of ionic modulation along the x- and z-axes occur in response to the electrolyte potential distribution generated by the potential difference between the pore entrance and the conductive surface. Because significant portion of the voltage drop occurs across the depletion region located at the pore entrance and inside the nanopore, the local electrolyte potential near the pore entrance differs from the applied transmembrane potential. The floating conductive surface responds to this nonuniform potential distribution through charge redistribution, resulting in the accumulation of coions near the neighboring interface and the formation of a dynamic electric double layer whose strength is governed by the bulk ionic concentration. As a result, the induced electric double layer further suppresses counterion concentrations within the depletion region, thereby enhancing transport asymmetry and amplifying ionic current rectification. This suppression arises because coion accumulation within the depletion region displaces counterions that would otherwise contribute to ionic transport. The resulting reduction in the local counterion concentration decreases the number of charge carriers available for conduction, leading to further suppression of the ionic current under positive applied potentials. Importantly, polarization of the Au layer on the membrane surface would not occur in the absence of voltage induced ionic concentration polarization (ICP) in the solution. To further support the claim that ICP enables Au polarization, we looked at the

potential distribution along the membrane surface at -2 V, and indeed no significant accumulation of ions next to Au was observed, and the potential was homogeneous.

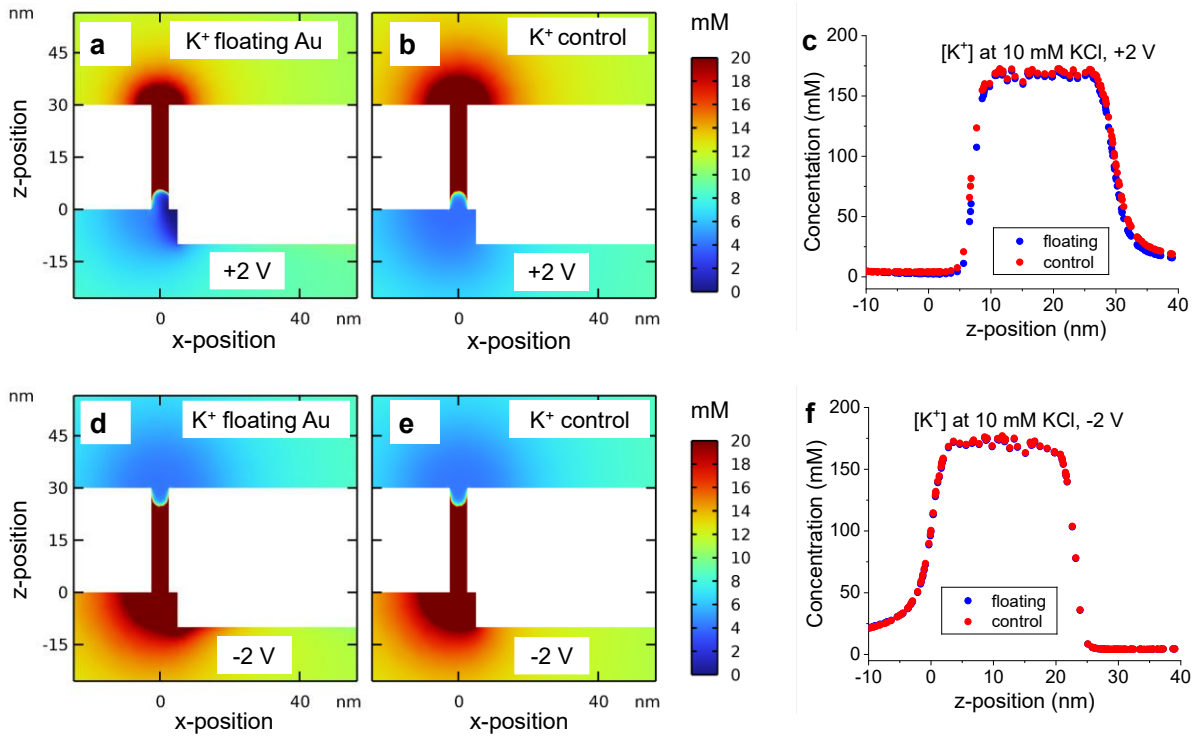

Figure 6.3 Concentration Profiles for [K^+]. Profiles of K^+ ions concentrations used to examine the electrostatic coupling between the metallic surface and the ionic enrichment and depletion regions in the solution, in 10 mM KCl in the bulk. (a - c) Heat maps and axial distribution of K^+ concentration at + 2 V. (d- f) Heat maps and axial distribution of K^+ concentration at - 2 V. Panels a and d (b and e) contain heat maps with floating potential (control boundary) condition. Panels (c) and (f) show corresponding potassium ion concentration line profiles extracted along the dashed line in panels a, b, d, and e.

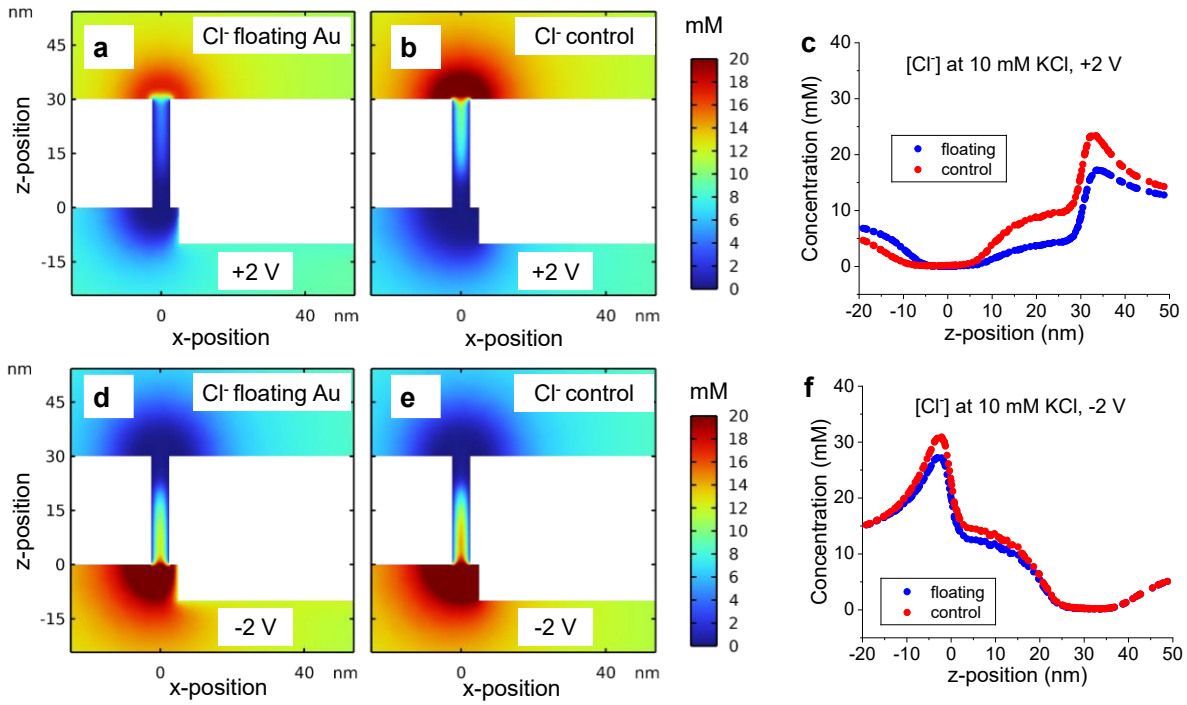

Figure 6.4 Concentration Profiles for [Cl^-]. Distributions of [Cl^-] concentrations when Au was functioning as floating electrode or a control geometric surface without surface charge in 10 mM KCl in bulk. (a – c) Heat maps and axial profile at + 2 V. (d – f) Heat maps and axial profile at -2 V. Panels a and d (b and e) contain heat maps with floating potential (control boundary) condition. Panels (c) and (f) show corresponding chloride ion concentration line profiles extracted along the vertical pore axis in panels a, b, d, and e.

Potential distribution analysis further supports the interpretation that induced polarization of the neighboring conductive surface governs the observed enhancement in ionic current rectification (Figure 6.5 h-i). Because the floating potential boundary condition enforces equipotential behavior across the conductive interface, charge must dynamically redistribute in response to the highly nonuniform electrolyte potential generated near the nanopore entrance.

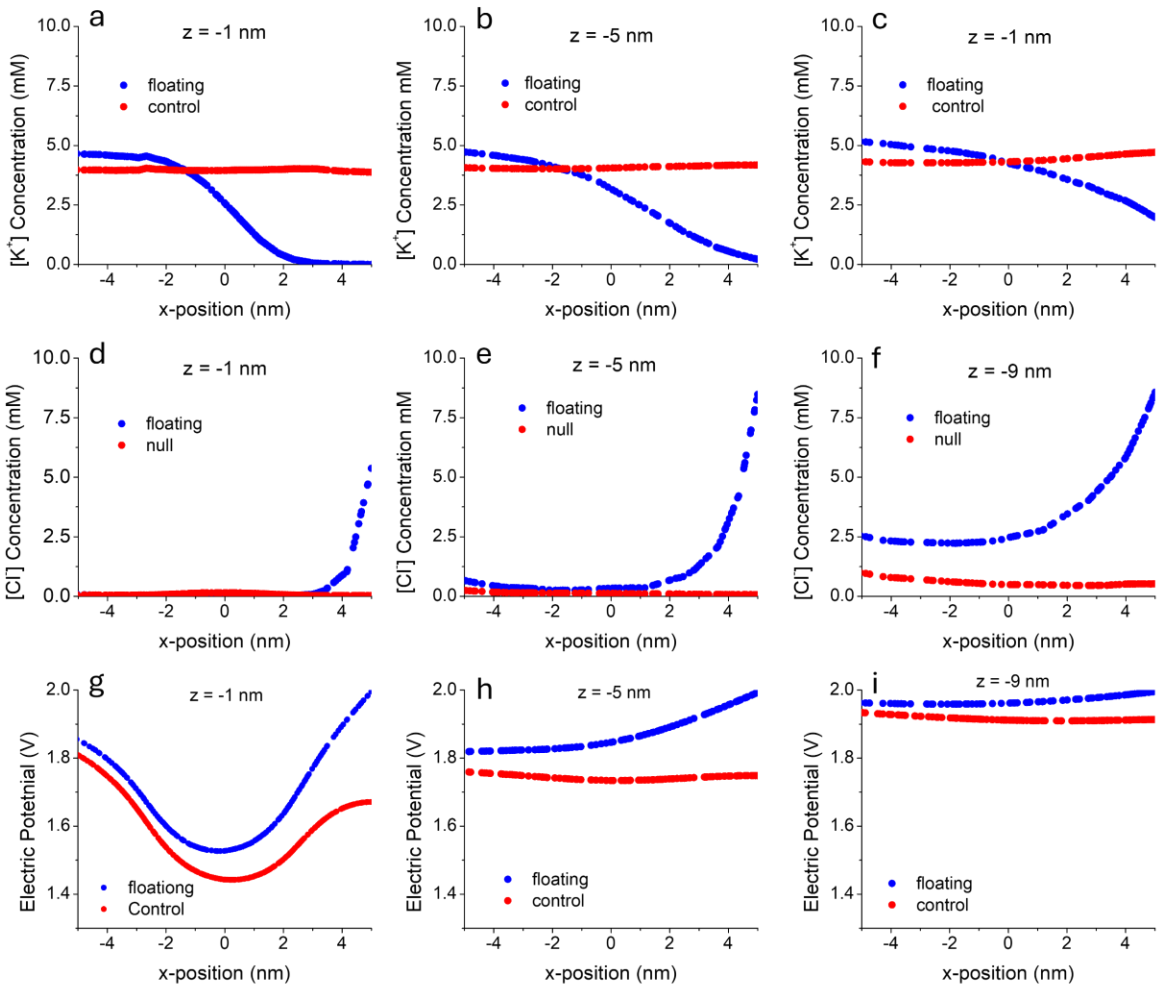

Figure 6.5 Profiles of ionic concentrations and electric potential in the direction of x-axis parallel to the membrane surface. (a – c) and (d – f) Concentration profiles of K^+ and Cl^- ions where position of x = 0 nm is the pore center and the position of x = 5 nm is the edge of the Au layer. (g – i) Profiles of electric potential. Blue points show results for the Au layer functioning as a floating electrode, while red points correspond to control models. (a, d, g) Profiles at z = -1 nm. (b, e, h) Profiles at z = -5 nm. (c, f, i) Profiles at z = -9 nm.

Figure 6.5 g shows that under a +2 V transmembrane bias, the local electrolyte potential along a line parallel to the membrane surface located at z = - 1 nm, has a minimum at ~1.5 V, producing a local potential difference of approximately 0.5 V between the conductive surface

and the adjacent electrolyte. This potential difference drives accumulation of coions near the neighboring conductive surface, resulting in formation of an induced electric double layer coupled directly to the depletion region outside the nanopore.

6.4 Surface Charge as a Boundary Condition on the Metallic Surface

In contrast to the floating potential boundary condition, introducing a fixed negative surface charge density on the neighboring surface, equal in magnitude to that of the nanopore, reverses the ionic current rectification behavior, compared to the floating potential boundary condition (Figures 6.2, 6.6). The negatively charged surface electrostatically attracts counterions toward the nanopore entrance, substantially increasing the local counterion concentration over the entire range of applied transmembrane potentials. Consequently, the depletion region that normally develops near the pore entrance under positive bias is significantly suppressed and, under sufficiently strong pore–surface coupling, can be effectively eliminated (Figure 6.6).

The suppression of the depletion region formed at the pore entrance with the boundary condition of surface charge set on Au fundamentally alters the transport-limiting mechanism of the single nanopore and creates an ionic diode. Rather than restricting the supply of charge carriers to the nanopore entrance, the neighboring surface continuously replenishes the local counterion population, maintaining a highly conductive transport pathway through the channel. As a result, ionic transport is enhanced under bias conditions that would otherwise be limited by concentration polarization in the floating potential configuration (Figures 6.2-4). These results demonstrate that the electrostatic boundary condition imposed on the neighboring surface governs whether pore–surface coupling suppresses or enhances ionic transport.

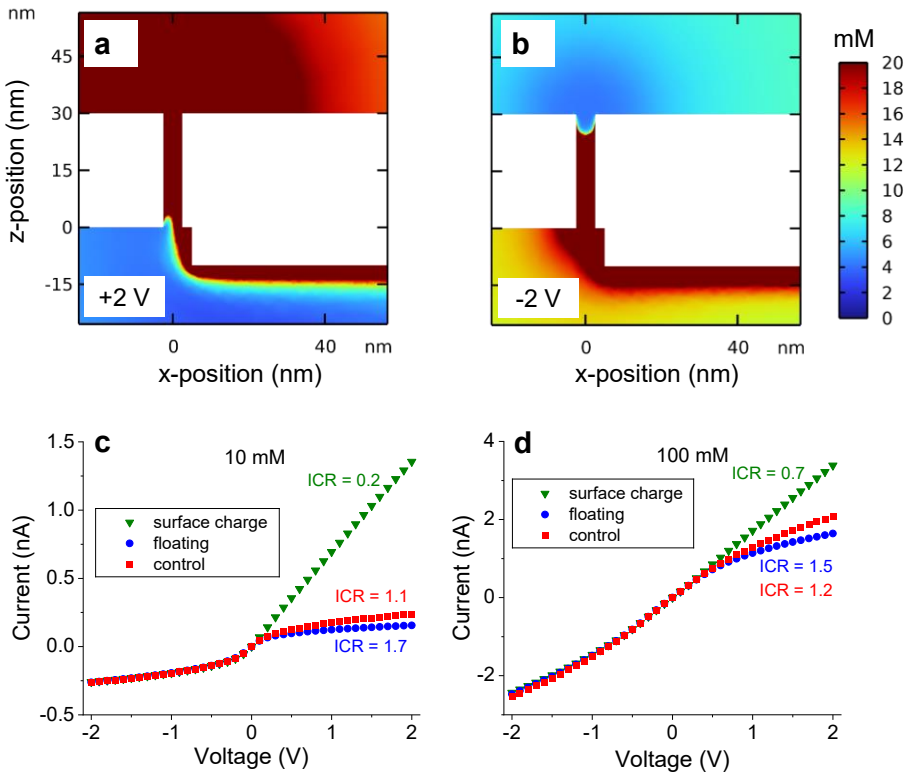

Figure 6.6 Heat maps of ionic concentrations and rectification with the boundary condition of Au layer set as surface charge density of -0.05 C/m^2. (a, b) Heat maps of total ionic concentrations at the pore entrances and in the pore for 10 mM bulk KCl concentrations when the surface charge density of -0.05 C/m^2 was applied as a boundary condition to the neighboring geometric surface at (a) +2 V and (b) −2 V, respectively. Note the formation of asymmetric enrichment regions near the nanopore entrance under opposite bias polarities. Panels (c–d) present corresponding current–voltage curves comparing the control (red points), floating potential (blue points), and surface charge (green points) model boundary conditions, highlighting the influence of neighboring surface polarization and surface charge effects on ionic transport and current rectification behavior.

The corresponding current–voltage (I-V) curves reflect the counterions accumulation for positive voltages leading to current enhancement, and reversed ionic current rectification (ICR) that becomes significantly less than unity for the 1 mM, 10 mM, and 100 mM models. This reversal in rectification compared to the floating potential model behavior occurs primarily because the neighboring charged surface provides a substantially larger reservoir of counterions available for transport through the nanopore, while simultaneously suppressing or eliminating the depletion region that would otherwise limit ionic transport. Note that this boundary condition on Au did not affect the currents for negative voltages that remain the same for the control, floating potential and surface charge boundary conditions.

6.5 Au as an Electrically Addressable Gate

Unlike a fixed surface charge, the electrostatic influence of an applied gate potential evolves with the local electrolyte potential surrounding the nanopore. Consequently, the transport behavior is governed not by the applied gate voltage alone, but by the potential difference between the gate electrode and the local electrostatic potential at the nanopore entrance.

When the applied gate potential is positive and comparable to or greater than the transmembrane potential, the potential difference between the gate electrode and the nanopore entrance remains small (Figure 6.7a, b). Under these conditions, the neighboring surface perturbs the local electric field only weakly, producing behavior analogous to that of a floating conductor. The induced surface charge promotes modest coion accumulation adjacent to the neighboring surface, reducing the local counterion concentration available for transport while preserving the ion-depleted region near the nanopore entrance. Consequently, ionic transport remains depletion-

dominated, resulting in suppressed ionic current under positive transmembrane bias and ionic current rectification ratios greater than unity.

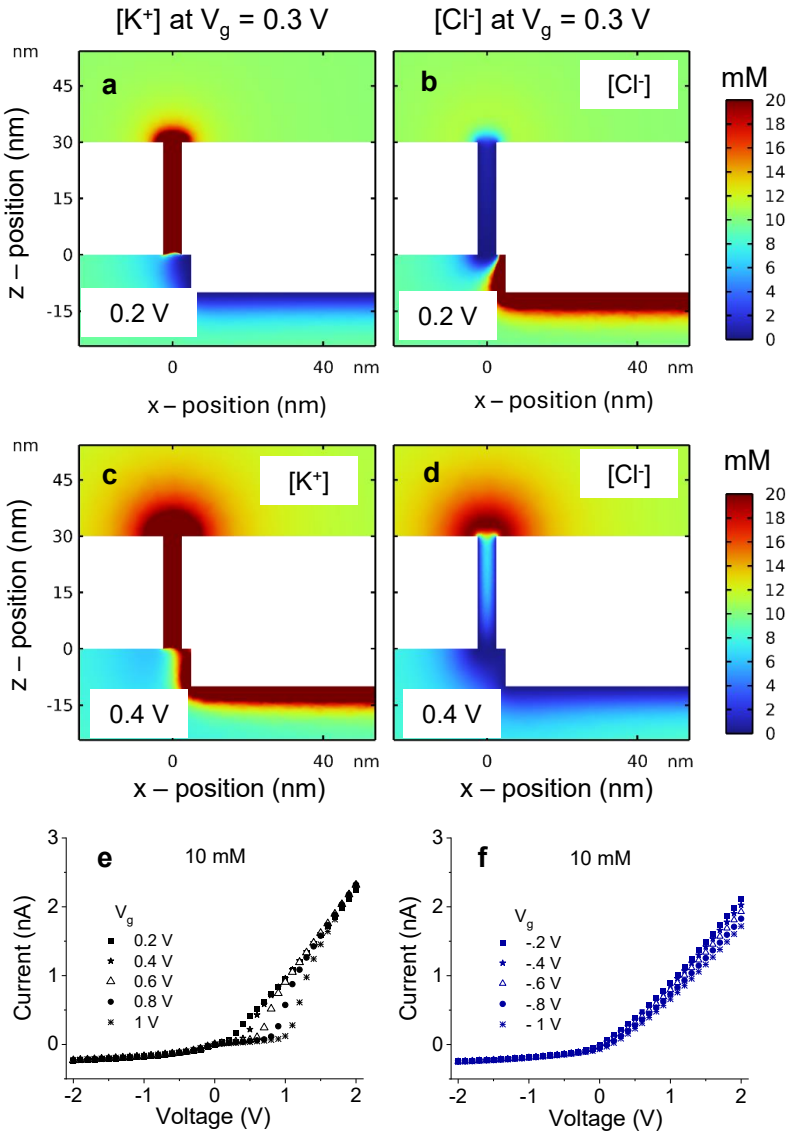

Figure 6.7 Gating of ion current through a nanopore placed in proximity to a gated metallic surface. (a – d) Heat maps of K^+ (a, c) and Cl^- (b, d) ions at the transmembrane potential of 0.3 V with gated voltage applied to the Au layer of +0.2 V (a, b) and +0.4 V (c, d).

As the transmembrane potential exceeds the applied gate potential, the potential difference between the gate electrode and the nanopore entrance becomes increasingly negative. The neighboring surface therefore undergoes a progressive redistribution of charge, strengthening the electrostatic attraction of counterions toward the pore entrance (Figure 6.7 c, d). The resulting counterion enrichment increasingly compensates for concentration polarization, reducing the extent of the depletion region and enhancing the local ionic conductivity. Consequently, the ionic current increases as the transport mechanism continuously evolves from floating-potential behavior toward that characteristic of a fixed negatively charged surface. Unlike chemically functionalized nanopores, whose transport characteristics are permanently defined by surface chemistry, electrostatic gating enables reversible, real-time modulation of nanopore transport through purely electrical control. This capability provides a versatile strategy for dynamically tuning ionic current rectification and represents an important step toward adaptive ionic circuitry and reconfigurable nanofluidic devices.

Switching the polarity of the gate potential to negative produces fundamentally different high-bias behavior. Because the gate-to-electrolyte potential difference remains strongly negative over the entire range of applied transmembrane biases investigated, electrostatic attraction continuously enriches counterions near the neighboring surface and suppresses the depletion region responsible for ionic current rectification. At moderate transmembrane biases, this enhanced counterion population increases the ionic conductivity and promotes transport through the nanopore. However, at sufficiently large transmembrane potentials, the current no longer increases with increasingly negative gate voltage. Instead, the current decreases slightly as the gate potential becomes more negative.

This behavior indicates that the transport-limiting mechanism changes once depletion has been eliminated. At a transmembrane potential of +2 V, all positive gate potentials between +0.2 V and +1.0 V converge to an identical current, indicating that electrostatic gating has completely suppressed depletion resistance and that the total conductance is governed primarily by the intrinsic pore and access resistances. In contrast, progressively more negative gate potentials continue to perturb the local electric field, producing stronger lateral electrostatic attraction that localizes counterions near the neighboring surface rather than directing them through the nanopore. Consequently, additional counterion enrichment does not translate into increased translocation through the channel but instead produces a slight reduction in the axial ionic flux. These observations demonstrate that electrostatic gating not only suppresses concentration polarization but also provides a means of continuously tuning the dominant transport mechanism through electrical control alone.

Electrostatic gating does not simply mimic a charged surface; rather, it dynamically controls the dominant transport mechanism by continuously modifying the gate-to-electrolyte potential difference. As a result, depletion formation, counterion enrichment, and ionic conductivity become electrically tunable, enabling reversible switching between distinct transport regimes that cannot be achieved through permanent chemical functionalization.

6.6 Gating of Ion Transport as a Function of the Distance from the Metallic Surface and Number of Pores

The next class of systems investigated consists of two distinct geometries. The first comprises single nanopores positioned at systematically varied distances from a neighboring surface, while the second consists of two- and three-pore array architectures in which only one

nanopore is directly coupled to the neighboring surface and the remaining nanopores are influenced indirectly through interpore interactions. For each of the systems we will be considering the same following boundary conditions as applied for a single nanopore system, i.e. floating potential, a fixed surface charge density, and an applied gate potential.

Because neighboring nanopores interact through the overlap of their ion depletion regions,[23, 24, 63] an analogous distance-dependent electrostatic coupling is expected between an individual nanopore and an adjacent surface. Systematically varying the pore-to-surface separation therefore provides a direct means of quantifying the spatial range and magnitude of this coupling under each electrostatic boundary condition.

The simulations shown in Figure 8 confirm this behavior. As the separation between the nanopore entrance and the neighboring surface increases, the electrostatic coupling progressively weakens, reducing the influence of the neighboring boundary condition on the ionic concentration profiles and current rectification. This reduction in coupling is observed for all three boundary conditions; however, the magnitude of the interactions depend strongly on the nature of the neighboring surface.

6.5 Nanopore Arrays

The next class of systems investigated consists of two distinct geometries. The first comprises single nanopores positioned at systematically varied distances from a neighboring surface, while the second consists of two- and three-pore array architectures in which only one nanopore is directly coupled to the neighboring surface and the remaining nanopores are influenced indirectly through interpore interactions. For each of the systems we will be

considering the following electrostatic boundary conditions: a floating potential and an applied gate potential.

6.7 ICR as a Function of Distance

Having established that electrically gated nanopores continuously transition between the limiting behaviors of floating-potential and fixed surface-charge boundary conditions, the remaining discussion focuses on the distance-dependent coupling produced by floating and electrically gated neighboring surfaces. Because neighboring nanopores interact through the overlap of their concentration polarization and ion depletion regions, an analogous electrostatic interaction is expected between an individual nanopore and a neighboring surface. Systematically varying the pore-to-surface separation therefore provides a direct means of quantifying both the magnitude and the spatial extent of this electrostatic coupling.

The simulations confirm the existence of a finite nanopore–surface interaction. As the separation between the nanopore entrance and the neighboring surface increases, the influence of the surface on the local ion distributions and ionic transport progressively decreases. Both floating-potential and electrically gated systems exhibit the same general trend, with the neighboring surface producing progressively weaker perturbations as the separation distance increases. Interestingly, although the magnitude of the interaction depends strongly on the electrolyte concentration and the applied gate potential, the characteristic interaction distance remains remarkably consistent. For all conditions investigated, the neighboring surface produces little measurable influence on nanopore transport once the separation exceeds approximately 20 nm, indicating the presence of a well-defined nanopore–surface coupling length.

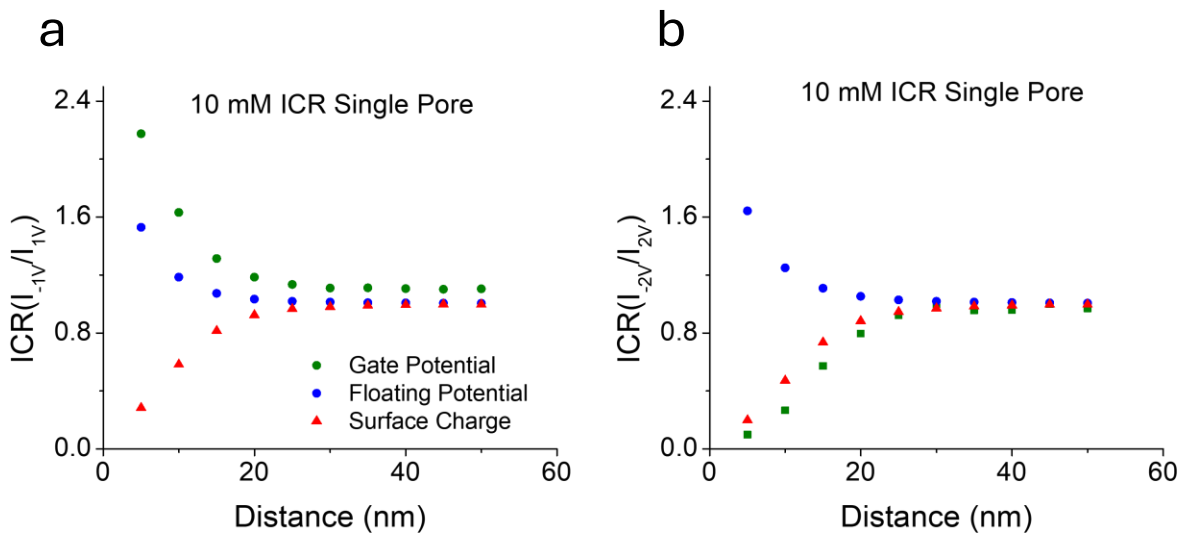

Figure 6.8 ICR Distributions. Ionic Current Rectification values for gating potential (+1 V), floating potential, and surface charge boundary conditions for 10 mM KCl as a function of distance from the neighboring surface. With the gate potential boundary condition, when the gate potential is lower (high) than the transmembrane potential, the behavior is similar to floating potential (surface charge) boundary condition. The gate potential in this figure is 1 V.

The magnitude of the electrostatic coupling is strongly dependent on the bulk electrolyte concentration. At low electrolyte concentrations, concentration polarization produces a more pronounced ion-depleted region and a larger transport resistance near the nanopore entrance. Consequently, perturbations introduced by a neighboring surface located within the interaction region produce comparatively large changes in the local ion distributions, electric field, and ionic current. As the electrolyte concentration increases, the depletion region becomes less severe and the local conductivity increases, substantially reducing the sensitivity of the nanopore to neighboring electrostatic perturbations. The neighboring surface therefore produces a much smaller change in the measured current despite maintaining the same physical separation from the nanopore.

Although the depletion region extends substantially farther into the reservoir at lower electrolyte concentrations, the characteristic interaction distance remains approximately 20 nm for all concentrations investigated. This observation indicates that the coupling length is not determined solely by the spatial extent of the depletion region. Rather, the neighboring surface modifies ionic transport only when its electrostatic perturbation overlaps the localized access region immediately surrounding the nanopore entrance, where the electric field and ionic flux converge into the channel. While concentration polarization may extend well beyond this region, its outer portion contributes comparatively little to the pore-access resistance. Consequently, perturbations introduced beyond the localized entrance region have only a negligible influence on the measured current, even though the depletion profile itself remains spatially extended.

These observations demonstrate that the magnitude and spatial range of nanopore–surface coupling are governed by distinct physical mechanisms. The electrolyte concentration primarily determines the strength of the interaction by controlling the severity of concentration polarization and the resistance associated with the depleted entrance region. In contrast, the interaction distance is governed primarily by the geometry of the nanopore access region and the finite spatial overlap between the neighboring surface and the pore-directed electric field. The approximately 20 nm interaction distance therefore represents an effective nanopore–surface coupling length rather than the full extent of the depletion region or the equilibrium Debye screening length.

The same characteristic interaction distance is observed for both floating-potential and electrically gated surfaces despite the substantially stronger electrostatic perturbations generated by the latter. This result further supports the conclusion that the electrical boundary condition primarily determines the magnitude of the local electrostatic perturbation, whereas the geometry

of the nanopore entrance determines the spatial range over which that perturbation can influence ionic transport. From a device perspective, this finite coupling length establishes an important design criterion for electrically gated nanopores and future ionic circuits. Neighboring electrodes or nanostructures positioned within this interaction region can effectively modulate ionic transport, whereas structures located beyond approximately 20 nm become largely electrostatically decoupled from the nanopore.

Among the two cases, the floating-potential boundary condition produces the weakest electrostatic perturbation. Consequently, its influence decays rapidly with increasing separation distance. For a bulk electrolyte concentration of 10 mM, the neighboring floating surface no longer produces a measurable effect on nanopore transport once the separation exceeds approximately 20 nm. In contrast, both the fixed surface-charge and applied gate-potential boundary conditions generate substantially stronger electric fields that extend farther into the electrolyte, allowing significant electrostatic coupling to persist over considerably larger separation distances.

6.8 Nanopore Arrays: Propagation of Electrostatic Coupling Through Ionic Networks

Having established the electrostatic interaction between an individual nanopore and a neighboring surface, the next logical system to investigate is a nanopore array. Unlike isolated nanopores, ionic transport in nanopore arrays is governed not only by interactions between each nanopore and the surrounding electrolyte but also by electrostatic coupling between neighboring pores through their overlapping concentration polarization regions. Consequently, a local electrostatic perturbation introduced at one pore has the potential to influence transport

throughout the array. Understanding how these perturbations propagate is essential for the rational design of ionic circuits composed of multiple interacting nanopores.

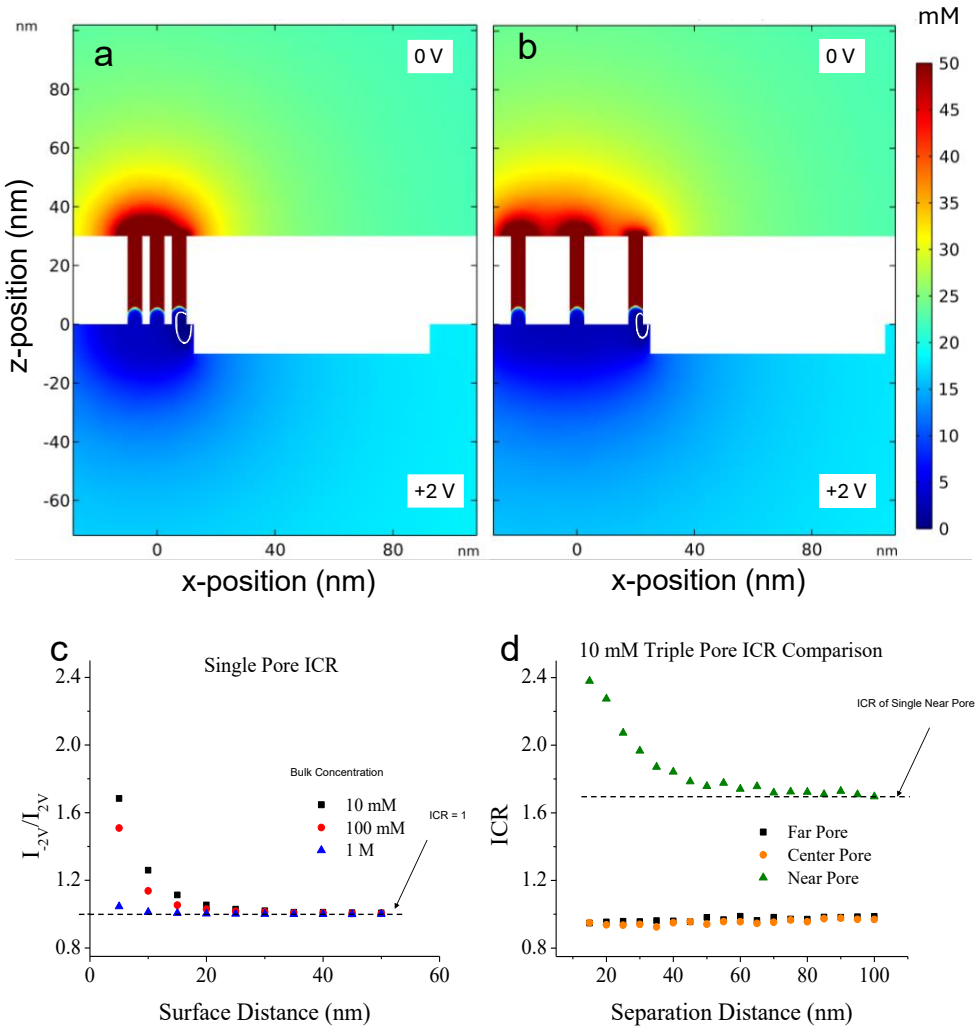

Figure 6.9 ICR for Nanopore Arrays with Floating Potential Boundary Condition. Panels (a–b) show total ionic concentration maps at a transmembrane potential of +2 V and a bulk KCl concentration of 10 mM for pore-to-pore distances of (a) 7.5 nm and (b) 20 nm. The white contour indicates a total ionic concentration of 10 mM, while darker blue regions correspond to concentrations below 10 mM. Tighter pore spacing produces a larger depletion region and greater current suppression in the pore nearest the conductive surface. Panels (c–d) compare the

ICR of a single pore (c) with the individual ICR values of pores within the array (d). Significant rectification is observed primarily for the pore nearest the conductive surface, demonstrating that the surface-induced effect is spatially localized.

To investigate this behavior, two- and three-pore arrays were considered in which a neighboring surface was positioned 5 nm from the entrance of the first nanopore while the pore-to-pore spacing was systematically varied from 10 to 40 nm. Based on the single-pore results presented in the previous section, direct electrostatic coupling between a nanopore and the neighboring surface becomes negligible once their separation exceeds approximately 20 nm, independent of the applied electrical boundary condition. Consequently, any changes observed in pores located beyond this characteristic interaction distance cannot result from direct nanopore–surface coupling but instead must arise through electrostatic interactions transmitted between neighboring nanopores within the array.

Models incorporating a floating-potential boundary condition showed that, across nearly all pore-to-pore distances investigated, the pore nearest the conductive surface exhibited rectification characterized by current suppression at positive transmembrane potentials. In contrast, the remaining pores in the array maintained ICR values near unity, indicating approximately symmetric I–V behavior. This trend is clearly illustrated in Figure 6.9d. Interestingly, as the pore-to-pore distance decreased, both the current suppression and rectification of the pore nearest the conductive surface increased. This behavior suggests that closely spaced pores interact through their overlapping ionic environments and increasingly compete for available ions[2]. The resulting enhancement of local ion depletion increases the effective resistance of the neighboring pore and, consequently, its rectification.

As the pore-to-pore distance increased, the ICR of the pore nearest the conductive surface approached that of the corresponding single-pore model, indicating progressively weaker pore–pore interactions and increasingly independent transport behavior. Importantly, these results demonstrate that **functionally distinct pores can be produced within the same nanopore array without requiring individual chemical modification of each pore**. Simply positioning a nanopore array near a conductive surface can produce a system in which one pore exhibits pronounced rectification while neighboring pores retain nearly symmetric, resistor-like I–V behavior. This provides a comparatively simple strategy for creating heterogeneous ionic transport functionality within a single membrane.

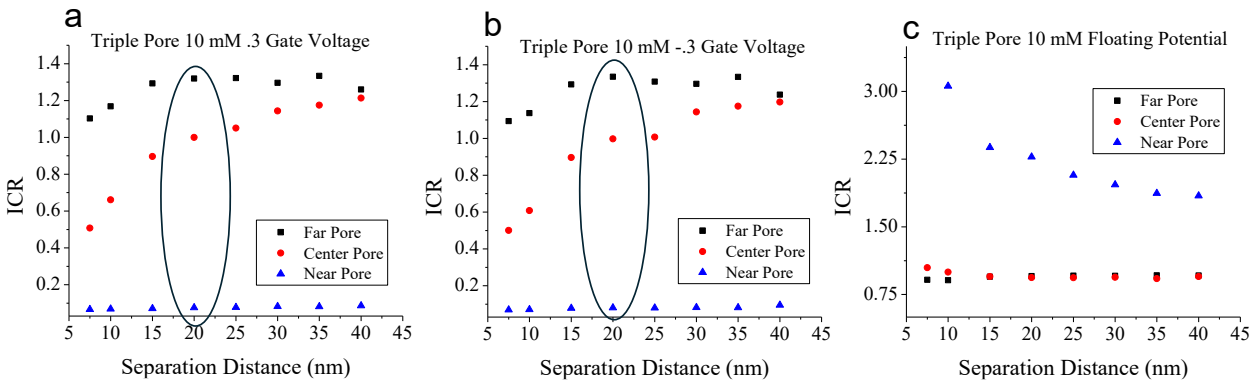

Figure 6.10 ICR as a Function of Pore-to-Pore Distance for Gate and Floating Potential Models. Panels (a–c) show the ionic current rectification (ICR) values of individual nanopores within a three-pore array as a function of pore length. All models were simulated at a bulk KCl concentration of 10 mM. Panel (a) corresponds to a gate potential of +0.3 V applied to the neighboring surface, panel (b) to a gate potential of −0.3 V, and panel (c) to a floating-potential boundary condition. ICR was calculated as the ratio of the current magnitudes measured at −2 V and +2 V transmembrane potentials.

The electrically gated systems exhibit particularly rich transport behavior. We see in figure 6.10 that, as the pore-to-pore spacing approaches the characteristic interaction length identified in the single-pore models, the transport response of individual nanopores becomes spatially differentiated despite the gate potential being applied only adjacent to the first pore. Rather than responding uniformly to the applied gate voltage, the nanopores assume distinct transport characteristics depending on their position within the array. Nanopores located nearest the gated surface exhibit enhanced current under positive transmembrane bias and behave similarly to positively rectifying ionic diodes. In contrast, nanopores positioned near the characteristic interaction distance exhibit nearly symmetric current–voltage responses with minimal rectification, resembling ohmic ionic resistors. Nanopores located beyond this interaction distance exhibit slight current suppression under positive bias, resulting in weak rectification in the **opposite direction** to that observed for the pore nearest the conductive surface.

These observations demonstrate that the electrostatic perturbation introduced by the neighboring gate is not transmitted directly to distant nanopores. Instead, the perturbation is redistributed through successive electrostatic interactions between neighboring pores. The first nanopore responds directly to the applied gate potential, modifying its local electric field and concentration polarization. This modified electrochemical environment subsequently perturbs the adjacent nanopore, which in turn influences the next pore in the array. Consequently, electrostatic information propagates through the nanopore network by a sequence of localized interpore interactions rather than by long-range direct coupling between the gate and distant nanopores. The approximately 20 nm interaction length identified in the single-pore systems

therefore emerges as the fundamental length scale governing both nanopore–surface and interpore electrostatic coupling.

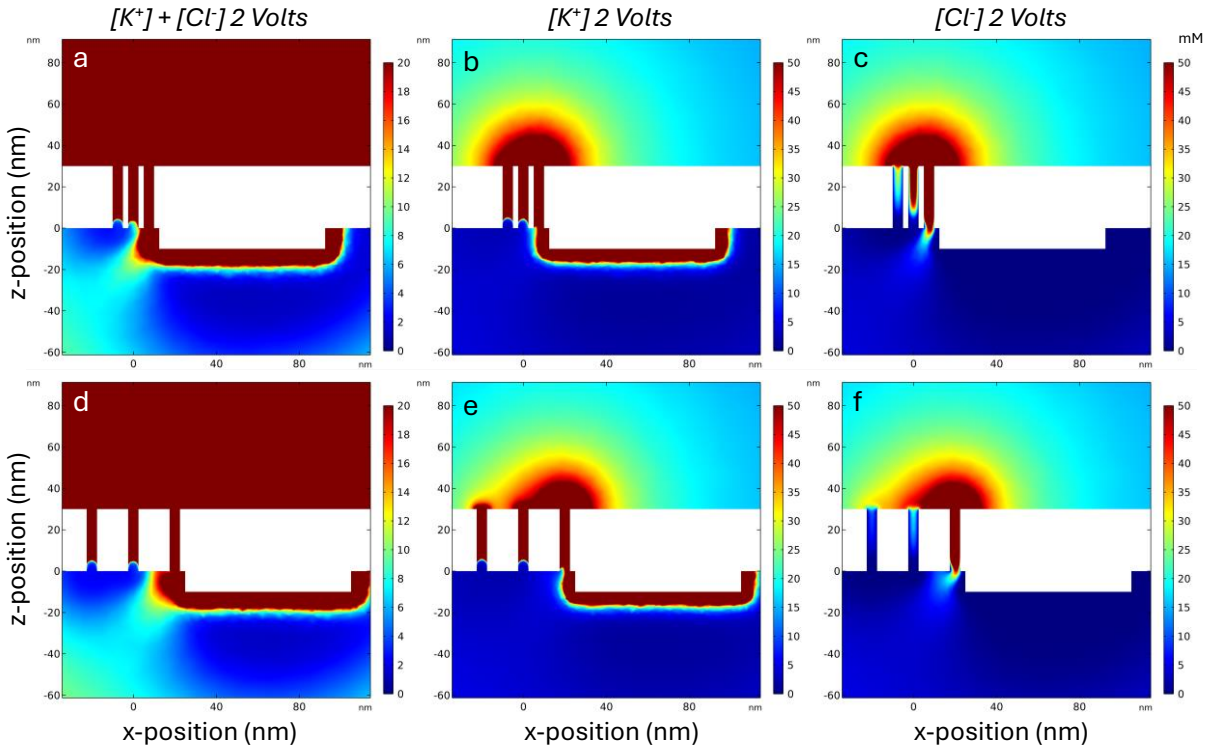

Figure 6.11 Concentration Heat Maps of Triple Pore Gating Models at 2 Volts. This figure shows ionic concentration profiles for three-pore nanopore arrays with pore-to-pore spacings of (a–c) 7.5 nm and (d–f) 20 nm. Panels (a, d) show the total ionic concentration, panels (b, e) show the K^+ concentration, and panels (c, f) show the Cl^- concentration. All concentration maps were obtained at a bulk KCl concentration of 10 mM and an applied transmembrane potential of +2 V.

Perhaps the most significant consequence of this behavior is the spontaneous emergence of multiple ionic circuit elements within a single gated nanopore array. By varying only the relative pore spacing, the array simultaneously produces nanopores exhibiting diode-like rectification, nearly ideal resistive behavior, and weak current suppression without requiring independent electrical control of each pore. The functional behavior of each nanopore is therefore determined collectively through electrostatic interactions within the network rather than

by its individual geometry or surface chemistry alone. These results demonstrate that local electrical gating can generate nonlocal transport responses throughout an interconnected nanopore array, providing a mechanism for constructing adaptive ionic circuits in which multiple functional elements emerge from a single externally applied electrical stimulus.

While this work has not yet been published and the underlying mechanism remains under investigation, the current hypothesis is that **pore selectivity changes as a function of pore-to-pore distance**, resulting in an increasing contribution of chloride ions to the total ionic current. This suggests a dynamic relationship between pore spacing, ion selectivity, and rectification behavior. At a pore-to-pore distance of approximately 20 nm, the selectivity of the central pore appears to produce nearly symmetric, resistor-like I–V behavior for the central channel, even though its local depletion region remains influenced by the highly conducting pore nearest the conductive surface. Evidence supporting a change in selectivity is shown in Figure 6.11(c, f), where the chloride concentration varies among the individual pores within the array. Furthermore, the overall chloride concentration within the pores is enhanced at smaller pore-to-pore distances. These results suggest that changes in co-ion participation may contribute to the distinct transport behaviors observed among neighboring pores as the array spacing is varied.

Collectively, these results establish that ionic transport in nanopore systems is governed by two independent electrostatic length scales. The first determines the magnitude of electrostatic perturbations through electrolyte-dependent concentration polarization, whereas the second defines a characteristic electrostatic coupling length over which neighboring structures can influence transport. Because this interaction length governs both nanopore–surface and interpore coupling, it represents a fundamental design parameter for electrically programmable nanofluidic systems. Local electrical gating therefore provides not only dynamic control over

individual nanopores but also a mechanism for propagating electrostatic information through nanopore networks, enabling the spontaneous emergence of multiple iontronic circuit elements from a single applied electrical stimulus.

CHAPTER 7 Conclusions and Outlook for Biomimetic Iontronics

Solid-state nanopores provide a versatile platform for controlling ionic transport at nanometer length scales and represent promising building blocks for biomimetic iontronic systems. A central finding of this dissertation, however, is that the functional dimensions of a nanopore are not necessarily defined by its physical geometry. Ion-selective transport generates ion concentration polarization (ICP), producing concentration and electrostatic potential gradients that extend from the nanopore into the surrounding electrolyte. These extended fields contribute directly to nanopore resistance, mediate interactions between neighboring structures, and provide a mechanism through which external electrostatic boundary conditions can regulate ionic transport.

The central objective of this dissertation was therefore to determine how this nonlocal character of nanoscale ionic transport influences individual nanopores and small nanopore arrays. Through experiments and continuum simulations, the effects of nanopore geometry, surface charge, electrolyte concentration, interpore separation, and neighboring electrostatic boundary conditions were systematically investigated. Collectively, the results establish ICP as a unifying mechanism connecting three central observations: **nonadditive conductance in closely spaced nanopore arrays, reduced sensitivity of conductance to nanopore length under strongly concentration-polarized conditions, and electrostatic coupling between nanopores and nearby conductive surfaces.**

These findings lead to a broader physical picture in which a nanopore cannot always be treated as an isolated resistor confined to the geometrical dimensions of its channel. Instead, the nanopore and the surrounding concentration-polarized electrolyte constitute a coupled transport element whose functional boundaries can extend tens of nanometers beyond the physical pore.

This distinction between the **geometrical nanopore** and its **functional electrochemical environment** provides the central framework connecting the results of this dissertation.

Chapter 4 examined this principle through minimal arrays containing two and three nanopores. Experimental measurements and three-dimensional continuum simulations demonstrated that closely spaced nanopores do not necessarily behave as independent parallel conductors. Ion-selective transport generates depletion regions outside the nanopore entrances, and when neighboring pores are sufficiently close, these regions overlap. The resulting reduction in local ionic concentration suppresses the total conductance of the array relative to the conductance expected from independent nanopores. The magnitude of this interaction depends strongly on electrolyte concentration, interpore separation, applied potential, and pore-wall surface properties.

These results established ICP as a mechanism of communication between neighboring nanoscale transport elements. Importantly, the coupling does not require direct physical contact between nanopores. Instead, information about the transport state of one nanopore is effectively transmitted through changes in the surrounding ionic concentration field. Modification of the nanopore surface charge further demonstrated that this interaction can be controlled. Patterned surface charge produced diode-like nanopores and redistributed the corresponding enrichment and depletion regions, thereby changing the strength of interpore coupling.

Chapter 5 examined another consequence of the nonlocal nature of ICP by investigating ionic transport through nanopores of different lengths. Classical descriptions of pore resistance predict a strong dependence of conductance on pore length because increasing the channel length increases the resistance of the electrolyte contained within the pore. The simulations and

experimental observations presented in this dissertation demonstrate that this geometric interpretation becomes incomplete when substantial ICP develops.

Under conditions where strongly ion-selective nanopores generate extended depletion regions, a significant fraction of the total electrical resistance can reside outside the physical nanopore. Increasing pore length therefore does not necessarily increase the total resistance proportionally because the contribution of the external depletion region can dominate or compensate for changes in internal pore resistance. Consequently, nanopores with substantially different physical lengths can exhibit nearly identical ionic conductance.

This result provides an important conceptual extension of conventional nanopore transport models. The effective electrical length of a nanopore is not necessarily identical to its geometrical length. Instead, the relevant transport region can include both the physical nanopore and the concentration-polarized electrolyte surrounding its entrances. The relationship between ICP and ion selectivity further demonstrates that these effects are coupled: surface-charge-induced selectivity enables preferential ionic transport, which generates ICP, while the resulting concentration distributions subsequently modify the resistance and transport characteristics of the nanopore.

Chapter 6 extended these concepts by introducing a neighboring conductive surface near the nanopore entrance. Unlike the pore–pore interactions examined in Chapter 4, this configuration allowed the influence of the surrounding electrostatic boundary condition to be investigated independently of transport through a second nanopore. Floating-potential, fixed-surface-charge, and externally applied gate-potential boundary conditions produced distinct modifications of the concentration and potential distributions surrounding the nanopore.

The influence of the neighboring surface decreased as the separation between the nanopore and surface increased, confirming that the coupling originates from modifications to the local electrochemical environment surrounding the pore entrance. However, the introduction of an externally applied gate potential provided an additional level of control. By changing the potential difference between the neighboring surface and the electrolyte surrounding the nanopore, the gate could promote either enrichment or depletion near the nanopore entrance and thereby modify ionic current.

The behavior became particularly significant in small nanopore arrays. Because individual nanopores occupied different spatial positions relative to the gated surface and to one another, the same applied gate potential could generate different transport responses among pores within a single array. Under appropriate conditions, individual nanopores could exhibit diode-like behavior with opposite rectification polarities while another pore exhibited an approximately symmetric current response. Thus, spatially uniform nanopore geometry does not necessarily produce spatially uniform functionality when the pores occupy different electrochemical environments.

7.1 Unifying Physical Picture

The results of Chapters 4–6 support a common physical interpretation of nanoscale ionic transport. A nanopore does not interact exclusively with the ions located within its geometrical volume. Instead, selective transport modifies ionic concentrations and electric potentials in the surrounding reservoirs, producing an extended electrochemical environment that participates directly in determining nanopore conductance.

This environment provides a mechanism through which geometry, surface chemistry, neighboring pores, and external electrodes become coupled. A neighboring nanopore can modify the concentration field experienced by another pore. A charged or polarized surface can alter the electrostatic potential and ionic composition near a pore entrance. An external gate can dynamically modify these distributions. In each case, the measured ionic current reflects the response of the complete coupled system rather than an isolated nanopore.

This perspective also provides a useful distinction between geometric and functional proximity. Two structures do not necessarily need to be physically connected to interact strongly. Instead, they must be sufficiently close that the electrochemical perturbation generated by one structure extends into the transport environment of the other. The characteristic interaction distance is therefore not determined by geometry alone but also by electrolyte concentration, surface charge, applied potential, ion selectivity, and the magnitude of ICP.

This principle has important consequences for the design of nanopore arrays. Increasing the number of nanopores in a membrane cannot always be expected to increase current proportionally because sufficiently closely spaced pores may compete for the same local ionic environment. Conversely, this apparent limitation can become a functional advantage when interactions are intentionally engineered. Overlapping concentration fields provide a mechanism for coupling nanoscale ionic components without requiring direct physical connections between them.

7.2 Implications for Biomimetic Iontronics

Biological ionic systems derive much of their functionality from networks of interacting ion channels rather than from isolated transport elements. Although the solid-state nanopores

investigated in this dissertation are substantially simpler than biological ion channels, the results demonstrate several physical principles that could support analogous collective functionality in synthetic systems.

Individual nanopores can exhibit selective conduction and diode-like rectification. Their transport properties can be altered by neighboring nanopores through shared concentration fields. Conductive surfaces can modify the local electrochemical environment, and externally applied gate potentials can dynamically regulate ionic transport. Most importantly, different pores within the same small array can exhibit different functional responses despite possessing similar geometrical structures.

These properties suggest a pathway toward nanopore-based ionic circuits in which functionality emerges not only from the design of individual pores but also from their spatial arrangement and interactions. In such systems, ICP would no longer represent merely a transport limitation. Instead, concentration polarization could function as a coupling mechanism through which the state of one ionic element modifies the response of another.

This approach differs fundamentally from conventional electronic circuitry. Electronic components are typically connected through metallic conductors that transport electronic charge between discrete circuit elements. In nanopore-based iontronic systems, coupling may instead occur through dynamically evolving ionic concentration and electrostatic potential fields within the electrolyte. The surrounding solution therefore becomes an active component of the circuit architecture.

7.3 Future Directions

The systems considered in this dissertation represent minimal architectures containing only a small number of nanopores and comparatively simple electrostatic boundary conditions. The next step is to extend these principles toward larger and increasingly heterogeneous nanopore networks.

One particularly important direction is the fabrication and characterization of arrays in which individual nanopores possess intentionally different surface-charge distributions, geometries, or gating environments. Such heterogeneous arrays could combine ionic resistors, diodes, gated elements, and potentially memory-dependent components within a single membrane. Controlling the spacing between these elements would provide an additional mechanism for tuning their interactions through ICP.

Experimental realization of individually addressable gates represents another important objective. The neighboring conductive surfaces investigated here demonstrate that electrostatic boundary conditions outside the nanopore can significantly modify transport. Patterned electrodes positioned near selected nanopores could therefore provide spatially resolved control over individual components within an array. Independent gate electrodes would enable the transport state of one region to be modified without changing the transmembrane potential applied to the entire device.

Time-dependent transport represents another important extension. The present work primarily considers steady-state ionic distributions, whereas biological ionic systems frequently operate under oscillating or transient conditions. Because concentration polarization develops and relaxes over finite time scales, dynamically varying potentials may introduce history dependence, delayed coupling, and memory into nanopore arrays. Combining spatial coupling

with temporal dynamics could therefore enable substantially more complex ionic functionality than is accessible under steady-state conditions.

Further theoretical work should also investigate the limits of the continuum description as nanopore dimensions approach molecular length scales. The Poisson–Nernst–Planck framework employed throughout this dissertation captures the principal concentration and electrostatic effects relevant to the systems considered here, but it does not explicitly describe ion-specific adsorption, hydration, dielectric heterogeneity, molecular-scale surface structure, or stochastic transport. Incorporating these effects where necessary will be important for extending the design principles identified here toward increasingly confined nanopores and chemically complex interfaces.

Ultimately, the development of functional iontronic networks will require simultaneous control over nanopore geometry, surface chemistry, spatial organization, electrolyte composition, and external electrostatic fields. The results presented in this dissertation provide a physical framework for understanding how these parameters interact.

7.4 Final Conclusions

The central conclusion of this dissertation is that **the functional boundaries of a nanopore can extend substantially beyond its physical boundaries**. Ion concentration polarization generates concentration and electrostatic potential fields in the surrounding electrolyte that contribute directly to transport resistance and provide a mechanism for coupling nanopores to neighboring pores, surfaces, and external electrodes. This principle explains the nonadditive conductance of closely spaced nanopore arrays, the reduced dependence of

conductance on physical pore length under strongly concentration-polarized conditions, and the ability of neighboring conductive surfaces to regulate nanopore transport without direct contact.

The surrounding electrolyte should therefore not be regarded simply as a passive reservoir supplying ions to an isolated nanopore. Under ion-selective nanoscale transport, the electrolyte becomes an active component of the device: its spatially and temporally evolving concentration and potential distributions determine how individual transport elements interact and how the collective system responds to external stimuli.

This perspective shifts the design problem from engineering individual nanopores to engineering **coupled electrochemical environments**. Control over pore geometry, surface charge, spatial arrangement, electrolyte composition, and electrostatic gating provides a means of programming interactions among nanoscale ionic components. Behaviors that appear undesirable when nanopores are treated as independent elements—such as concentration polarization and nonadditive conductance—can consequently become functional mechanisms when interactions are deliberately designed.

The results presented in this dissertation therefore establish both a fundamental understanding of coupled nanoscale ionic transport and a pathway toward biomimetic iontronic systems in which ionic signals can be selectively conducted, rectified, gated, and ultimately processed through networks of interacting nanoscale components.

LIST OF REFERENCES

(1) Emmerich, T.; Ronceray, N.; Agrawal, K. V.; Garaj, S.; Kumar, M.; Noy, A.; Radenovic, A. Nanofluidics. *Nat. Rev. Methods Primer* **2024**, *4* (1), 69. https://doi.org/10.1038/s43586-024-00344-0

(2) Cao, E.; Cain, D.; Silva, S.; Siwy, Z. S. Ion Concentration Polarization Tunes Interpore Interactions and Transport Properties of Nanopore Arrays. *Adv. Funct. Mater.* **2024**, *34* (11), 2312646. https://doi.org/10.1002/adfm.202312646

(3) Cain, D.; Cao, E.; Vlassiouk, I.; Schäffer, T. E.; Siwy, Z. S. Ion Concentration Polarization Causes a Nearly Pore-Length-Independent Conductance of Nanopores. *Faraday Discuss.* **2025**, *257*, 344–359. https://doi.org/10.1039/D4FD00148F

(4) Yeh, L.-H.; Zhang, M.; Qian, S.; Hsu, J.-P.; Tseng, S. Ion Concentration Polarization in Polyelectrolyte-Modified Nanopores. *J. Phys. Chem. C* **2012**, *116* (15), 8672–8677. https://doi.org/10.1021/jp301957j

(5) Ma, L.; Li, Z.; Yuan, Z.; Huang, C.; Siwy, Z. S.; Qiu, Y. Modulation of Ionic Current Rectification in Ultrashort Conical Nanopores. *Anal. Chem.* **2020**, *92* (24), 16188–16196. https://doi.org/10.1021/acs.analchem.0c03989

(6) Yu, L.; Li, X.; Luo, C.; Lei, Z.; Wang, Y.; Hou, Y.; Wang, M.; Hou, X. Bioinspired Nanofluidic Iontronics for Brain-like Computing. *Nano Res.* **2024**, *17* (2), 503–514. https://doi.org/10.1007/s12274-023-5900-y

(7) Login, F. H.; Nejsum, L. N. Aquaporin Water Channels: Roles beyond Renal Water Handling. *Nat. Rev. Nephrol.* **2023**, *19* (9), 604–618. https://doi.org/10.1038/s41581-023-00734-9

(8) Fu, D.; Lu, M. The Structural Basis of Water Permeation and Proton Exclusion in Aquaporins (Review). *Mol. Membr. Biol.* **2007**, *24* (5–6), 366–374. https://doi.org/10.1080/09687680701446965

(9) Doyle, D. A.; Cabral, J. M.; Pfuetzner, R. A.; Kuo, A.; Gulbis, J. M.; Cohen, S. L.; Chait, B. T.; MacKinnon, R. The Structure of the Potassium Channel: Molecular Basis of K^+ Conduction and Selectivity. *Science* **1998**, *280* (5360), 69–77. https://doi.org/10.1126/science.280.5360.69

(10) MacKinnon, R. Potassium Channels and the Atomic Basis of Selective Ion Conduction (Nobel Lecture). *Angew. Chem. Int. Ed.* **2004**, *43* (33), 4265–4277. https://doi.org/10.1002/anie.200400662

(11) Choe, S. Potassium Channel Structures. *Nat. Rev. Neurosci.* **2002**, *3* (2), 115–121. https://doi.org/10.1038/nrn727

(12) Kuang, Q.; Purhonen, P.; Hebert, H. Structure of Potassium Channels. *Cell. Mol. Life Sci.* **2015**, *72* (19), 3677–3693. https://doi.org/10.1007/s00018-015-1948-5

(13) Hodgkin, A. L.; Huxley, A. F. Currents Carried by Sodium and Potassium Ions through the Membrane of the Giant Axon of *Loligo*. *J. Physiol.* **1952**, *116* (4), 449–472. https://doi.org/10.1113/jphysiol.1952.sp004717

(14) Hodgkin, A. L.; Huxley, A. F. A Quantitative Description of Membrane Current and Its Application to Conduction and Excitation in Nerve. *J. Physiol.* **1952**, *117* (4), 500–544. https://doi.org/10.1113/jphysiol.1952.sp004764

(15) Li, J.; Stein, D.; McMullan, C.; Branton, D.; Aziz, M. J.; Golovchenko, J. A. Ion-Beam Sculpting at Nanometre Length Scales. *Nature* **2001**, *412* (6843), 166–169. https://doi.org/10.1038/35084037

(16) Storm, A. J.; Chen, J. H.; Ling, X. S.; Zandbergen, H. W.; Dekker, C. Fabrication of Solid-State Nanopores with Single-Nanometre Precision. *Nat. Mater.* **2003**, *2* (8), 537–540. https://doi.org/10.1038/nmat941

(17) Kim, M. J.; Wanunu, M.; Bell, D. C.; Meller, A. Rapid Fabrication of Uniformly Sized Nanopores and Nanopore Arrays for Parallel DNA Analysis. *Adv. Mater.* **2006**, *18* (23), 3149–3153. https://doi.org/10.1002/adma.200601191

(18) Li, Z.; Mathwig, K.; Arotiba, O. A.; Tshwenya, L.; Batista Carneiro Neto, E.; Chaves Pereira, E.; Marken, F. Driving Electrochemical Membrane Processes with Coupled Ionic Diodes. *Curr. Opin. Electrochem.* **2023**, *39*, 101280. https://doi.org/10.1016/j.coelec.2023.101280

(19) Zhang, H.; Ai, B.; Gong, Z.; Sui, T.; Siwy, Z. S.; Qiu, Y. Ion Transport through Differently Charged Nanoporous Membranes: From a Single Nanopore to Multinanopores. *Anal. Chem.* **2025**, *97* (35), 19218–19231. https://doi.org/10.1021/acs.analchem.5c03051

(20) Emmerich, T.; Teng, Y.; Ronceray, N.; Lopriore, E.; Chiesa, R.; Chernev, A.; Artemov, V.; Di Ventra, M.; Kis, A.; Radenovic, A. Nanofluidic Logic with Mechano–Ionic Memristive Switches. *Nat. Electron.* **2024**, *7* (4), 271–278. https://doi.org/10.1038/s41928-024-01137-9

(21) Edri Fraiman, N.; Sabbagh, B.; Yossifon, G.; Fish, A. Toward an Ion-Based Large-Scale Integrated Circuit: Design, Simulation, and Integration. *Commun. Eng.* **2025**, *4* (1), 180. https://doi.org/10.1038/s44172-025-00511-5

(22) Tunuguntla, R. H.; Henley, R. Y.; Yao, Y.-C.; Pham, T. A.; Wanunu, M.; Noy, A. Enhanced Water Permeability and Tunable Ion Selectivity in Subnanometer Carbon Nanotube Porins. *Science* **2017**, *357* (6353), 792–796. https://doi.org/10.1126/science.aan2438

(23) Kopec, W.; Köpfer, D. A.; Vickery, O. N.; Bondarenko, A. S.; Jansen, T. L. C.; De Groot, B. L.; Zachariae, U. Direct Knock-on of Desolvated Ions Governs Strict Ion Selectivity in K+ Channels. *Nat. Chem.* **2018**, *10* (8), 813–820. https://doi.org/10.1038/s41557-018-0105-9

(24) Mayer, S. F.; Cao, C.; Dal Peraro, M. Biological Nanopores for Single-Molecule Sensing. *iScience* **2022**, *25* (4), 104145. https://doi.org/10.1016/j.isci.2022.104145

(25) Miles, B. N.; Ivanov, A. P.; Wilson, K. A.; Doğan, F.; Japrung, D.; Edel, J. B. Single Molecule Sensing with Solid-State Nanopores: Novel Materials, Methods, and Applications. *Chem Soc Rev* **2013**, *42* (1), 15–28. https://doi.org/10.1039/C2CS35286A

(26) Hu, R.; Tong, X.; Zhao, Q. Four Aspects about Solid-State Nanopores for Protein Sensing: Fabrication, Sensitivity, Selectivity, and Durability. *Adv. Healthc. Mater.* **2020**, *9* (17), 2000933. https://doi.org/10.1002/adhm.202000933

(27) Fan, Q.; Xu, C.; Liu, W.; Zhang, Z.; Chen, Y.; Sha, J. Self-Heating-Induced Blocking in Nanopores Enables Neuromorphic Ionic Computing. *Nat. Commun.* **2026**, *17* (1), 8635. https://doi.org/10.1038/s41467-026-75570-z

(28) Ritmejeris, J.; Chen, X.; Dekker, C. Single-Molecule Protein Sequencing with Nanopores. *Nat. Rev. Bioeng.* **2024**, *3* (4), 303–316. https://doi.org/10.1038/s44222-024-00260-8

(29) Laucirica, G.; Toimil-Molares, M. E.; Trautmann, C.; Marmisollé, W.; Azzaroni, O. Nanofluidic Osmotic Power Generators – Advanced Nanoporous Membranes and Nanochannels for Blue Energy Harvesting. *Chem. Sci.* **2021**, *12* (39), 12874–12910. https://doi.org/10.1039/D1SC03581A

(30) Zhu, Z.; Wang, D.; Tian, Y.; Jiang, L. Ion/Molecule Transportation in Nanopores and Nanochannels: From Critical Principles to Diverse Functions. *J. Am. Chem. Soc.* **2019**, *141* (22), 8658–8669. https://doi.org/10.1021/jacs.9b00086

(31) Shi, W.; Friedman, A. K.; Baker, L. A. Nanopore Sensing. *Anal. Chem.* **2017**, *89* (1), 157–188. https://doi.org/10.1021/acs.analchem.6b04260

(32) Deng, T.; Li, M.; Wang, Y.; Liu, Z. Development of Solid-State Nanopore Fabrication Technologies. *Sci. Bull.* **2015**, *60* (3), 304–319. https://doi.org/10.1007/s11434-014-0705-8

(33) Fried, J. P.; Swett, J. L.; Nadappuram, B. P.; Mol, J. A.; Edel, J. B.; Ivanov, A. P.; Yates, J. R. *In Situ* Solid-State Nanopore Fabrication. *Chem. Soc. Rev.* **2021**, *50* (8), 4974–4992. https://doi.org/10.1039/D0CS00924E

(34) Apel, P. Y.; Korchev, Yu. E.; Siwy, Z.; Spohr, R.; Yoshida, M. Diode-like Single-Ion Track Membrane Prepared by Electro-Stopping. *Nucl. Instrum. Methods Phys. Res. Sect. B Beam Interact. Mater. At.* **2001**, *184* (3), 337–346. https://doi.org/10.1016/S0168-583X(01)00722-4

(35) Siwy, Z. S. Ion-Current Rectification in Nanopores and Nanotubes with Broken Symmetry. *Adv. Funct. Mater.* **2006**, *16* (6), 735–746. https://doi.org/10.1002/adfm.200500471

(36) He, Y.; Tsutsui, M.; Zhou, Y.; Miao, X.-S. Solid-State Nanopore Systems: From Materials to Applications. *NPG Asia Mater.* **2021**, *13* (1), 48. https://doi.org/10.1038/s41427-021-00313-z

(37) Masuda, H.; Fukuda, K. Ordered Metal Nanohole Arrays Made by a Two-Step Replication of Honeycomb Structures of Anodic Alumina. *Science* **1995**, *268* (5216), 1466–1468. https://doi.org/10.1126/science.268.5216.1466

(38) Lee, W.; Park, S.-J. Porous Anodic Aluminum Oxide: Anodization and Templated Synthesis of Functional Nanostructures. *Chem. Rev.* **2014**, *114* (15), 7487–7556. https://doi.org/10.1021/cr500002z

(39) Kwok, H.; Briggs, K.; Tabard-Cossa, V. Nanopore Fabrication by Controlled Dielectric Breakdown. *PLoS ONE* **2014**, *9* (3), e92880. https://doi.org/10.1371/journal.pone.0092880

(40) Briggs, K.; Charron, M.; Kwok, H.; Le, T.; Chahal, S.; Bustamante, J.; Waugh, M.; Tabard-Cossa, V. Kinetics of Nanopore Fabrication during Controlled Breakdown of Dielectric Membranes in Solution. *Nanotechnology* **2015**, *26* (8), 084004. https://doi.org/10.1088/0957-4484/26/8/084004

(41) Zhang, S.; Li, M.; Su, B.; Shao, Y. Fabrication and Use of Nanopipettes in Chemical Analysis. *Annu. Rev. Anal. Chem.* **2018**, *11* (1), 265–286. https://doi.org/10.1146/annurev-anchem-061417-125840

(42) Garaj, S.; Hubbard, W.; Reina, A.; Kong, J.; Branton, D.; Golovchenko, J. A. Graphene as a Subnanometre Trans-Electrode Membrane. *Nature* **2010**, *467* (7312), 190–193. https://doi.org/10.1038/nature09379

(43) Liu, K.; Feng, J.; Kis, A.; Radenovic, A. Atomically Thin Molybdenum Disulfide Nanopores with High Sensitivity for DNA Translocation. *ACS Nano* **2014**, *8* (3), 2504–2511. https://doi.org/10.1021/nn406102h

(44) Seidel, H.; Csepregi, L.; Heuberger, A.; Baumgärtel, H. Anisotropic Etching of Crystalline Silicon in Alkaline Solutions: I . Orientation Dependence and Behavior of Passivation Layers. *J. Electrochem. Soc.* **1990**, *137* (11), 3612–3626. https://doi.org/10.1149/1.2086277

(45) Walker, R. C.; Shi, T.; Silva, E. C.; Jovanovic, I.; Robinson, J. A. Radiation Effects on Two-Dimensional Materials: Radiation Effects on Two-Dimensional Materials. *Phys. Status Solidi A* **2016**, *213* (12), 3065–3077. https://doi.org/10.1002/pssa.201600395

(46) Polster, J. W.; Aydin, F.; De Souza, J. P.; Bazant, M. Z.; Pham, T. A.; Siwy, Z. S. Rectified and Salt Concentration Dependent Wetting of Hydrophobic Nanopores. *J. Am. Chem. Soc.* **2022**, *144* (26), 11693–11705. https://doi.org/10.1021/jacs.2c03436

(47) Howorka, S.; Siwy, Z. Nanopore Analytics: Sensing of Single Molecules. *Chem. Soc. Rev.* **2009**, *38* (8), 2360. https://doi.org/10.1039/b813796j

(48) Xue, L.; Yamazaki, H.; Ren, R.; Wanunu, M.; Ivanov, A. P.; Edel, J. B. Solid-State Nanopore Sensors. *Nat. Rev. Mater.* **2020**, *5* (12), 931–951. https://doi.org/10.1038/s41578-020-0229-6

(49) Rahman, M.; Sampad, M. J. N.; Hawkins, A.; Schmidt, H. Recent Advances in Integrated Solid-State Nanopore Sensors. *Lab. Chip* **2021**, *21* (16), 3030–3052. https://doi.org/10.1039/D1LC00294E

(50) Wanunu, M. Nanopores: A Journey towards DNA Sequencing. *Phys. Life Rev.* **2012**, *9* (2), 125–158. https://doi.org/10.1016/j.plrev.2012.05.010

(51) Wanunu, M. Back and Forth with Nanopore Peptide Sequencing. *Nat. Biotechnol.* **2022**, *40* (2), 172–173. https://doi.org/10.1038/s41587-021-01205-x

(52) Brinkerhoff, H.; Kang, A. S. W.; Liu, J.; Aksimentiev, A.; Dekker, C. Multiple Rereads of Single Proteins at Single–Amino Acid Resolution Using Nanopores. *Science* **2021**, *374* (6574), 1509–1513. https://doi.org/10.1126/science.abl4381

(53) Deamer, D.; Akeson, M.; Branton, D. Three Decades of Nanopore Sequencing. *Nat. Biotechnol.* **2016**, *34* (5), 518–524. https://doi.org/10.1038/nbt.3423

(54) Nivala, J.; Marks, D. B.; Akeson, M. Unfoldase-Mediated Protein Translocation through an α-Hemolysin Nanopore. *Nat. Biotechnol.* **2013**, *31* (3), 247–250. https://doi.org/10.1038/nbt.2503

(55) Rodriguez-Larrea, D.; Bayley, H. Multistep Protein Unfolding during Nanopore Translocation. *Nat. Nanotechnol.* **2013**, *8* (4), 288–295. https://doi.org/10.1038/nnano.2013.22

(56) Ouldali, H.; Sarthak, K.; Ensslen, T.; Piguet, F.; Manivet, P.; Pelta, J.; Behrends, J. C.; Aksimentiev, A.; Oukhaled, A. Electrical Recognition of the Twenty Proteinogenic Amino Acids Using an Aerolysin Nanopore. *Nat. Biotechnol.* **2020**, *38* (2), 176–181. https://doi.org/10.1038/s41587-019-0345-2

(57) Hou, X.; Guo, W.; Jiang, L. Biomimetic Smart Nanopores and Nanochannels. *Chem. Soc. Rev.* **2011**, *40* (5), 2385. https://doi.org/10.1039/c0cs00053a

(58) Acar, E. T.; Buchsbaum, S. F.; Combs, C.; Fornasiero, F.; Siwy, Z. S. Biomimetic Potassium-Selective Nanopores. *Sci. Adv.* **2019**, *5* (2), eaav2568. https://doi.org/10.1126/sciadv.aav2568

(59) Kowalczyk, S. W.; Blosser, T. R.; Dekker, C. Biomimetic Nanopores: Learning from and about Nature. *Trends Biotechnol.* **2011**, *29* (12), 607–614. https://doi.org/10.1016/j.tibtech.2011.07.006

(60) Tagliazucchi, M.; Szleifer, I. Transport Mechanisms in Nanopores and Nanochannels: Can We Mimic Nature? *Mater. Today* **2015**, *18* (3), 131–142. https://doi.org/10.1016/j.mattod.2014.10.020

(61) Siwy, Z.; Fuliński, A. Origin of 1 / f α Noise in Membrane Channel Currents. *Phys. Rev. Lett.* **2002**, *89* (15), 158101. https://doi.org/10.1103/PhysRevLett.89.158101

(62) Schoch, R. B.; Han, J.; Renaud, P. Transport Phenomena in Nanofluidics. *Rev. Mod. Phys.* **2008**, *80* (3), 839–883. https://doi.org/10.1103/RevModPhys.80.839

(63) Siwy, Z. S.; Howorka, S. Engineered Voltage-Responsive Nanopores. *Chem Soc Rev* **2010**, *39* (3), 1115–1132. https://doi.org/10.1039/B909105J

(64) Vlassiouk, I.; Siwy, Z. S. Nanofluidic Diode. *Nano Lett.* **2007**, *7* (3), 552–556. https://doi.org/10.1021/nl062924b

(65) Karnik, R.; Duan, C.; Castelino, K.; Daiguji, H.; Majumdar, A. Rectification of Ionic Current in a Nanofluidic Diode. *Nano Lett.* **2007**, *7* (3), 547–551. https://doi.org/10.1021/nl062806o

(66) Powell, M. R.; Cleary, L.; Davenport, M.; Shea, K. J.; Siwy, Z. S. Electric-Field-Induced Wetting and Dewetting in Single Hydrophobic Nanopores. *Nat. Nanotechnol.* **2011**, *6* (12), 798–802. https://doi.org/10.1038/nnano.2011.189

(67) Polster, J. W.; Acar, E. T.; Aydin, F.; Zhan, C.; Pham, T. A.; Siwy, Z. S. Gatingof Hydrophobic Nanopores with Large Anions. *ACS Nano* **2020**, *14* (4), 4306–4315. https://doi.org/10.1021/acsnano.9b09777

(68) Aryal, P.; Sansom, M. S. P.; Tucker, S. J. Hydrophobic Gating in Ion Channels. *J. Mol. Biol.* **2015**, *427* (1), 121–130. https://doi.org/10.1016/j.jmb.2014.07.030

(69) Klesse, G.; Tucker, S. J.; Sansom, M. S. P. Electric Field Induced Wetting of a Hydrophobic Gate in a Model Nanopore Based on the 5-HT_3 Receptor Channel. *ACS Nano* **2020**, *14* (8), 10480–10491. https://doi.org/10.1021/acsnano.0c04387

(70) Zhang, Z.; He, L.; Zhu, C.; Qian, Y.; Wen, L.; Jiang, L. Improved Osmotic Energy Conversion in Heterogeneous Membrane Boosted by Three-Dimensional Hydrogel Interface. *Nat. Commun.* **2020**, *11* (1), 875. https://doi.org/10.1038/s41467-020-14674-6

(71) Lin, C.-Y.; Combs, C.; Su, Y.-S.; Yeh, L.-H.; Siwy, Z. S. Rectification of Concentration Polarization in Mesopores Leads To High Conductance Ionic Diodes and High Performance Osmotic Power. *J. Am. Chem. Soc.* **2019**, *141* (8), 3691–3698. https://doi.org/10.1021/jacs.8b13497

(72) Hille, B. *Ion Channels of Excitable Membranes*, 3. ed.; Sinauer Assoc: Sunderland, Mass, 2001.

(73) Garalde, D. R.; Snell, E. A.; Jachimowicz, D.; Sipos, B.; Lloyd, J. H.; Bruce, M.; Pantic, N.; Admassu, T.; James, P.; Warland, A.; Jordan, M.; Ciccone, J.; Serra, S.; Keenan, J.; Martin, S.; McNeill, L.; Wallace, E. J.; Jayasinghe, L.; Wright, C.; Blasco, J.; Young, S.; Brocklebank, D.; Juul, S.; Clarke, J.; Heron, A. J.; Turner, D. J. Highly Parallel Direct RNA Sequencing on an Array of Nanopores. *Nat. Methods* **2018**, *15* (3), 201–206. https://doi.org/10.1038/nmeth.4577

(74) Van De Groep, J.; Brongersma, M. L. Metasurface Mirrors for External Control of Mie Resonances. *Nano Lett.* **2018**, *18* (6), 3857–3864. https://doi.org/10.1021/acs.nanolett.8b01148

(75) Liu, Y.; Holzinger, A.; Knittel, P.; Poltorak, L.; Gamero-Quijano, A.; Rickard, W. D. A.; Walcarius, A.; Herzog, G.; Kranz, C.; Arrigan, D. W. M. Visualization of Diffusion within Nanoarrays. *Anal. Chem.* **2016**, *88* (13), 6689–6695. https://doi.org/10.1021/acs.analchem.6b00513

(76) Gadaleta, A.; Sempere, C.; Gravelle, S.; Siria, A.; Fulcrand, R.; Ybert, C.; Bocquet, L. Sub-Additive Ionic Transport across Arrays of Solid-State Nanopores. *Phys. Fluids* **2014**, *26* (1), 012005. https://doi.org/10.1063/1.4863206

(77) Hall, J. E. Access Resistance of a Small Circular Pore. *J. Gen. Physiol.* **1975**, *66* (4), 531–532. https://doi.org/10.1085/jgp.66.4.531

(78) Freger, V. Selectivity and Polarization in Water Channel Membranes: Lessons Learned from Polymeric Membranes and CNTs. *Faraday Discuss.* **2018**, *209*, 371–388. https://doi.org/10.1039/C8FD00054A

(79) Yazda, K.; Bleau, K.; Zhang, Y.; Capaldi, X.; St-Denis, T.; Grutter, P.; Reisner, W. W. High Osmotic Power Generation via Nanopore Arrays in Hybrid Hexagonal Boron Nitride/Silicon Nitride Membranes. *Nano Lett.* **2021**, *21* (10), 4152–4159. https://doi.org/10.1021/acs.nanolett.0c04704

(80) Han, W.; Chen, X. A Review: Applications of Ion Transport in Micro-nanofluidic Systems Based on Ion Concentration Polarization. *J. Chem. Technol. Biotechnol.* **2020**, *95* (6), 1622–1631. https://doi.org/10.1002/jctb.6288

(81) Green, Y.; Shloush, S.; Yossifon, G. Effect of Geometry on Concentration Polarization in Realistic Heterogeneous Permselective Systems. *Phys. Rev. E* **2014**, *89* (4), 043015. https://doi.org/10.1103/PhysRevE.89.043015

(82) Zangle, T. A.; Mani, A.; Santiago, J. G. Theory and Experiments of Concentration Polarization and Ion Focusing at Microchannel and Nanochannel Interfaces. *Chem. Soc. Rev.* **2010**, *39* (3), 1014. https://doi.org/10.1039/b902074h

(83) Park, H. B.; Kamcev, J.; Robeson, L. M.; Elimelech, M.; Freeman, B. D. Maximizing the Right Stuff: The Trade-off between Membrane Permeability and Selectivity. *Science* **2017**, *356* (6343), eaab0530. https://doi.org/10.1126/science.aab0530

(84) Epsztein, R.; DuChanois, R. M.; Ritt, C. L.; Noy, A.; Elimelech, M. Towards Single-Species Selectivity of Membranes with Subnanometre Pores. *Nat. Nanotechnol.* **2020**, *15* (6), 426–436. https://doi.org/10.1038/s41565-020-0713-6

(85) Lively, R. P.; Sholl, D. S. From Water to Organics in Membrane Separations. *Nat. Mater.* **2017**, *16* (3), 276–279. https://doi.org/10.1038/nmat4860

(86) Siwy, Z. S.; Bruening, M. L.; Howorka, S. Nanopores: Synergy from DNA Sequencing to Industrial Filtration – Small Holes with Big Impact. *Chem. Soc. Rev.* **2023**, *52* (6), 1983–1994. https://doi.org/10.1039/D2CS00894G

(87) Stein, D.; Kruithof, M.; Dekker, C. Surface-Charge-Governed Ion Transport in Nanofluidic Channels. *Phys. Rev. Lett.* **2004**, *93* (3), 035901. https://doi.org/10.1103/PhysRevLett.93.035901

(88) Lucas, R. A.; Siwy, Z. S. Tunable Nanopore Arrays as the Basis for Ionic Circuits. *ACS Appl. Mater. Interfaces* **2020**, *12* (50), 56622–56631. https://doi.org/10.1021/acsami.0c18574

(89) Ma, L.; An, X.; Song, F.; Qiu, Y. Effective Charged Exterior Surfaces for Enhanced Ionic Diffusion through Nanopores under Salt Gradients. *J. Phys. Chem. Lett.* **2022**, *13* (24), 5669–5676. https://doi.org/10.1021/acs.jpclett.2c01351

(90) Cao, L.; Wen, Q.; Feng, Y.; Ji, D.; Li, H.; Li, N.; Jiang, L.; Guo, W. On the Origin of Ion Selectivity in Ultrathin Nanopores: Insights for Membrane-Scale Osmotic Energy Conversion. *Adv. Funct. Mater.* **2018**, *28* (39), 1804189. https://doi.org/10.1002/adfm.201804189

(91) Lee, C.; Joly, L.; Siria, A.; Biance, A.-L.; Fulcrand, R.; Bocquet, L. Large Apparent Electric Size of Solid-State Nanopores Due to Spatially Extended Surface Conduction. *Nano Lett.* **2012**, *12* (8), 4037–4044. https://doi.org/10.1021/nl301412b

(92) Wang, L.; Wang, Z.; Patel, S. K.; Lin, S.; Elimelech, M. Nanopore-Based Power Generation from Salinity Gradient: Why It Is Not Viable. *ACS Nano* **2021**, *15* (3), 4093–4107. https://doi.org/10.1021/acsnano.0c08628

(93) Zhang, Z.; Huang, X.; Qian, Y.; Chen, W.; Wen, L.; Jiang, L. Engineering Smart Nanofluidic Systems for Artificial Ion Channels and Ion Pumps: From Single-Pore to Multichannel Membranes. *Adv. Mater.* **2020**, *32* (4), 1904351. https://doi.org/10.1002/adma.201904351

(94) Smeets, R. M. M.; Keyser, U. F.; Krapf, D.; Wu, M.-Y.; Dekker, N. H.; Dekker, C. Salt Dependence of Ion Transport and DNA Translocation through Solid-State Nanopores. *Nano Lett.* **2006**, *6* (1), 89–95. https://doi.org/10.1021/nl052107w

(95) Arrigan, D. W. M. Nanoelectrodes, Nanoelectrode Arrays and Their Applications. *The Analyst* **2004**, *129* (12), 1157. https://doi.org/10.1039/b415395m

(96) Liu, Y.; Sairi, M.; Neusser, G.; Kranz, C.; Arrigan, D. W. M. Achievement of Diffusional Independence at Nanoscale Liquid–Liquid Interfaces within Arrays. *Anal. Chem.* **2015**, *87* (11), 5486–5490. https://doi.org/10.1021/acs.analchem.5b01162

(97) Ho, C.; Qiao, R.; Heng, J. B.; Chatterjee, A.; Timp, R. J.; Aluru, N. R.; Timp, G. Electrolytic Transport through a Synthetic Nanometer-Diameter Pore. *Proc. Natl. Acad. Sci.* **2005**, *102* (30), 10445–10450. https://doi.org/10.1073/pnas.0500796102

(98) Van Den Hout, M.; Hall, A. R.; Wu, M. Y.; Zandbergen, H. W.; Dekker, C.; Dekker, N. H. Controlling Nanopore Size, Shape and Stability. *Nanotechnology* **2010**, *21* (11), 115304. https://doi.org/10.1088/0957-4484/21/11/115304

(99) Li, M.; Anand, Robbyn. K. Recent Advancements in Ion Concentration Polarization. *The Analyst* **2016**, *141* (12), 3496–3510. https://doi.org/10.1039/C6AN00194G

(100) Daiguji, H.; Oka, Y.; Shirono, K. Nanofluidic Diode and Bipolar Transistor. *Nano Lett.* **2005**, *5* (11), 2274–2280. https://doi.org/10.1021/nl051646y

(101) Constantin, D.; Siwy, Z. S. Poisson-Nernst-Planck Model of Ion Current Rectification through a Nanofluidic Diode. *Phys. Rev. E* **2007**, *76* (4), 041202. https://doi.org/10.1103/PhysRevE.76.041202

(102) Robin, P.; Kavokine, N.; Bocquet, L. Modeling of Emergent Memory and Voltage Spiking in Ionic Transport through Angstrom-Scale Slits. *Science* **2021**, *373* (6555), 687–691. https://doi.org/10.1126/science.abf7923

(103) Zhang, S.; Wang, J.; Yaroshchuk, A.; Du, Q.; Xin, P.; Bruening, M. L.; Xia, F. Addressing Challenges in Ion-Selectivity Characterization in Nanopores. *J. Am. Chem. Soc.* **2024**, jacs.4c00603. https://doi.org/10.1021/jacs.4c00603

(104) Daiguji, H.; Yang, P.; Majumdar, A. Ion Transport in Nanofluidic Channels. *Nano Lett.* **2004**, *4* (1), 137–142. https://doi.org/10.1021/nl0348185

(105) Green, Y. Ion Transport in Nanopores with Highly Overlapping Electric Double Layers. *J. Chem. Phys.* **2021**, *154* (8), 084705. https://doi.org/10.1063/5.0037873

(106) Plecis, A.; Schoch, R. B.; Renaud, P. Ionic Transport Phenomena in Nanofluidics: Experimental and Theoretical Study of the Exclusion-Enrichment Effect on a Chip. *Nano Lett.* **2005**, *5* (6), 1147–1155. https://doi.org/10.1021/nl050265h

(107) Su, S.; Zhang, Y.; Peng, S.; Guo, L.; Liu, Y.; Fu, E.; Yao, H.; Du, J.; Du, G.; Xue, J. Multifunctional Graphene Heterogeneous Nanochannel with Voltage-Tunable Ion Selectivity. *Nat. Commun.* **2022**, *13* (1), 4894. https://doi.org/10.1038/s41467-022-32590-9

(108) Ma, L.; Li, Z.; Yuan, Z.; Wang, H.; Huang, C.; Qiu, Y. High-Performance Nanofluidic Osmotic Power Generation Enabled by Exterior Surface Charges under the Natural Salt Gradient. *J. Power Sources* **2021**, *492*, 229637. https://doi.org/10.1016/j.jpowsour.2021.229637

(109) Vlassiouk, I.; Smirnov, S.; Siwy, Z. Ionic Selectivity of Single Nanochannels. *Nano Lett.* **2008**, *8* (7), 1978–1985. https://doi.org/10.1021/nl800949k

(110) Feng, J.; Graf, M.; Liu, K.; Ovchinnikov, D.; Dumcenco, D.; Heiranian, M.; Nandigana, V.; Aluru, N. R.; Kis, A.; Radenovic, A. Single-Layer MoS2 Nanopores as Nanopower Generators. *Nature* **2016**, *536* (7615), 197–200. https://doi.org/10.1038/nature18593

(111) Siria, A.; Poncharal, P.; Biance, A.-L.; Fulcrand, R.; Blase, X.; Purcell, S. T.; Bocquet, L. Giant Osmotic Energy Conversion Measured in a Single Transmembrane Boron Nitride Nanotube. *Nature* **2013**, *494* (7438), 455–458. https://doi.org/10.1038/nature11876

(112) Tsutsui, M.; Hsu, W.-L.; Garoli, D.; Leong, I. W.; Yokota, K.; Daiguji, H.; Kawai, T. Gate-All-Around Nanopore Osmotic Power Generators. *ACS Nano* **2024**, *18* (23), 15046–15054. https://doi.org/10.1021/acsnano.4c01989

(113) Zhang, Z.; Wen, L.; Jiang, L. Nanofluidics for Osmotic Energy Conversion. *Nat. Rev. Mater.* **2021**, *6* (7), 622–639. https://doi.org/10.1038/s41578-021-00300-4

(114) Xie, G.; Wen, L.; Jiang, L. Biomimetic Smart Nanochannels for Power Harvesting. *Nano Res.* **2016**, *9* (1), 59–71. https://doi.org/10.1007/s12274-016-0993-1

(115) Lucas, R. A.; Lin, C.-Y.; Baker, L. A.; Siwy, Z. S. Ionic Amplifying Circuits Inspired by Electronics and Biology. *Nat. Commun.* **2020**, *11* (1), 1568. https://doi.org/10.1038/s41467-020-15398-3

(116) Ni, Z.; Qiu, H.; Guo, W. Electrically Tunable Ion Selectivity of Charged Nanopores. *J. Phys. Chem. C* **2018**, *122* (51), 29380–29385. https://doi.org/10.1021/acs.jpcc.8b10191

(117) Liu, S.; Zhang, X.; Yang, Y.; Hu, N. Ion Transport in Multi-Nanochannels Regulated by pH and Ion Concentration. *Anal. Chem.* **2024**, *96* (14), 5648–5657. https://doi.org/10.1021/acs.analchem.4c00406

(118) Green, Y.; Abu-Rjal, R.; Eshel, R. Electrical Resistance of Nanochannel-Microchannel Systems: An Exact Solution. *Phys. Rev. Appl.* **2020**, *14* (1), 014075. https://doi.org/10.1103/PhysRevApplied.14.014075

(119) Melnikov, D. V.; Hulings, Z. K.; Gracheva, M. E. Concentration Polarization, Surface Charge, and Ionic Current Blockade in Nanopores. *J. Phys. Chem. C* **2020**, *124* (36), 19802–19808. https://doi.org/10.1021/acs.jpcc.0c04829